Exploring Methods to Increase Sensitivity in Low Mass Dark Matter Search for CRESST-III

Dissertation

der Mathematisch-Naturwissenschaftlichen Fakultät

der Eberhard Karls Universität Tübingen

zur Erlangung des Grades eines

Doktors der Naturwissenschaften

(Dr. rer. nat.)

vorgelegt von

Lena Meyer

aus Bad Urach

Tübingen

2024

Gedruckt mit Genehmigung der Mathematisch-Naturwissenschaftlichen Fakultät der Eberhard Karls Universität Tübingen.

Tag der mündlichen Qualifikation:	01.08.2024
Dekan:	Prof. Dr. Thilo Stehle
1. Berichterstatter/-in:	Prof. Dr. Josef Jochum
2. Berichterstatter/-in:	Prof. Dr. Tobias Lachenmaier

Zusammenfassung

Dunkle Materie ist eines der größten Mysterien der modernen Physik und einer der Schlüssel zum Verständnis des Universums. Seit über 30 Jahren ist die Suche nach Dunkle-Materie-Teilchen mit schwacher Wechselwirkung (WIMPs) erfolglos, was dazu führte, dass der Fokus von Experimenten, die nach dunkler Materie suchen, wie CRESST sich zu Wechselwirkungen auf der subschwachen Skala verschob. Das CRESST-Experiment ist ein kryogenes Direkt-Nachweis-Experiment mit dem Ziel, den Rückstoß von Teilchen aus dem dunklen Halo, der unsere Galaxie umgibt, an Kernen in einem Targetkristal mit Hilfe von supraleitenden Thermometern zu detektieren. Um den neugewonnenen Parameterbereich zu erforschen, muss das Experiment sensitiver für niedrigere Dunkle-Materie-Massen im sub-GeV/c^2-Bereich werden. Hierfür werden sensitivere Detektoren mit niedrigeren Energieschwellen benötigt. Neben der Entwicklung von neuen Detektordesigns wurde ein Softwaretrigger in [1] eingeführt, der einen digitalen Filter zur Optimierung der Signal-Rausch-Verhältnisse verwendet [2]. Der erste Teil dieser Thesis fokussiert sich auf den Versuch, die Implementierung der Filter im derzeitigen CRESST-Analyse-Framework zu optimieren. Die Idee, zusätzliche Bandpassfilter zu verwenden, die ungewünschte Rauschfrequenzen und computerbasierte Artefakte weiter unterdrücken sollen wurde untersucht. Eine Verbesserung der Auflösung im Niedrigenergiebereich und der Energieschwelle konnte jedoch nicht erreicht werden. Dabei wurde erfolgreich ein neuer niederenergetischer Referenzpeak für eine präzisere Energiekalibrierung des Rückstoßspektrums verwendet.
Bei neuesten Messungen konnten Energieschwellen von bis 10 eV erreicht werden [3], dies brachte jedoch eine neue Herausforderung mit sich. Im Energiebereich unter 200 eV ist ein exponentiell-ähnlicher Anstieg an Ereignissen in Richtung der Trigger Schwelle in allen in CRESST betriebenen Detektoren zu beobachten. Das Energiespektrum der Ereignisse imitiert ein Dunkle-Materie-Signal, aber eine relativ kurze Zerfallszeit schließt eine Erklärung durch dunkle Materie aus. Ein neuer Fokus, um das Signal zu verstehen und zu entfernen, wurde gesetzt. Der zweite Teil dieser Thesis zeigt eine Niedrigenergieanalyse eines CRESST-III-Moduls, das für [4] produziert und analysiert wurde. Vollständigkeitshalber wird eine Wiederholung der standard spinunabhängigen Analyse zur Setzung von Ausschlussgrenzen für Dunkle-Materie-Massen präsentiert. Die Zeit-, Energie- und Temperaturabhänigkeit der beobachteten Überschussereignisse wird untersucht. Eine zweite Dunkle-Materie-Analyse wird an einem Datenset mit geringem Überschuss, entstanden durch den zeitlichen Zerfall, durchgeführt. Die resultierende Ausschlussgrenze erreicht niedrigere Wechselwirkungsquerschnitte im selben Massebereich mit signifikant geringerer Exposition, was die begrenzende Natur der Niedrigenergie-Überschussevents in der Suche nach niedermassiger, dunkler Materie demonstriert.

Abstract

Dark matter is one of the greatest mysteries of modern physics and one of the keys to understanding our universe. For more than 30 years, searches for weakly-interacting dark matter particles (WIMPs) have been unsuccessful, resulting in dark matter search experiments like CRESST to focus on interactions on the sub-weak scale. The CRESST experiment is a cryogenic direct detection experiment aiming to detect the recoil of particles in the dark matter halo surrounding our galaxy. The experiment utilizes superconducting thermometers to detect the recoil of dark matter particles on target nuclei. To explore the new open parameter space, the experiment needs to be sensitive to lower dark matter masses in the sub-GeV/c^2 scale, requiring more sensitive detectors with lower thresholds. Besides the development of new detector modules, a software trigger was introduced in [1] using a digital filter to optimise the signal to noise ratio [2]. The first part of this thesis focuses on an attempt to further optimise the implementation of the filter in the current CRESST analysis framework. The idea of using additional band-pass filters to further suppress unwanted noise frequencies and computational artefacts is explored, but an improvement in energy resolution and threshold could not be achieved. In the process, a new lower energetic reference peak was successfully used for a more accurate energy calibration of the recoil spectrum.
In recent measurements, thresholds as low as 10 eV could be reached [3], but this introduced a new challenge. In the energy range below 200 eV, an exponential-like rise of events is observed towards the threshold in all detectors operated in CRESST. The events mimic a dark matter signal in energy, but a relatively fast time decay can be seen, excluding a dark matter explanation. A new focus is set to understand or remove the excess signal. The second part of this thesis shows the low energy analysis of a CRESST-III module that was produced and analysed for [4]. For completeness, a repetition of the standard spin-independent analysis to set dark matter exclusion limits that was performed in the scope of this thesis is presented. The time, energy, and temperature dependence of the observed excess events are studied. A second dark matter search analysis is performed on a data set with reduced excess event rate, taking advantage of the excess time decay. The resulting exclusion limit reaches lower interaction cross sections in the same mass range with significantly less exposure, demonstrating the limiting nature of the low energy excess events to low mass dark matter search in CRESST.

Contents

Chapter 1

Dark Matter

This chapter gives a short introduction to Dark Matter (DM). In Section 1.1 an overview of the most compelling evidence for the existence of DM is presented, Section 1.2 shows a selection of possible DM candidates. In Section 1.3 the currently most prominent attempts for the detection of DM are presented.

1.1 Observational Evidence

1.1.1 Gravitational Evidence

The term "dark matter" (or originally "dunkle Materie") was first used by Fritz Zwicky in 1933 to explain the high velocity dispersion of galaxies in the Coma cluster [5]. He determined the velocity within the cluster through the Doppler red shift and calculated the virial mass [6]. This calculated mass was significantly higher than the mass expected from the cluster's luminosity, leading to the postulation of non-luminous "dark" matter.

Galaxy Rotation Curves

More observations on the gravitational evidence for DM were made in the 1970s by Vera Rubin [7, 8]. She measured the rotational curves of individual stars in spiral galaxies. The velocity v of a star following a circular orbit with radius r around the galactic center is given by

$$v = \sqrt{G\frac{M}{r}} \propto \sqrt{\frac{1}{r}} \tag{1.1}$$

where G is the gravitational constant and M the mass of the galaxy within the orbit r. For the considered galaxies most visible mass is located in the central bulge, leading to the expectation for the velocity to drop with $1/\sqrt{r}$ for stars outside of the bulge. However, the studied rotation curves show a flat dependence even at high radii. Figure 1.1 shows the measured rotation curve of a spiral galaxy (black dots) and the rotation curve

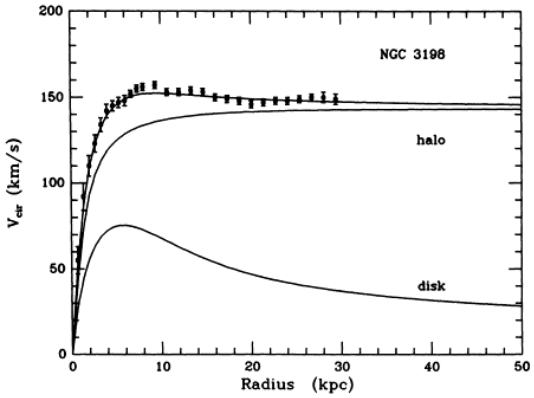

Figure 1.1: Measured rotation curve of the spiral galaxy NGC 3198 showing a fit including a mass component from the stellar disk and a DM halo, taken from [9].

expected when only considering the mass contained in the stellar disk. The introduction of a spherical DM halo leads to the best description of the measured data.

Bullet Cluster

Additional gravitational evidence for DM comes from the galaxy cluster 1E0657-558, known as the bullet cluster. The cluster is a result from the merger of two galaxy clusters as depicted in [10]. Figure 1.2 shows the distribution of galaxies within the cluster on the left and the distribution of hot gas, which holds the majority of the visible mass, on the right. The density of galaxies within the two clusters is low enough for them to pass through each other, while the gas is slowed down due to electromagnetic interaction between the particles. The mass distribution of the cluster determined via gravitational lensing does not match the visible mass distribution of the hot gas. The difference can be explained with a large amount of non-visible matter within the galaxies, which can pass through each other with minimal to no interaction [10].

1.1.2 Cosmic Microwave Background

Around 380 000 years after the big bang the universe reached a temperature of $\sim$0.3 eV causing photons to freeze-out from matter. They could now freely move through the universe, creating the Cosmic Microwave Background (CMB). The CMB is observed as a black body spectrum at 2.73 K with fluctuations in the order of 10^{-5} K. The fluctuations originate from different gravitational potentials during the freeze-out. In more dense regions the photons needed more energy to escape causing a red shift and vice versa a blue shift in low density regions [11]. Without the presence of DM the fluctuations would have been washed out by the counter pressure of the electromagnetic radiation. A fit of the ΛCDM model to data from the Planck telescope shows that only a small fraction of 5 % of the energy density of the universe comes from baryonic matter, while DM contributes 26 % [12].

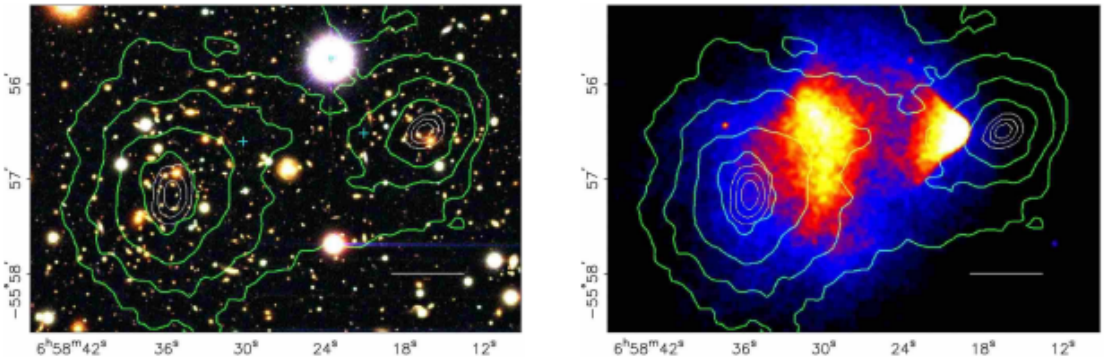

Figure 1.2: The left graphic shows a colour image of the merging bullet cluster. The right graphic shows the distribution of hot gas in the cluster merger. The green and white lines show the mass distribution expected from gravitational lensing, taken from [10].

Structure Formation

The small fluctuations in the CMB combined with the expansion of the universe lead to the large scale structures we observe today. In regions with strong gravitational potential the expansion of matter density is slowed down leading to different regions with varying densities [13]. Extensive numerical simulations tracing the matter distribution can only reproduce the structures we observe today with the presence of DM [14].

1.2 Dark Matter Candidates

Today there are many theories for DM candidates in all mass ranges. In general, they have to follow certain requirements: Considering their presence during the photon freeze-out, they need to be stable or have a life time of at least the age of the universe. They need to be present in the right abundance, but there can be several types of particles. The majority needs to be non-relativistic or "cold", since relativistic DM could not lead to the formation of large structures. They need to interact gravitationally and other interactions need to be very weak or zero. They need to be produced in the very early universe, have no charge and are non-baryonic. This section shows a selection of potential DM candidates.

1.2.1 WIMPs

Weakly Interacting Massive Particles (WIMPs) are a general class of particles that are massive, stable and follow interactions of the weak scale. They are said to be produced in the early universe in thermal equilibrium with other particles. With the cool down of the universe, the production became unfavourable, and with the expansion of the universe, eventually the annihilation as well, leading to the stable density we observe

today [15, 16]. The annihilation cross section of these particles can be calculated with the current mass density and returns values of the weak scale. This apparent coincidence is often referred to as the WIMP miracle. The mass of the particles can be in the order of $\mathrm{GeV/c^2}$ to $\mathrm{TeV/c^2}$, but is restricted to be larger than $2\,\mathrm{GeV/c^2}$ [17]. Today most of the given parameter space is explored and after many years WIMPs are slowly becoming disfavoured and other theories are being explored.

Hidden Sector Dark Matter

Without an evident reason why the interaction should be limited to the weak nuclear force, lower masses and interaction cross sections can still be explored. Under the assumption of no or a new type of interaction one is no longer limited to the standard model and different combinations of mass and coupling return the right particle density, referred to as the WIMPless miracle [18].

1.2.2 Axions

The axion is a well motivated DM candidate, that was introduced as a solution to the strong CP problem. Measurements of the neutron electric dipole moment [19] can be related to a vanishing CP violating angle in QCD, but in fundamental theory CP violation should be allowed in the strong interaction and the violating angle of $\mathcal{O}(1)$ [20]. A solution to the problem was proposed by introducing the Pecci-Quinn symmetry; a global symmetry, that is broken by colour anomaly and spontaneously [21]. The theory includes a light pseudo-scalar particle [22], that fits DM particle requirements.

1.2.3 Non-particle Explanations

Most DM theories include a proposed particle, but there are alternative explanation attempts. One theory is the existence of Massive Compact Halo Objects (MACHOs), large baryonic objects such as neutron stars, black holes, or brown dwarfs, that emit minimal radiation, leaving them undetected so far. Recently primordial black holes, black holes created in the early universe from the collapse of extremely dense regions [23, 24], have become a favoured candidate. Their existence or lack thereof should be proven within the following decade.
Other theories are trying to explain the observed evidence without the existence of DM in any form. The most known is MOdified Newtonian Dynamics (MOND). It was originally introduced to explain galaxy rotation curves by extending the Newtonian force with an interpolating term based on an arbitrarily chosen constant that (surprisingly) fits most galaxies [25]. In its original form the theory cannot account for other evidence beside the galaxy rotation curves, but in the following years extensions were introduced to explain the gravitational lensing effects in cluster mergers and to remodel the CMB power spectrum [26, 27].

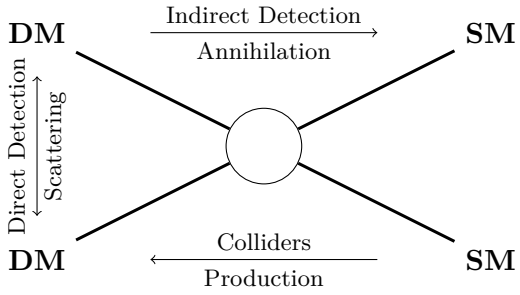

Figure 1.3: Schematic view of the different detection channels in the style of a Feynman diagram.

1.3 Detection

In current research there are three prominent detection channels for DM as shown in Figure 1.3: direct detection through scattering on standard model particles, indirect detection measuring products of DM annihilation and production of DM at particle colliders. This section focuses on direct detection.

1.3.1 Direct Detection

Under the assumption of a DM halo in our galaxy the detection of WIMPs and WIMP-like particles is possible anywhere on earth. The challenge lies in creating sensitive detectors with very low background or large target mass to accommodate for the small interaction cross section of DM. In the right environment DM can be detected through elastic coherent scattering on target nuclei or electrons. The recoil energy of the process is given by elastic two body scattering

$$E_R = \frac{\mu^2 v^2}{m_T}(1 - \cos(\theta)). \tag{1.2}$$

μ is the reduced mass of the DM particle and the nucleus, v is the relative velocity of the particle, m_T is the mass of the target nucleus and θ the scattering angle. Direct detection experiments aim to measure the differential recoil rate, that can be derived from the expected interaction rate per mass unit

$$R \sim \frac{\rho_{DM}}{m_{DM}} \langle v \rangle \sigma \frac{N_T}{m_T}. \tag{1.3}$$

depending on the density of the DM halo ρ_{DM}, the mass of a DM particle m_{DM} and its expected velocity $\langle v \rangle$, the interaction cross section σ and the number of target nuclei N_T. The differential recoil rate is given by

$$\frac{dR}{dE_R} = \frac{\rho_{DM}}{m_T m_{DM}} \int_{v_{min}}^{v_{esc}} v f(v) \frac{d\sigma(E_R, v)}{dE_R} d^3 v \tag{1.4}$$

where v_{min} is the minimum velocity need for an energy transfer to the nucleus and v_{esc} is the escape velocity of the galaxy [28]. $f(v)$ gives the velocity distribution of the DM halo in the galactic rest frame:

$$f(v) = N\Big(\frac{3}{2\pi w^2}\Big) \cdot \exp\Big(-\frac{3v^2}{2w^2}\Big) \tag{1.5}$$

with the normalization factor

$$N = \Big[\mathrm{erf}(z) - \frac{2}{\sqrt{\pi}} z \exp(-z^2)\Big]^{-1} \tag{1.6}$$

with $z^2 = 3v_{esc}^2/(2w^2)$ and $w = \sqrt{\frac{3}{2}} v_\infty$ depending on the asymptotic value of the rotational velocities v_∞ [29]. The differential cross section is given by [30]

$$\frac{d\sigma}{dE_R} = \frac{\sigma m_N}{\mu^2 v} F^2(q). \tag{1.7}$$

The nuclear form factor $F(q)$ for a momentum transfer $q^2 = 2m_N E_R$ is given as the Fourier transform of the target nucleus mass distribution, it can be obtained using a spherical Bessel function $j_1(qr_n)$ [31]:

$$F(q) = 3\frac{j_1(qr_n)}{qr_n} \exp\Big(-\frac{(qs)^2}{2}\Big), \tag{1.8}$$

where r_n is the radius of the sphere and s the width of the gaussian used to smooth the density distribution. The spin-independent cross section can be approximated by

$$\sigma \approx \frac{4\mu^2}{\pi} A^2 f^2, \tag{1.9}$$

where f is the coupling strength for protons and neutrons and A is the atomic mass number. Exemplary recoil spectra for different target materials are shown in Figure 1.4. Direct detection signals are generally read out with three different approaches: phonons, scintillation or ionisation. A combination of two can be used for background discrimination. The Cryogenic Rare Event Search using Superconducting Thermometers (CRESST) experiment uses a combination of phonon and scintillation signal, its working principle is described in the following Chapter 2. Other examples for direct detection experiments are SuperCDMS [33] and EDELWEISS [34] using scintillation and ionisation for recoil discrimination and liquid noble gas experiments like XENON [35], LZ [36] and DarkSide [37] combining ionisation and scintillation.

1.3.2 Indirect Detection

Indirect detection experiments search for the annihilation products of DM, these include gamma rays, neutrinos, and antimatter-matter pairs. Although DM signals can be extracted from antimatter and gamma ray spectra recorded, they tend to be of low intensity

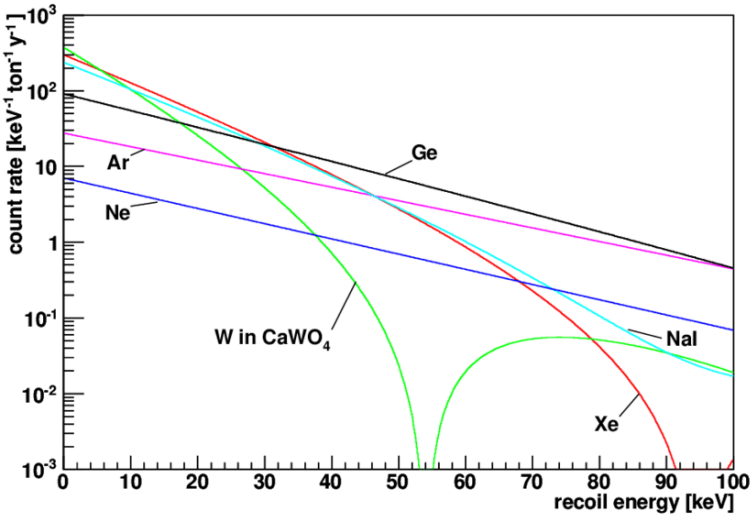

Figure 1.4: DM recoil spectrum for different target nuclei assuming a 60 GeV WIMP and a cross section of 10^{-44}cm^2, taken from [32].

compared to the expected background [38, 39]. The brightest source for indirect DM search is the galactic center, but it has many background contributions. The expected neutrino signal from DM annihilation originates from many sources within the galaxy including the sun and can potentially be observed with large-scale neutrino detectors [40, 41, 42].

1.3.3 Colliders

DM search at colliders aims to produce DM by reversing the annihilation process in the early universe by high energetic collisions of standard model particles. The produced particles are generally invisible to the experiments, but a detection can be made by observing an imbalance of reconstructed momentum of all produced particles. Details on the search with colliders at LHC can be found in [43, 44].

Chapter 2

CRESST Experiment

Phase III of the CRESST experiment is one of the leading cryogenic experiments searching for WIMPs and sub-GeV/c^2 DM. The CRESST experiment was originally proposed in 1993 [45], and first operations started in 1999 [46], making it one of the first attempts at direct DM search. In the first phase of CRESST large-scale sapphire crystals of 250 g were used as absorbers. Later, the experiment was upgraded to use wafer detectors to measure the scintillation response of the target crystal, allowing for discrimination between nuclear recoil events and electron recoil events, which are the most prominent background [47]. In this phase the target material was changed to calcium tungstate. The recent phase focuses on reaching low thresholds to probe lower DM masses. The data taking run used in this work focuses on utilising different target materials. This chapter describes the experimental setup of the CRESST experiment in Section 2.1 and introduces the detection principle in Section 2.2. The detector modules used in at least part of this work are presented in Section 2.3. The data taking method is explained in Section 2.4 and an update on the current status of the experiment and results is given in Section 2.5.

2.1 Experimental Set-up

The CRESST-Experiment is located in the Laboratori Nazionali del Gran Sasso (LNGS) under the Gran Sasso mountain in central Italy. The location was chosen because the mountain acts as a natural shielding against cosmic radiation. The halls of the laboratory are covered by 1400 m of rock, 3600 m water equivalent, reducing the event rate of cosmic muons to around $3.3\text{–}3.4 \cdot 10^{-4}\,\mathrm{s^{-1}m^{-2}}$ [49, 50]. A schematic of the vertical cross section is shown in Figure 2.1. The detector modules are mounted in a copper carousel within a dilution refrigerator. The detectors are connected to the cryostat through a 1.5 m long copper "cold finger" allowing for better shielding of the modules. The carousel is surrounded by 14 cm of copper and 20 cm of radiopure lead. The lead is used to shield from external radioactivity, the copper to shield against intrinsic radioactivity from the lead and external radioactivity. A plastic scintillator muon veto is installed outside of

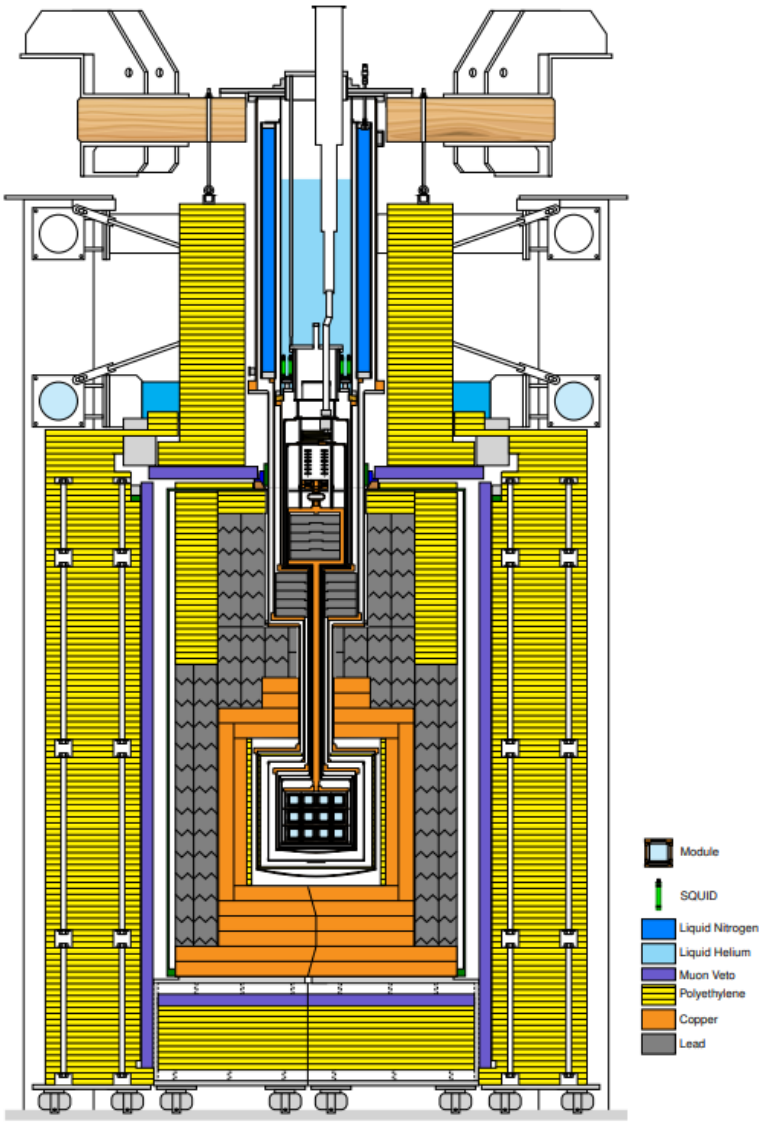

Figure 2.1: Schematic cross section of the experimental set showing the detectors in the so-called detector carousel made of cooper. The surround shielding is shown: cooper (orange), lead (grey), polyethylene (yellow), muon veto (purple). Figure taken from [48]

the cryostat, tagging the remaining muon flux that is interacting with the set up. The muon veto achieves a total solid angle coverage of 98.7 % [51]. Around the muon veto is an airtight radon box. To shield from neutrons originating in the surrounding rocks 40 cm of polyethylene make up the outer layer of the setup. Additionally a 3.5 cm layer of polyethylene is installed inside the copper layer to shield from neutrons which can be produced within the copper or lead layers through muon interactions.

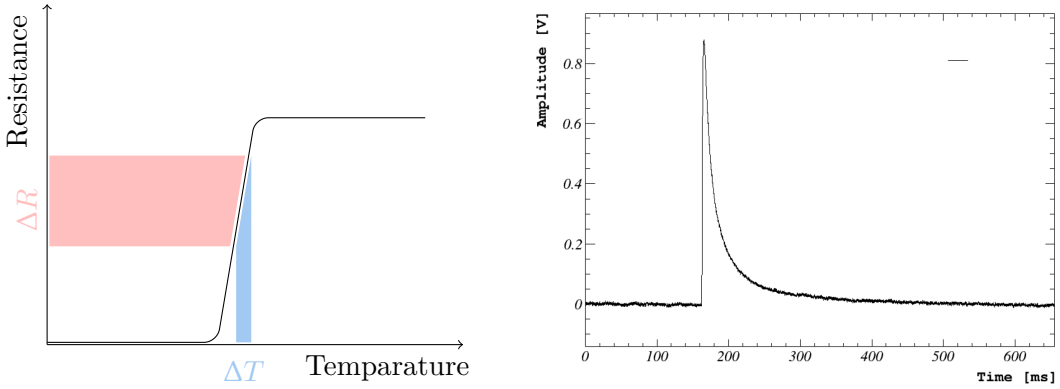

(a) Transition curve

(b) Expected signal

Figure 2.2: (a) shows a sketched transition curve of a TES used in CRESST. The blue illustrates the temperature increase in the crystal; the pink shows the following resistance increase in the sensor. (b) shows the expected read out signal. It is characterized by a fast rise corresponding to the temperature rise and a slower decay.

2.2 Detection Principle

As mentioned before, CRESST is a direct detection experiment attempting to measure the energy deposited in a target by the recoil of a DM particle on a nucleus within the crystal lattice of the target. The target is cooled to temperatures $\mathcal{O}\,(\mathrm{mK})$ minimizing the crystal lattice vibration. Particle interactions produce phonons, that travel through the crystal and cause a temperature increase. The temperature increase is read out by a Transition Edge Sensor (TES) described in Section 2.2.1. The detector readout is shown in Section 2.2.2 and the particle discrimination strategy in Section 2.2.3.

2.2.1 Transition Edge Sensors

The recoil energy ΔE deposited in the detector leads to a small rise in temperature ΔT

$$\Delta T \propto \frac{\Delta E}{C}, \tag{2.1}$$

that can be detected by the TES on the detector crystals. C is the heat capacity of the detector. To obtain the maximum temperature shift, it should be as small as possible. Generally, the heat capacity decreases with decreasing temperature, leading to the use of cryogenic detectors with operating points in the order of millikelvin. A TES in CRESST is a thin superconducting tungsten film, that is operated in the transition region between superconducting and normal conducting phase. In this region a small temperature rise of the crystal leads to rise of the resistance following the resistance over temperature curve seen in Figure 2.2a. The change of resistance can be read out by the Superconducting QUantum Interference Device (SQUID) electronics. The obtained voltage curve shows a sharp rise and a slower cool down. If the recoil energy leads to a temperature rise

that exceeds the transition region the full peak amplitude cannot be measured, the pulse shape is saturated. In addition to the TES a heater is deposited on the crystal. Through the coupling to a heat bath the crystal is brought back to its operating point. A continuously applied heater bias current stabilizes the heater.

2.2.2 Detector Readout

The TES is operated in parallel to the SQUID input coil and in series with two shunt resistors. A constant current is applied continuously, when the current in the TES changes, the magnetic field induced by the coil changes, which leads to a change of the magnetic flux in the SQUID, that increases the voltage. The voltage signal is recorded by the data acquisition system. An example of the recorded signal is shown in Figure 2.2b. For more information on the SQUID's working principle see [52, 53].

2.2.3 Particle Discrimination

The detector modules are equipped with a target crystal and wafer (or light) detector. The wafer detector consists of a Silicon-On-Sapphire (SOS) crystal and a tungsten TES to record the scintillation light created by events in the target detector. Different types of particle interactions produce different amounts of scintillation. The ratio of the phonon response E_{PH} to the light response E_L is defined as the light yield

$$LY = \frac{E_L}{E_{PH}}. \tag{2.2}$$

A typical light yield plot is sketched in Figure 2.3. The light yield is calibrated with the ^{55}Fe X-ray at 5.89 keV set to $LY = 1$. A band of electromagnetic interactions (e^- and γ) can be seen leading up to it. The nuclear recoils of W, O and Ca and the α-band appear at a lower light yield due to quenching. At low energies the bands overlap due to the finite resolution of the light detector. The Region Of Interest (ROI) or acceptance region for DM recoil events can be defined with the help of the nuclear recoil bands [54].

2.3 Detector Modules

In the latest CRESST-III run "Run36" modules with different properties were installed. They vary in material, size and holding structure. All considered detector modules are of the standard CRESST-III design shown in Figure 2.4 and listed in Table 2.1. They were first presented in [56]. The target detector is a $(20 \times 20 \times 10)\,\mathrm{mm}^3$ crystal accompanied by a $(20 \times 20 \times 0.4)\,\mathrm{mm}^3$ thin SOS wafer detector. The detector housing is made of copper and the crystals are mounted on sticks or held by clamps. All modules are equipped with a screw holding a ^{55}Fe source in the detector housing, that is functioning as a low activity iron calibration source (1 mBq). The source is covered with glue and a thin gold layer to create a shield for Auger electrons from the source and scintillation light from the added glue.

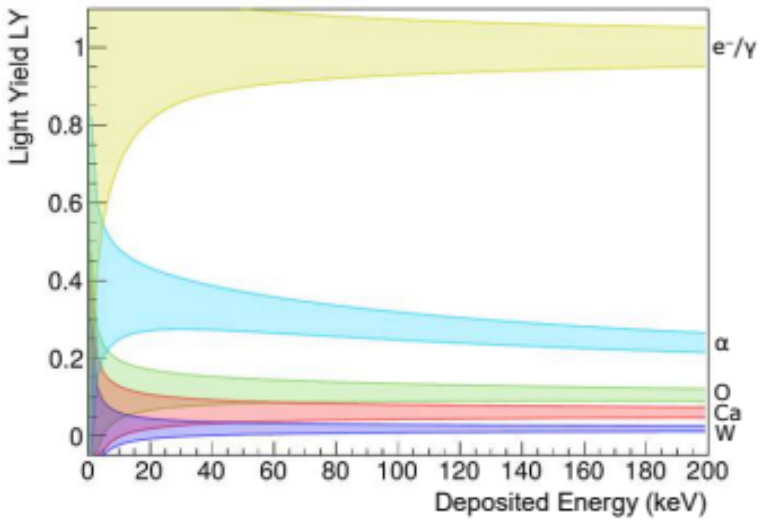

Figure 2.3: A schematic plot of the light yield featuring the e^-/γ-band (yellow), α-band (blue) and nuclear recoil bands of tungsten (purple), calcium (red) and oxygen (green). Electromagnetic background events can visually be separated from nuclear recoil events after a given threshold. Taken from [55].

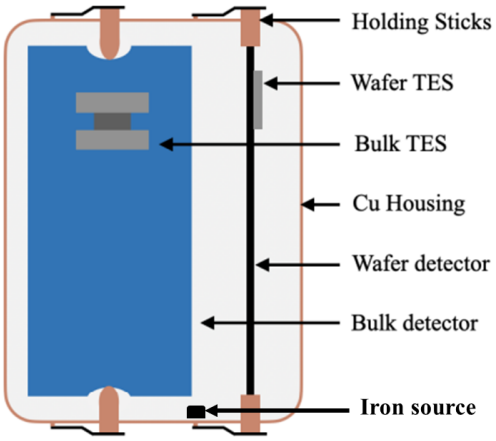

Figure 2.4: Schematic drawing of the standard detector module used in CRESST-III, modified from [56]. The modules features a target or bulk detector made of different materials specified in Table 2.1 and a SOS wafer detector. Both are equipped with a tungsten TES. The crystals are mounted on cooper (Cu), $CaWO_4$ sticks or bronze clamps. An iron source for energy calibration is installed within the housing.

Module	Material	Mass (g)	Holding	Scintillating Foil
Comm2	$CaWO_4$	24	Bronze clamps	No
TUM93A	$CaWO_4$	24	2 Cu & 1 $CaWO_4$ sticks	Yes
Sapp2	Al_2O_3	16	Cu sticks	No
Li1 and Li2	$LiAlO_2$	11	Cu sticks	Yes

Table 2.1: The five detector modules considered in at least parts of this work. All modules follow the standard CRESST-III design but feature different target material and different holding. Some have scintillating foil installed in the detector housing.

2.4 Data Taking

In the considered CRESST-III data taking run two different methods of data taking were used. One method is recording pulses only after exceeding a preset threshold value in the hardware, the other is recording the continuous data stream. In the first case a restricted window of data is recorded after the signal surpasses the preset threshold, the rest of the data stream is discarded. In a newer method the whole data stream is recorded and can later be trigger with software, this has the advantage that the threshold can still be optimized after the data is recorded. The continuously recorded data stream is referred to as streaming data. Before Run 34 of CRESST-III the recording of the entire data stream was not possible due to technical and electronic constraints. The method realising this recording is presented in [1]. In addition to the triggered data random record windows of the data stream are recorded to classify the noise seen by the detector. In case of the hardware triggered data the so-called empty baselines are recorded in set time intervals of one baseline per ten minutes of data taking. For the streaming data random samples are taken, it can be specified which percentage of the data stream should be classified as empty baselines.
During the whole data taking run heater pulses of known energy are artificially injected for mapping and calibrating the detector response. For easy discrimination in the analysis the time stamps of the injected pulses are recorded and can be used to identify triggered particle events from artificial heater pulses. In addition to these so-called test pulses, control pulses are injected. The maximum resistance change measurable is given by the difference of resistance between the start of the normal conduction phase and the resistance at the operating point. The control pulses have a large enough amplitude to drive the TES out of the transition phase into the normal conduction phase. Their recorded amplitude is used to measure the stability of the operating point.
In the current run the data taking occurs in sections of about 40–60 h, using the helium refill that is scheduled three times a week as a divider. The main data of the run was taken between November 2020 and August 2021. The data for the neutron calibration was taken in August and September 2021. The After Warm-Up (AWU) data was taken between January 2022 and February 2024. The blind AWU data set was taken between December 2022 and March 2023.

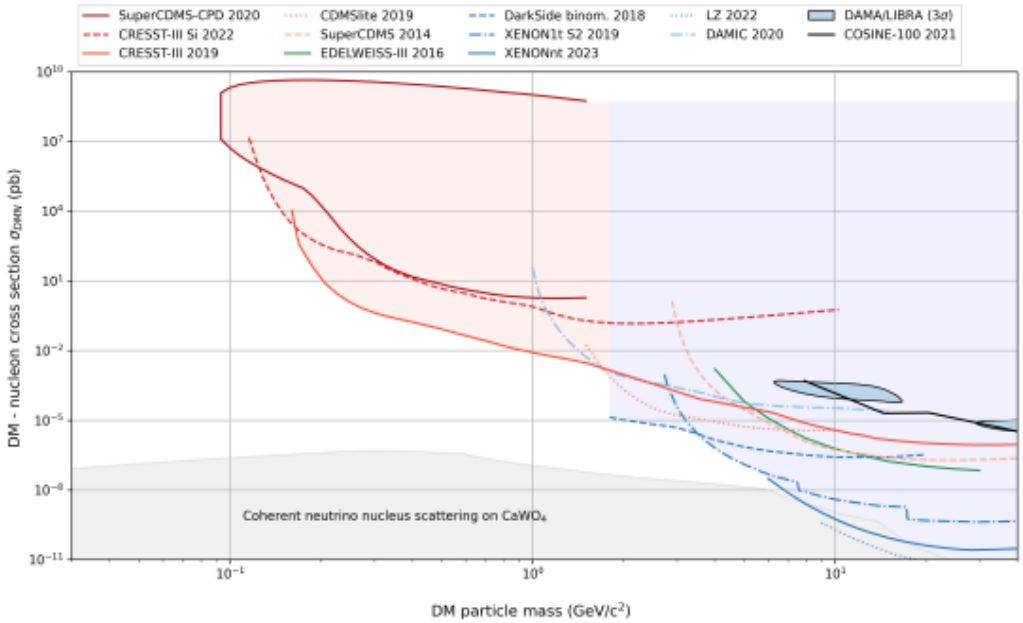

Figure 2.5: Recent CRESST limits (orange) in comparison to other experiments, taken from [59].

2.5 Current Status

As of early 2024 CRESST is one of the leading DM search experiments in the sub-GeV mass region, providing the leading limit in mass range between 130 MeV/c^2 and 1.8 GeV/c^2 [57, 3]. The best exclusion limits at higher masses are given by liquid noble gas detectors taking advantage of their large target mass to probe low cross sections: DarkSide [37], XENON1T / XENONnT [35, 58] and LZ [36]. Figure 2.5 gives an overview of the current coverage of parameter space. In recent years the goal of the CRESST experiment was to design detectors reaching lower thresholds to explore low DM masses. Threshold values as low as 10 eV could be achieved [3]. In the newly accessible energy range below ∼200 eV an unknown rise of events towards threshold could be observed in all detectors.

2.5.1 Low Energy Excess

The rise of events towards threshold at the low energies is referreded to as Low Energy Excess (LEE). It has been observed in all CRESST detectors in the past three data taking campaigns, where low thresholds below 200 eV could be reached. The LEE is characterized by a rise of events towards threshold starting at around 120–200 eV. It can be best described by a combination of different exponential or power law functions. Figure 2.6 shows a comparison of the LEE in the resent CRESST data taking campaign featuring modules of different target materials, no dependence on material or mass could

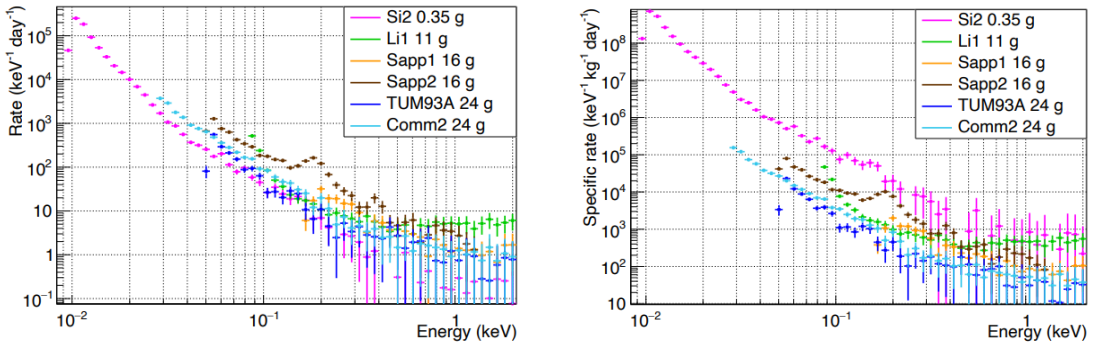

(a) Energy spectra

(b) Energy spectra scaled by mass

Figure 2.6: Energy spectra for different CRESST-III detectors scaled by measuring time (a) or exposure (b), taken from [56].

be observed [56]. A time dependent decay of the LEE events was observed in all detectors excluding a DM explanation. A fit returns similar decay times for all detectors, hinting towards a common origin [60, 61].
A LEE is not only observed in CRESST but in several low threshold experiments. It can be seen in other cryogenic experiment including EDELWEISS [62], MINER [63] and Super-CDMS [64, 65] as well as experiments using CDD detectors like DAMIC [66] and SENSEI [67]. Considering the very different nature of the experiments one common reason for its occurrence is improbable, rather, it appears to have various origins. It is of greatest interest to the low mass DM community to solve this puzzle since it is one of the greatest limiting factors concerning sensitivity.

Chapter 3

Data Analysis

The following chapter gives an overview of the data analysis methods used in the current data taking run. The methods described were used and presented in previous works including [1, 4, 68, 69]. Most of the analysis is performed using the ROOT-based [70] analysis software "Cryogenic Analysis Tool (CAT)" developed for [68]. The first section gives insight on the data selection. Section 3.2 and 3.3 show different methods of amplitude reconstruction with the help of the Standard Event (SEV) fit and Optimum Filter (OF). Section 3.4 illustrates the current software triggering of continuous data using the OF and the event building. Methods to determine the energy threshold and baseline resolution are described in Section 3.5. The following Section 3.6 explaines the energy calibration. Section 3.7 shows how the efficiency of the analysis is characterized. High level analysis is described in the final Section 3.8.

3.1 Data Selection

Not all of the continuously recorded data stream can be used for data analysis, some files contain disturbances due to technical issues or maintenance. Strong weather or geological phenomena such as earthquakes can disturb the data taking and should be excluded. Files which length is reasonable shorter than average should also be excluded. After file selection, the detector's operating stability is tested. For mapping the stability, high energetic control pulses that drive the detectors out of their transition phase are injected. If two consecutive pulses deviate from the average of the measured pulse height in the detector by 3σ the detector is classified as unstable until the pulses are within the stable region again. Unstable regions are removed from the data set. As a final step basic data quality checks are performed for each triggered event. The used analysis software calculates around 30 different parameters to characterize the recorded pulses, the most relevant for selection cuts are shown in Table 3.1. The parameters can be used to create general cuts to remove non-particle events that were triggered. The most prominent non-particle events can be seen in Table 3.2 and Figure 3.1. Additionally pulse shape discrimination cuts can be made with the help of the SEV fit (see Section 3.2) and the

OF (see Section 3.3). Since DM recoil signals are rare, time periods with high event rate are excluded.

Baseline Difference, Offset and Slope	The baseline difference, also referred to as right-left baseline, gives the difference of the signal height from samples at the beginning and end of a recorded pulse window. The baseline offset parameter gives the average signal in the baseline region. It can be determined by a linear model in most cases. The baseline slope is given by the gradient of the linear baseline model.
Pulse Height	This parameter is given by the maximum of the signal minus the baseline offset.
Minimum Derivative	The minimum derivative parameter is given by the minimum of the voltage difference between two consecutive samples.

Table 3.1: Most important main parameters for data quality selction cuts.

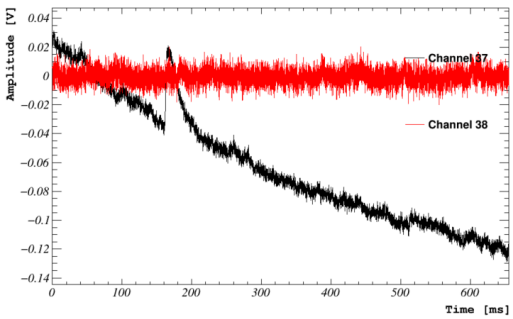

(a) Decaying baseline with pulse in Channel 37

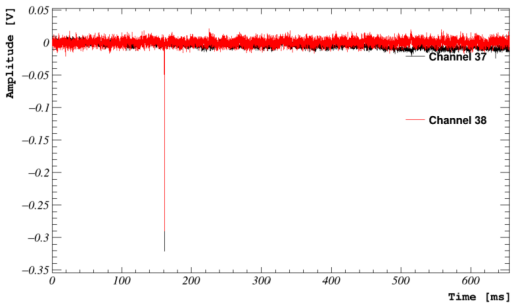

(b) Voltage spike in both channels

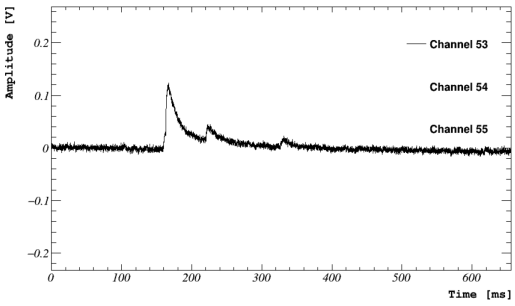

(c) Pile-up event in Channel 53

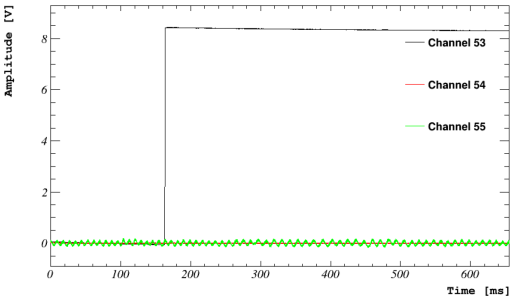

(d) SQUID reset in Channel 53

Figure 3.1: Examples for events removed by the data quality cuts in detector Comm2 and TUM93A including decaying baselines, voltage spikes, pile-up events and SQUID resets.

Decaying Baselines	The pulse data is recorded in a window with a given length. Pulses with a large amplitude can exceed the record length and be triggered if their amplitude is still above threshold. Real pulses can occur on top of the decaying baseline. They can be excluded by cutting on the baseline difference parameter.
Voltage Spikes	Voltage or delta spikes are caused by disturbances in the electronic read out. Comparing the minimum derivative parameter to the root-mean-square (r.m.s.) of the baseline creates a framework, that helps to exclude these events.
Pile-ups	Pile-up events are recorded if energy is deposited in the detector by more than one source in a short period of time. They can be excluded through comparisons that are sensitive to the pulse shape. This includes the r.m.s. obtained by the standard event fit or applying the OF.
Noise Triggers	Turbulent noise can be triggered as a particle event, if it exceeds the threshold. They can be excluded through comparisons that are sensitive to the pulse shape.
SQUID Resets and Flux Quantum Loss	The signal can exceed the range of the SQUID read out, which leads to a so-called SQUID reset and a shift of the baseline. Pulses can rise faster than the SQUID read out can follow, leading to a change in the baseline level.

Table 3.2: Types of non-particle events that should be removed.

3.2 Standard Event

The SEV characterizes the signal shape of particle or test pulse events in a detector. In the internal software CAT the pulse shape is created as a SEV template the following way. A set of pulses that contains only one class of events is selected from the data. The chosen sample is cleaned and after subtracting a linear baseline model averaged. If the sample is taken from a peak, weighting is not necessary. In CRESST analysis the pulses are take from the ^{55}Fe X-ray peak for the particle pulses and from the lowest stable Test Pulse Amplitude (TPA) for the test pulses.
To obtain a clean, noise free model of the pulse shape a parametric model can be used. It was first introduced in [71]. In this model the pulse shape is described analytically considering both the initial non-thermal photons and the thermal phonons with the rise of the temperature over the heat bath temperature. The contribution of both components is described by their amplitude and a decay time parameter:

$$\Delta T(t) = \Theta(t-t_0)\left[A_n\left(e^{\frac{t-t_0}{\tau_{in}}} - e^{\frac{t-t_0}{\tau_n}}\right) + A_t\left(e^{\frac{t-t_0}{\tau_t}} - e^{\frac{t-t_0}{\tau_n}}\right)\right] \tag{3.1}$$

where τ_{in} is the intrinsic thermal relaxation time of the film, τ_n the lifetime of the non-thermal phonons, τ_t the thermal relaxation time of the crystal. The Θ-function represents the uniform distribution of the non-thermal phonons in the absorber volume. The amplitude A consists of detector and material properties [71].
Figure 3.2 shows an example of a created standard event template and the corresponding parametric model.

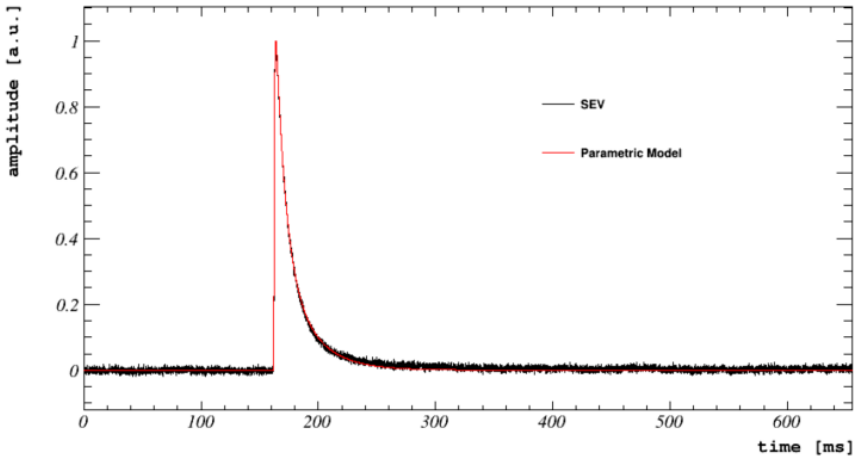

Figure 3.2: An example standard event template (black) created from the training set of the light detector of TUM93A and the corresponding parametric model (red).

To characterize the pulses a SEV fit can be performed. The template is fitted to the triggered pulses with some free parameters, including the amplitude, time shift and baseline offset. The r.m.s. of the fit givens an indication on how well the pulse shape matches the standard template and can be used to discriminate between real particle events and false triggers.
The response of the detector is only linear in the transition region of the superconducting tungsten film. Pulses at high energies will saturate and not show the accurate shape and height of the signal. This issue can be solved by only fitting the pulses below the truncation limit, the point where the transition curve stops being linear. The limit can be determined with an untruncated fit to the particle or test pulses. Saturated pulses do not match the pulse shape of the standard template and return increasing r.m.s.. For the test pulses one can observe the non-linearity by comparing the untruncated fit amplitude to the injected TPA.

3.3 Optimum Filter

An OF, often also called matched or correlated filter is a filter for optimising the Signal to Noise Ratio (SNR). The OF transfer function is designed to optimise a chosen parameter

response following the criterion of optimisation.
In the recent phase of the experiment, it has been used to optimise the triggering of low energetic particle events, the reconstructed OF amplitude gives an accurate measure of the pulse amplitude for energy calibration and can be used to characterize detector properties namely the analysis threshold and the baseline resolution.

3.3.1 Frequency Solution by Gatti and Manfredi

An approach to obtain the optimal filter transfer function was introduced in [2]. The following section includes the derivation of the OF transfer function shown in [2]: In this approach a network is considered, which leads to the optimum ratio. The output signal of such a system can be described by

$$v(t) = \frac{Q}{2\pi} \int_{-\infty}^{\infty} H(i\omega) S(\omega) e^{i\omega t} dt \tag{3.2}$$

where $H(i\omega)$ is the OF transfer function, $S(\omega)$ is the Fourier transform of a signal $QS(t)$. The r.m.s. noise for the system is

$$\langle v_N^2 \rangle^{1/2} = [\bar{v}_N]^{1/2} = \left\{ \frac{1}{2\pi} \int_{-\infty}^{\infty} N(\omega) |H(i\omega)|^2 d\omega \right\}^{1/2} \tag{3.3}$$

with $N(\omega)$ being the Noise Power Spectrum (NPS). The wanted function should maximize the ratio between value of the signal and the r.m.s. noise:

$$\rho^2 = \frac{Q^2}{2\pi} \frac{[\int_{-\infty}^{\infty} H(i\omega) S(\omega) e^{i\omega t} d\omega]^2}{\int_{-\infty}^{\infty} N(\omega) |H(i\omega)|^2 d\omega} \tag{3.4}$$

Using the Cauchy-Schwartz inequality

$$\left| \int_{-\infty}^{\infty} u_1(\omega) u_2(\omega) d\omega \right|^2 \leq \int_{-\infty}^{\infty} |u_1(\omega)|^2 d\omega \int_{-\infty}^{\infty} |u_2(\omega)|^2 d\omega \tag{3.5}$$

with

$$u_1(\omega) = H(i\omega) N^{1/2}(\omega), \tag{3.6}$$

$$u_2(\omega) = \frac{S(\omega)}{N^{1/2}(\omega)} exp(i\omega\tau_M) \tag{3.7}$$

the following relation can be obtained:

$$\begin{aligned} \frac{Q^2}{2\pi} \frac{[\int_{-\infty}^{\infty} H(i\omega) S(\omega) e^{i\omega t} d\omega]^2}{\int_{-\infty}^{\infty} N(\omega) |H(i\omega)|^2 d\omega} &\leq \frac{Q^2}{2\pi} \frac{[\int_{-\infty}^{\infty} H(i\omega) N(\omega) d\omega]^2 [\int_{-\infty}^{\infty} \frac{|S(\omega)|^2}{N(\omega)} d\omega]^2}{\int_{-\infty}^{\infty} N(\omega) |H(i\omega)|^2 d\omega} \\ &= \frac{Q^2}{2\pi} \frac{\int_{-\infty}^{\infty} |S(\omega)|^2 d\omega}{\int_{-\infty}^{\infty} N(\omega) d\omega}. \end{aligned} \tag{3.8}$$

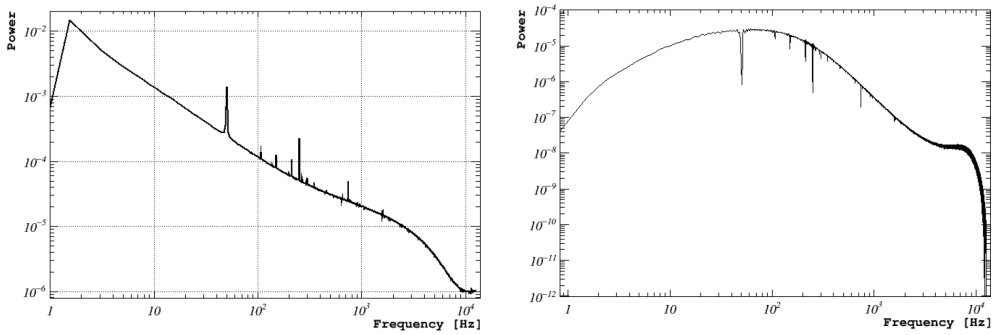

Figure 3.3: The NPS (left) and OF (right) for the phonon detector of module TUM93A.

Put in words this means passing a signal with transform $S(\omega)$ and noise $N(\omega)$ trough a linear network, the output SNR cannot exceed the integral over the whole frequency range of the ratio between the energy density of the signal and the noise spectrum.
The equality of the system is true for

$$u_1(\omega) = K' u_2^*(\omega), \tag{3.9}$$

with K' being a constant. The OF transfer function can be easily derived from it as

$$H(i\omega) = K' \frac{S^*(\omega)}{N(\omega)} e^{-i\omega\tau_M}. \tag{3.10}$$

3.3.2 Optimum Filter Creation

Following the definition of the OF transfer function, two things are needed for the creation of the OF, the pulse shape of the particle events and the noise distribution in form of the NPS.
For the SEV creation see Section 3.2. The NPS is created from a set of empty baselines. A window function is applied to each baseline, which is then Fourier transformed and the ensemble average is taken. Figure 3.3 shows the NPS of the TUM93A phonon detector. The OF is created following the transfer function in Equation 3.10. K is defined in a way that the pulse amplitude is preserved for the output of the filter. The OF kernel for the TUM93A detector is shown in Figure 3.3.

3.4 Trigger and Event Building

In DM search reaching a low threshold and gaining higher sensitivity is wanted to explore more of the parameter space. To achieve a low energy threshold the events need to be tagged as close to the noise level as possible, meaning a higher SNR leads to a lower threshold. The filtering of the continuously taken data stream reduces noise fluctuations and sets the baseline to zero.

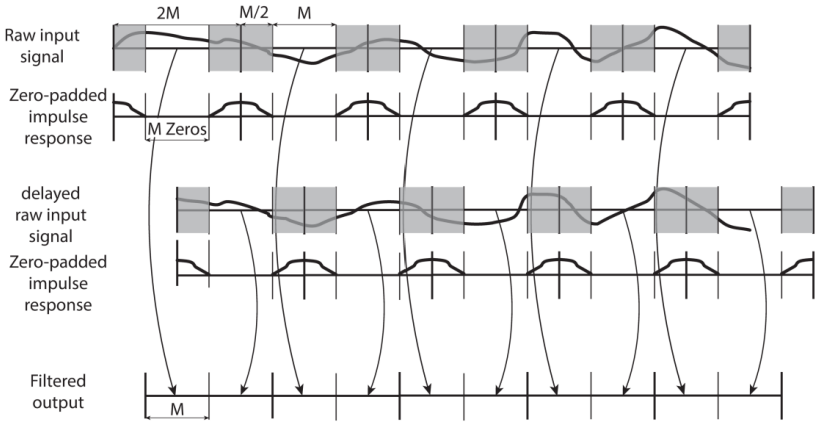

Figure 3.4: Sketch of the filtering method of the continuous data stream. The filter transfer function in time domain is zero-padded and convolved with the raw data signal, the first and last quarter of the chosen record window is discarded. The remaining samples give the filtered output. The data stream is shifted by half a record window and the process repeated allowing a full coverage of the continuous data stream. Taken from [1].

The filtering of the data can be done in two different ways. In time domain the finite impulse response filter whose kernel is the Discrete Fourier Transform (DFT) of the transfer function has to be implemented. In frequency domain the data samples need to be transformed using a DFT, then multiplied by the transfer function and transformed back. Both methods need the same number of operations. For the frequency approach Fast Fourier Transform (FFT) algorithms can be used, reducing the number of operations and making the approach more favourable to use.
The filtering of the whole continuous data stream was developed and shown in [1]: The filter transfer function with a length M is computed using the before created standard event and noise spectrum and transformed into time domain. M zeros are inserted into the middle of the function and the proximity of the insertion smoothed to avoid the creation of fake oscillations. A convolution theorem following

$$\sum_{k=-M/2+1}^{M/2} H_k y_{j-k} = \mathscr{F}^{-1}\{\hat{H}_i \hat{y}_i\}_j \tag{3.11}$$

is applied. As a last step the first and last $M/2$ samples are discarded and the data stream shifted by M to start the process again. This way the whole data stream can be filtered without anti-aliasing issues. A sketch of the method can be seen in Figure 3.4. The filtered data stream is then scanned for samples above the threshold. The sample in the center of a considered data window with a maximum value is the triggered pulse position. The maximum value is set as the amplitude of the triggered pulse. The ap-

plication of the OF to a recorded pulse can lead to oscillations on the baseline around this pulse. If the pulse is of large enough energy those oscillation can be above threshold, setting the maximum value as the amplitude avoids the misidentification of such oscillations as the actual particle pulse. The scanning for new pulses continues after the data window ended. The timestamp of the triggered event is saved. In the next step of event building the timestamps corresponding to triggered events are matched to their detector module and stored with some basic characterizing parameters. For each event the event type is classified. The trigger timestamps are compared to the timestamps of the injected heater pulses and the injected test and control pulses can be separated; they are saved with their corresponding TPA. The remaining particle events are assigned a TPA of zero. As a final step in the event building random samples from the data stream are taken and marked with a TPA of -1. Since the baseline events are drawn randomly from the complete data stream, they can contain events, that need to be removed later in the analysis.

3.5 Threshold and Resolution

To evaluate the number of noise triggers, the probability that in a time window containing only noise the maximum value of samples exceeds the threshold needs to be described. For this the noise distribution probability of noise samples filtered with the OF and a trigger window length need to be defined. The wanted probability function describes the probability to find the maximum for a set of baseline windows. For uncorrelated noise it is a binomial distribution, if assumed that the samples can be described by a Gaussian distribution.

$$P_d(x_{max}) = \frac{d}{\sqrt{2\pi}\sigma} e^{-(\frac{x_{max}}{\sqrt{2}\sigma})^2} \left(\frac{1}{2} + \frac{erf(x_{max}/\sqrt{2}\sigma}{2} \right)^{d-1} \tag{3.12}$$

The total noise trigger rate is given by:

$$NTR(x_{th}) = \frac{1}{t_{win} m_{det}} \int_{x_{th}}^{\infty} P_d(x_{max}) dx_{max} \tag{3.13}$$

In CRESST the threshold limit is currently chosen at 1 noisetrigger/kg/day [72] using a more conservative approach. The above model first introduced in [72] assumes a Gaussian noise distribution, but in some detectors a high signal rate at low energies or other non-trivial pollution necessitate a more detailed model. An exponentially rising pollution at low energies is the best fit to describe a low energy signal rate

$$\begin{aligned} P_d(x_{max}) = \lambda e^{-\lambda x_{max}} \cdot & \left(\frac{1}{2} + \frac{erf(x_{max}/(\sqrt{2}\sigma))}{2} \right)^{d-1} \\ & + (1 - e^{\lambda x_{max}}) \cdot (d-1) \\ & \cdot \frac{d}{\sqrt{2\pi}\sigma} \cdot e^{-(\frac{x_{max}}{\sqrt{2}\sigma})^2} \cdot \left(\frac{1}{2} + \frac{erf(x_{max}/(\sqrt{2}\sigma))}{2} \right)^{d-2} \end{aligned} \tag{3.14}$$

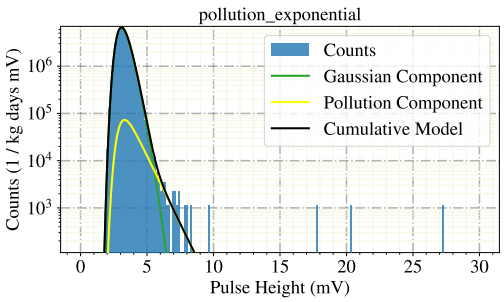

(a) The distribution of the filtered noise maximum with the best fit of the pollution model.

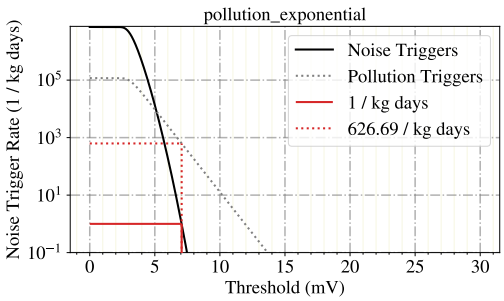

(b) The noise trigger rate and evaluation at 1 noise trigger/kg/day.

Figure 3.5: Example for the threshold determination on the TUM93A phonon channel.

as introduced in [59]. From fitting the new description to the maximum distribution, the number of noise triggers and a number of corresponding pollution triggers can be obtained.
To gain knowledge about the resolution in the low energy region of the detector, where a potential DM signal is expected, but no reference peaks can be observed in the energy spectrum, the following method is used. A standard event pulse is superimposed on a noise trace and the OF applied. The maximum of the filtered amplitude is evaluated for each trace and the variance of the combined results is taken as the baseline resolution. For low energy interactions the width of noise fluctuations is corresponding to the detector resolution. The baseline resolution can therefore also be obtained by filtering a set of noise traces and evaluating the amplitude at a set time in the record window. The distribution of the samples taken gives the baseline resolution. Both methods were first described in [1].
Both threshold and low energy detector resolution can additionally be obtained with a simulation, for more details see Chapter 3.7

3.6 Energy Calibration

In the considered data taking run the detector is calibrated using an ^{55}Fe source that is located in the detector module housing and artificially injected heater test pulses. ^{55}Fe decays via electron capture to ^{55}Mn. The characteristic emissions with the highest probability are the Kα_1 at 5.8877 keV (16.56 %), Kα_2 at 5.8988 keV (8.45 %) and K$\beta_1{}'$ at 6.49–6.54 keV (3.40 %) of ^{55}Mn [73]. The resolution of the considered detectors is not good enough in the energy region to resolve both Kα peaks individually, a single peak with energy 5.89 keV is considered. For most detectors the chosen calibration peaks are within the linear region of the detector and the amplitude of the recorded events can be reconstructed using the OF. The response of the detector is mapped using test pulses. For this, heater pulses with a defined energy are injected into the detector. They are

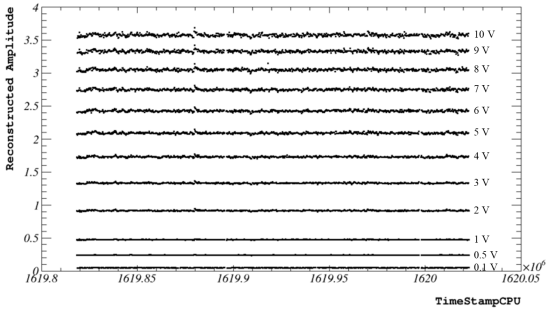

(a) Reconstructed TPA obtained using the OF over time.

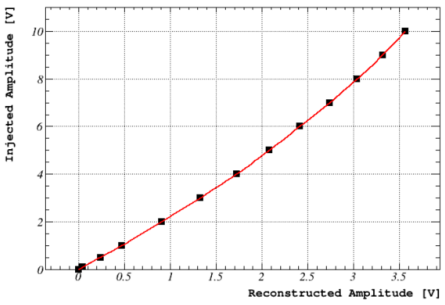

(b) Test pulse transfer function created with a gaussian spline interpolation.

Figure 3.6: TPR and example for test pulse transfer functions in the training set of TUM93A from file bck_089.

injected throughout the whole run in given time intervals, so the time dependence of the amplitude, that was reconstructed using the OF or a SEV fit, can be considered for every energy. An example of the reconstructed TPA over time can be seen in Figure 3.6a. The injected amplitude is mapped with respect to the reconstructed amplitude. For every measured particle event the Test Pulse Response (TPR) object at the measured time is constructed using a spline interpolation (Figure 3.6b) or a polynomial and the Test Pulse Equivalent (TPE) amplitude at the reconstructed amplitude can be obtained. If this is done for every particle event, the obtained spectrum of the TPE amplitude is linear to the energy spectrum and can be calibrated using the X-ray peaks at 5.89 keV and 6.49 keV from the iron calibration source with the help of the Conversion Pulse height to Energy (CPE) factor

$$CPE = \frac{E_{exp}}{A_{TPE}}, \tag{3.15}$$

where E_{exp} is the theoretically expected energy of the reference peak and A_{TPE} the position in the TPE amplitude spectrum. To calibrate the energy value of parameters in the very low energy region, the CPE factor is used in combination with the reconstructed position of the lowest stable test pulse A_{rec} compared to its injected power A_{inj},

$$\text{Conversion} = \frac{A_{inj}}{A_{rec}}. \tag{3.16}$$

The amplitude reconstruction with help of the OF can be used only in the non-saturated regime of the energy spectrum below the truncation limit. Pulses with a higher amplitude have to be corrected with the help of a SEV fit.
Figure 3.7 shows the filter amplitude of particle and test pulses in the background (bck) data set of detector TUM93A. The amplitude of the iron line matches a low test pulse injected at 2 V but reconstructed at 0.8 V, the spectrum can be reconstructed accordingly. It can be seen that the lowest amplitude test pulse matches the trigger threshold, confirming the reasonableness of the conversion factor. The broadening of

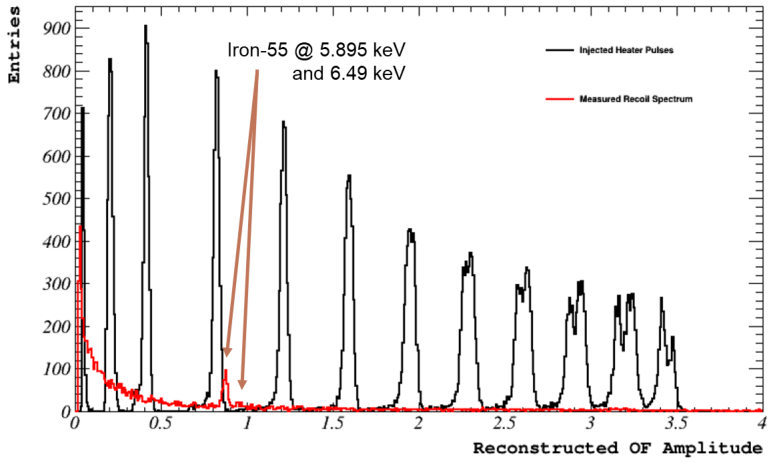

Figure 3.7: Spectrum of the reconstructed OF amplitude in detector TUM93A for the injected heater pulses (black) and the measured recoil spectrum (red) showing the iron calibration peaks at 5.89 keV and 6.49 keV.

pulses at higher amplitudes shows the unreliable amplitude reconstruction of the filter in the non-linear regime.

3.6.1 Neutron Calibration

In the previous data taking run, neutron sources were installed into the experimental setup for a given period of time and used to help define the nuclear recoil bands marking the DM acceptance region. (n,γ) interactions on the target nuclei can also be used for improved calibration of the lower energy region. The ^{55}Fe calibration source gives a calibration reference several keV above the ROI, but the most prominent tungsten recoil peaks lie around 100 eV. The deexitation of the nucleus after the capture of a neutron gives the same nuclear recoil signature as DM. For $CaWO_4$ the recoil is possible on different tungsten isotopes, but in our detectors following the branching ratios and simulations only the ^{182}W(n,γ)^{183}W interaction with a peak at 112.4 eV is observable [74]. The properties of the interaction are stated in Table 3.3. The recoil peak was first observed by the Calibrated nuclear Recoils for Accurate Bolometry (CRAB) and NUCLEUS collaboration [75].
An AmBe source with an output of ~2000 $\frac{\text{neutrons}}{s}$ was placed at a distance of ~75 cm

Isotope	Q (keV)	E_R (eV)	Y (%)	$\sigma_{n,\gamma}$ (barn)	$BR_{1\gamma}$ (%)
^{182}W	6190.7	112.4	26.50	20.31	13.936

Table 3.3: Properties of ^{182}W including the Q-value Q, recoil energy E_R, natural abundance Y, thermal capture cross section $\sigma_{n,\gamma}$ and branching ratio for single γ-emission $BR_{1\gamma}$ [76].

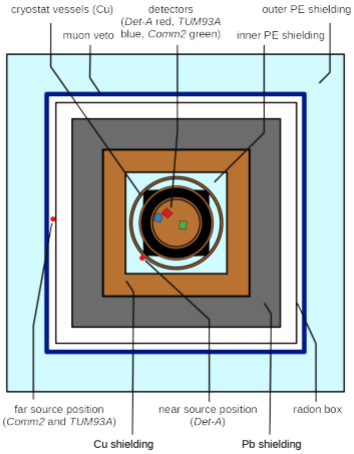

Figure 3.8: Top viewed schematic cross-section of the CRESST setup. Showing the central detector carousel in cooper with the detectors considered in blue (TUM93A) and green (Comm2) within the cryostat (concentric vessels). In- and outside of the outer cryostat is a layer of polyethylene shielding (light blue), followed by a layer of copper and lead shielding and an airtight box to shield radon gas. The outer red dot indicates the position of the neutron source. It is surrounded by a plastic-scintillator-based muon veto and an additional layer of polyethylene. Taken from [74].

from the detector modules on the outside of the radon box (see 2.1 for details on the experimental setup), resulting in a count rate of $6\,\mathrm{h}^{-1}$ in the energy range 0.1–5 keV [74]. The position of the source and the position of the detectors in the carousel are schematically shown in Figure 3.8.

3.7 Efficiency Simulation

As a final step of the raw data analysis the trigger probability of the software triggering and survival probability of the analysis are determined. The data quality, rate, stability, and muon veto cuts are designed to remove non-particle like events from a large data set. Since it is not feasible to judge the data on an event-to-event basis, general cuts are applied to remove the largest amount of non-particle events while keeping as many good events as possible. To account for the number of good events removed from the data a simulation can be performed. The simulation can also be used to determine the efficiency of the software trigger. Particle events are randomly simulated onto the continuous data stream with an amplitude in the relevant region between 0–8 keV. The continuous data stream is triggered with the simulated pulses using the OF amplitude. The data is matched with the simulation and test pulse time stamps excluding all not simulated triggers and test pulse coincidences. To account for coincidences with real particle pulses the true recorded energy is reconstructed using the TPR and CPE factor.

Using the reconstructed instead of the simulated energy places overlapping pulses at the right point in the spectrum. The survival and trigger probability are given by the fraction of simulated events surviving the trigger condition or data quality cuts. They are energy and time dependent quantities. For the trigger probability the list of triggered, simulated particle events is compared to the list containing all simulated events. The obtained probability can be fitted with an error function. The energy threshold E_{th} is taken at 50 % of the rise of the function, the detector resolution at threshold σ can also be taken from the fit function

$$f(E) = \frac{1-p_1}{2}\left[1 + erf\left(\frac{E-E_{th}}{\sqrt{2}\sigma}\right)\right] + p_2. \tag{3.17}$$

For the survival probability the data quality cuts are applied to the triggered particle list and compared to simulated pulses to show the accuracy of the cuts performed at all energies. The obtained recoil energy spectrum has to be adjusted with the survival probability.

3.8 High Level Analysis

The previous sections of the chapter showed the work flow of raw data analysis reaching up to the creation of the energy recoil spectrum, including the response of the veto detector, and the time and energy dependent survival probability. All following analyses can be considered high level analysis since it is no longer directly connected to the experimental setup and recorded data pulses and attempts to form a relation between experiment and theory. In this work it includes DM signal searches and the time and energy dependent analysis of the LEE in Section 5.2.
The first part of this section shows possible methods used to determine spin-independent DM exclusion limits including Yellin's Optimal Interval and Likelihood Method. It also shows the fit of the light yield bands to determine the acceptance region. The second part gives a short insight on positive analysis, testing for the significance of a potential discovery.

3.8.1 Exclusion Limit Calculation

The first step to obtaining an exclusion upper limit for considered DM cross sections is defining the acceptance region or ROI. For calcium tungstate detectors it is given by the mean of the oxygen band to the 99.5 % lower boundary of the tungsten band in the light yield. The band position can be extracted from a fit to the neutron calibration data.

Light Yield Band Fit

The band and energy spectrum description used in the fit are based on and derived in [77]. The electron band L_e is calibrated to set the iron calibration peak at a light yield $LY = 1$ and taking in various factors the energy dependence of the mean of the band

can be described by

$$L_e(E) = (L_0E + L_1E^2)\left[1 - L_2 \cdot \exp\Big(-\frac{E}{L_3}\Big)\right]. \tag{3.18}$$

The mean of the γ-band L_γ is slightly quenched compared to the mean of the electron band. The function has to be adjusted including the quenching factors $Q_{\gamma,1}$ and $Q_{\gamma,2}$

$$L_\gamma(E) = L_e(E[Q_{\gamma,1} + EQ_{\gamma,2}]). \tag{3.19}$$

The mean of nuclear recoil bands of O, Ca and W are given by

$$L_x(E) = (L_0E + L_1E^2) \cdot \epsilon \cdot QF_x \cdot \left[1 + f_x \cdot \exp\Big(-\frac{E}{\lambda_x}\Big)\right] \tag{3.20}$$

where QF_x, f_x and λ_x are values determined in [78], the scaling factor ϵ is determined by the band fit. The width of the bands is given by

$$\sigma_x(E) = \sqrt{\sigma_L(L_x(E)) + \frac{dL_x}{dE}\sigma_P(E)} \tag{3.21}$$

with the total resolution of the phonon σ_P and light detector σ_L.

Yellin's Optimal Interval Method

In this work the DM exclusion limits are calculated with Yellin's optimal interval approach [79]. This method has the advantage of not needing a precise description of the background but returns more conservative upper limits and cannot be used for positive analysis. The approach is a generalisation of the maximum gap method illustrated in Figure 3.9. The recorded events are shown as black squares on the x-axis, the expected DM event rate $\frac{dN}{dE}$ for a chosen cross section is shown as a black line. $\frac{dN}{dE}$ additionally includes any know background model. To set an upper limit on the cross section σ, said σ is varied until it is considered "too large", meaning the difference of experimentally recorded events to expected events is "too high" [79]. This is characterized as the size of the gap between two following events E_i and E_{i+1}

$$x_i = \int_{E_i}^{Ei+1} \frac{dN}{dE} dE. \tag{3.22}$$

Th largest x_i is considered the maximum gap x. σ is considered too large, if there is a gap x_i with a number of expected events larger than any random experiment would almost always give in its maximum gap x. If a random x_i is lower than the size of the observed x with a probability of C_0 the considered σ is rejected with the confidence level of C_0.

$$C_0(x, \mu) = \sum_{k=0}^{m} \frac{(kx - \mu)^k e^{-kx}}{k!}\Big(1 + \frac{k}{\mu - kx}\Big), \tag{3.23}$$

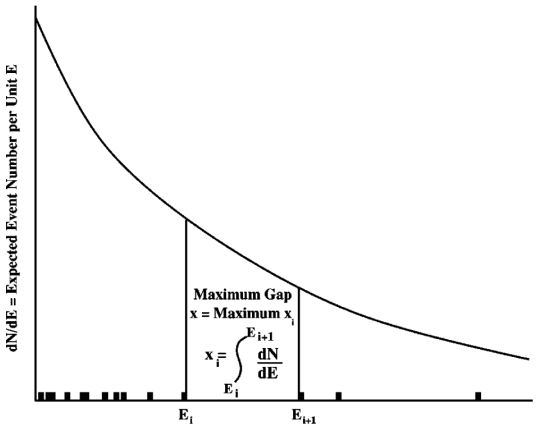

Figure 3.9: Illustrating the maximum gap method. The black squares are data points, the curve the expected event rate. The maximum gap is defined as the largest gap between two events with the highest difference between expected and observed events. Taken from [79].

where μ is the number of observed events and m is given as the greatest integer smaller than $\frac{\mu}{x}$, is derived in [79]. This approach gives best results for a small number of events for data sets with a high density the maximum gap can be replaced by the maximum interval over which there is a given number of events observed. $C_n(x, \mu)$ is defined to be the probability for a given σ that all intervals with less than n events have their expected number of events smaller than the maximum interval x. A Monte Carlo Simulation is needed to calculate the probability. For a given n the new probability can be treated like C_0, the optimum interval is given as the interval returning the highest value of $C_n(x, \mu)$ and the cross section σ meeting the confidence level exclusion limit of the discrepancy between expected and observed events can be calculated. To avoid bias the method includes a numerical calculation to determine n. It is chosen to be the n giving the strongest exclusion limit for the desired confidence level [79]. Typically a 90 % confidence level is chosen.

Likelihood Method

If the background is accurately known a better limit can be obtained using the Likelihood method. It is not necessary to define a ROI since the background is described by a parameterized model with parameters θ_b. The exclusion limit is determined for each DM mass m_{DM} individually for all relevant masses. The likelihood function for a set of model parameters describes the plausibility of the probability function of the model $\rho(x)$ to describe the observed data points x_i:

$$\mathcal{L}(\theta_b, \sigma) = \prod_i \rho(x_i|\theta_b, \sigma) \tag{3.24}$$

with σ being the DM nucleus interaction cross section. If the distribution ρ is not normalized, but the normalization depends on θ_b, in some cases the likelihood function cannot be maximized as needed. With a simple extension to the likelihood function this can be avoided [80]

$$\mathcal{L}(\theta_b, \sigma) = e^{-\nu} \prod_i \rho(x_i|\theta_b, \sigma), \tag{3.25}$$

where ν is the norm of the predicted data distribution with expected events X over the observation space A

$$\nu = \int_A \rho(X|\theta_b, \sigma). \tag{3.26}$$

To calculate the exclusion limit the likelihood ratio test can be used

$$\lambda = \frac{\mathcal{L}(\theta_b, \sigma_{exclusion})}{\mathcal{L}(\theta_b, \sigma)} \tag{3.27}$$

$\mathcal{L}(\theta_b, \sigma_{exclusion})$ gives the likelihood for the exclusion limit and $\mathcal{L}(\theta_b, \sigma)$ the best fit of the maximum likelihood if both parameters are let free. To minimize numerical calculation errors the statistical value

$$q = \begin{cases} -2\ln(\lambda) & \lambda > 0 \\ 0 & \lambda < 0 \end{cases} \tag{3.28}$$

is maximized instead of λ. Generally speaking, the higher value q returns, the higher is the incompatibility of model and data. The p-value describes the probability that a q larger or equal to the observed values, assuming σ, is true. It can be related to the statistical significance Z for a gaussian distribution

$$Z = \sqrt{2} erf^{-1}(2p - 1). \tag{3.29}$$

Wilk's theorem [81] states that q should follow a χ^2 distribution and it can be related to the statistical significance

$$Z = \sqrt{q} = \sqrt{-2\ln(\lambda)} \tag{3.30}$$

as shown in [82]. To find the upper limit with a 90 % confidence level evaluate Z for $p = 0.1$ and derive the negative logarithmic likelihood for $\mathcal{L}(\theta_b, \sigma_{exclusion})$ giving the value for $\sigma_{exclusion}$ and setting the exclusion limit on the interaction cross section for the chosen mass

$$nLL(\theta_b, \sigma_{exclusion}) = nLL((\theta_b, \sigma)\frac{Z^2}{2}. \tag{3.31}$$

3.8.2 Positive Analysis

Using the likelihood approach a positive analysis, a potential discovery calculation, can be done by comparing the best fit to a model containing no DM signal. A much higher probability is needed for a certain discovery since unknown background components can mimic the DM signal and lead to a false discovery or falsely high significance.

Chapter 4

Signal Processing

A filter is defined as a device that discriminates, based on a given attribute, what passes through it. A digital filter is a mathematical operation on a digital signal to reduce or enhance selected signal. Using a Linear Time-Invariant system (LTI) it is possible to design a filter that passes and attenuates selected frequencies. In a LTI the frequency response can be obtained by taking the Fourier transform of the time response. These filters are used in multiple different ways: to remove noise from signal, for spectral shaping, for signal detection in radar, sonar and communication or to perform spectral analysis of a signal [83, 84]. This chapter gives a short overview of basic digital filters and explores their usage to alter the OF for potentially enhancing detection sensitivity.

4.1 Digital Filtering

The filter types, considered in the following, consist of a pass, stop and transition band region. The pass band describes a range of frequencies, where the signal passes through the filter. The stop band describes the frequency range, that attenuates the signal. Within the transition band the cut-off frequency describes the frequency at which the suppression is at 70 % and the roll off describes the slope between start and end frequency.
In a Low Pass Filter (LPF) the pass band lies at frequencies below the cut-off frequency. A High Pass Filter (HPF) is the complement of a LPF and the pass band lies at frequencies above the transition region. Combining the two a Band Pass Filter (BPF) can be created that passes the signal between two frequencies, as well as a band stop filter, that attenuates the signal for a normally small frequency range. The amplitude over frequency response of the filters are sketched in Figure 5.4 and the effect of a LPF and HPF on a sine signal with artifical noise shown in Figure 4.2.
An ideal LPF would pass all frequencies below the cut-off frequency without change and stop all frequencies above. In frequency domain it is represented by a rectangular

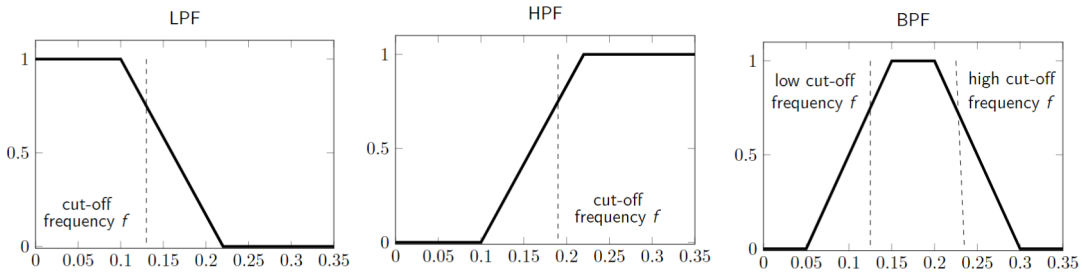

(a) LPF (b) HPF (c) BPF

Figure 4.1: Sketch of (a) a LPF passing frequencies lower than cut-off frequency f, (b) a HPF passing frequencies higher than cut-off frequency f and (c) a BPF created by cascading a LPF and HPF. The cut-off frequency at a 70 % level supression is indicated with a dashed line.

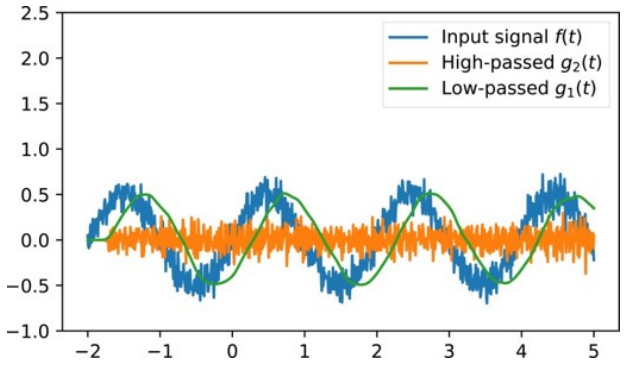

Figure 4.2: Illustration of the effect of a LPF and HPF on a noisy sine function. A strict LPF will remove the high frequency noise, but blurs out the time response. A HPF will remove the lower frequency sine function. Taken from [85]

function

$$TP = \begin{cases} 1 & |f| \leq f_c \\ 0 & \text{otherwise} \end{cases},$$

where f is the frequency and f_c the cut-off frequency. However, its response in time domain, the sinc function, is of infinite length, the processed signals would also need to be of infinite length in time. In reality this is not achievable and filters with a transition region are used [86]. In this study a decaying exponential function in time domain is used. Other well used examples include Butterworth [87] and Bessel filters [88].
The filters applied in frequency domain can cause several artifacts and effects on the signal in time. The low pass filter can blur out the time signal, most notable in onset and offset times. The high pass filter creates a negative peak for positive peaks in the signal. These effects can be neglected, since for OF creation in CAT the shape of the template pulse representing the signal does not need to be conserved.

4.2 Optimum Filter Modification

The current OF function follows the pulse shape while suppressing features characterized by the noise spectrum, e.g. a spike at a frequency of 50 Hz from the power supply. The characteristic of the pulse shape lies roughly in the region between 10–100 Hz. The lower frequencies are characterized by slow baseline fluctuations, that can be caused by trucks and cranes in the closer area of the experiment, while the higher frequencies are dominated by electronics noise. In theory suppressing these frequencies further could lead to an improvement of the SNR. Additionally the current creation method of the OF creates a rise of the filter function at high frequencies due to division of small numbers, not representing the true characteristic of the noise and pulse shape [1]. To create a new filter, that cuts on the frequencies of the OF containing mostly noise information and computation artifacts, the previously described filter types can be applied to the original OF. The filters were applied on the template pulse for initial accessibility reasons in the analysis software, considering the definition of the filter in Equation 3.10 this is valid.

$$\begin{aligned} H_{modified}(i\omega) &= H(i\omega) \cdot BP(\omega) \\ &= K' \frac{S^*(\omega)}{N(\omega)} e^{-i\omega\tau_M} \cdot BP(\omega) \\ &= K' \frac{S^*(\omega) \cdot BP(\omega)}{N(\omega)} e^{-i\omega\tau_M} \\ &= K' \frac{S^*_{modified}(\omega)}{N(\omega)} e^{-i\omega\tau_M}. \end{aligned} \tag{4.1}$$

The analysis was done in ROOT using the Fast Fourier Transforms Interface and CAT software. A previously created SEV template was transferred from time into frequency domain using a Fourier transform:

$$S(\omega) = \int_{-\infty}^{\infty} S(t) e^{-i\omega t} dt. \tag{4.2}$$

Here $S(t)$ is the signal in time domain and $S(\omega)$ in frequency domain. The resulting template is multiplied with the wanted filter in frequency domain. A basic filter corresponding to an exponential function in time domain was used. For the LPF

$$\mathrm{LP}(\omega) = \frac{1}{1 + i\omega t_l} \tag{4.3}$$

with t_l being the time corresponding to the cut-off frequency f_l of the LPF, was applied. The HPF is then given by

$$\mathrm{HP}(\omega) = 1 - \mathrm{LP}(\omega) = \frac{i\omega t_h}{1 + i\omega t_h} \tag{4.4}$$

with t_h being the time corresponding to the cut-off frequency f_h. The BPF follows as

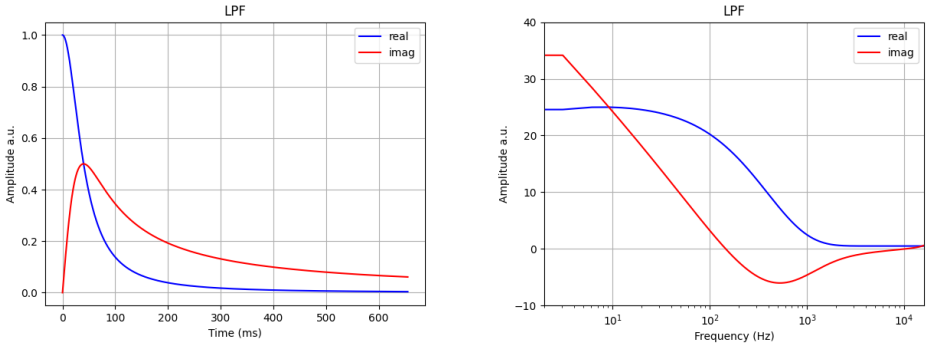

(a) LPF

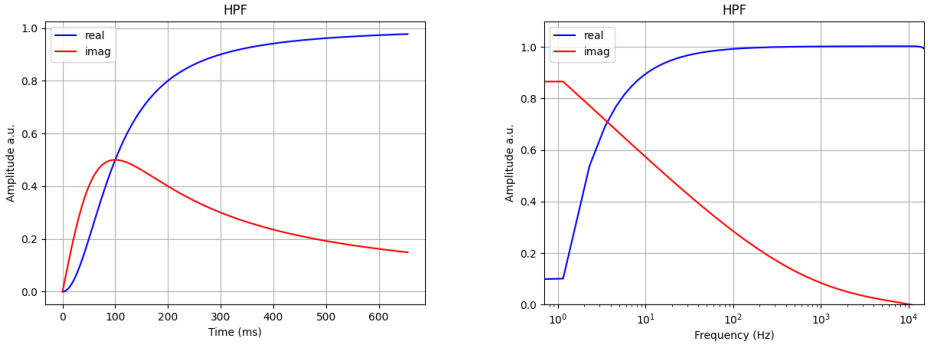

(b) HPF

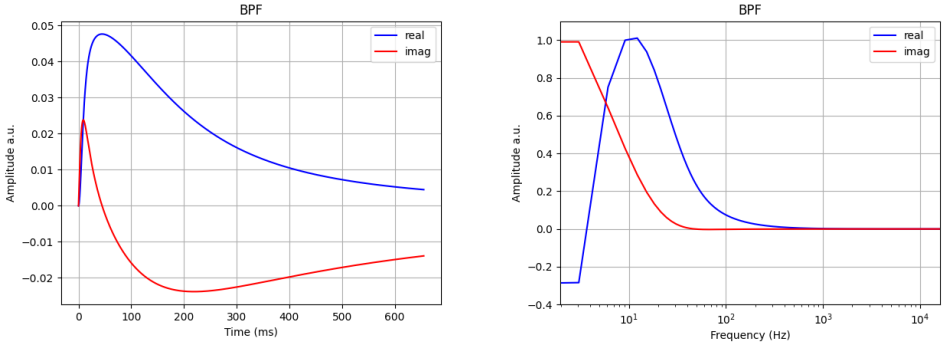

(c) BPF

Figure 4.3: Example sketch for the different types of pass filters used, showing the time (left) and frequency (right) domain. The blue curves indicate the real part and the red curve the imaginary part of the filter function.

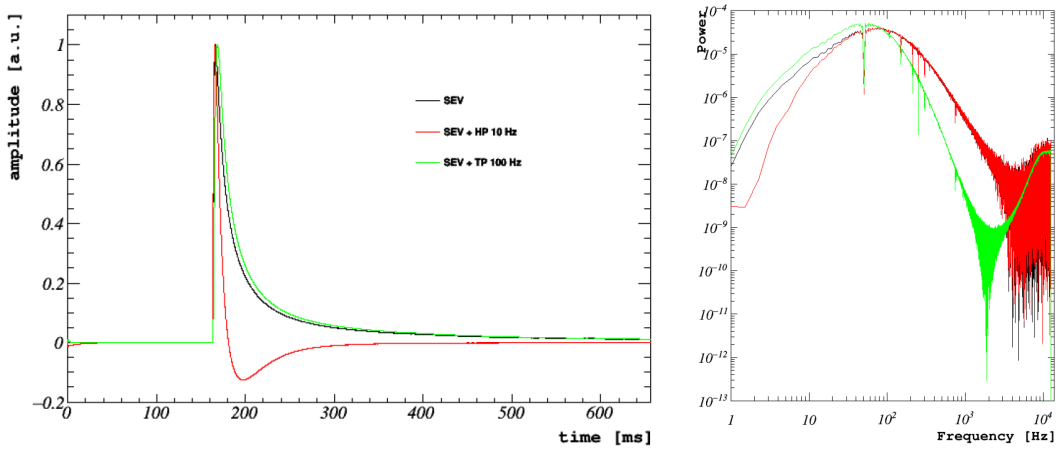

(a) Filtered SEV (b) Filtered OF

Figure 4.4: Modified SEV and OF created from TUM93A phonon channel. The black curve shows the original OF, the green one with an additional LPF and the red one includes a HPF. The HPFed SEV shows the typical undershoot after the peak, in the LPFed one the blurring of the time signal can be seen.

$$\mathrm{BP}(\omega) = \mathrm{LP}(\omega) \cdot \mathrm{BP}(\omega) = \frac{i\omega t_h}{(1 + i\omega t_h)(1 + i\omega t_l)}. \tag{4.5}$$

An example for all used types of filter functions is shown in Figure 4.3. The filtered template is transformed back into time domain using the inverse Fourier transform. The resulting new template pulse is used to create an OF within CAT. Figure 4.4 shows an example for the effect of HPFs and LPFs on the TUM93A phonon channel data. The application of LPFs generally introduces a rise of the filter kernel at the very high frequencies going against the intention of reducing the artificially created rise due to division of high numbers but having the same origin. The effect is countered by adding HPFs lowering the rise. They also introduce a rise of the low frequencies up to 100 Hz, enhancing low frequency disturbances as well as the pulse signal.

4.3 Analysis Method

In the following for all detector modules only the phonon channel was analysed. Due to computational issues not the whole analysis was done on all detector modules. The data was triggered using thresholds and OFs from previous analyses [69, 59, 4, 89, 90, 91]. The new filter was applied to the particle event list and the relative resolution of the iron line visible at 5.89 keV and 6.49 keV was determined by fitting the peak with a Gaussian function and comparing the width of the peak by the sigma of the fit to its position or the distance between both iron peaks. As a last step the energy spectrum was calibrated using the newly created filter. A Gaussian spline interpolation and test pulses of all injected energies were used to create the TPR object. The absolute

Module	used bck data files	ϵ(kg·days)	previous analysis
TUM93A	(003–008), 018, 028, 039, 048, 058, 078, 089	0.655	[4]
Comm2	(040–044), 048, 058, 078, 089	0.318	[89]
Li1	(040–044), 048, 058, 078, 089	0.164	[59, 90, 91]
Li2	(040–044), 048, 058, 078, 089	0.164	[59, 90, 91]
Sapp2	(003–008), 018, 028, 039, 048, 058, 078, 089	0.35	[69]

Table 4.1: The training data sets used for each detector and the corresponding exposure ϵ. The last column gives reference to the previous analyses the OF and SEV were taken from and data quality cuts were inspired by.

Module	used ncal data files	ϵ(kg·days)	previous analysis
TUM93A	(005–022)	0.89	[4]
Comm2	002, (004–012)	0.48	[89]

Table 4.2: The neutron calibration data sets used for each detector and the corresponding exposure ϵ. The last column gives reference to the previous analyses the OF and SEV were taken from and data quality cuts were inspired by.

resolution was determined with a binned fit on a histogram. The energy threshold and baseline resolution were determined following Section 3.5 using the iron or neutron calibration source for calibration. The threshold was determined with the help of the CAIT software package [92]. For the LPF a range of frequencies from 25 to 1000 Hz was explored, corresponding to a time of 1 ms (approaching 0 s) up to about the decay width of the pulse. For the HPF a time range from half of the decay width up to half the record length, corresponding to frequencies 3 to 13 Hz, was explored.

4.3.1 Data Selection

The data sets and exposure used for each detector are shown in Table 4.1 and 4.2. The used data essentially follows the advised training and neutron calibration data set for each channel using a similar duration of data taking for each detector leading to slightly different exposures, but of the same order of magnitude. The training data set describes a selected data set, that is used to train data cuts and templates, which are later applied to the full blind data set to avoid introducing a bias into the analysis. The training data set for detectors Comm2, Li1, Li2 differs from other detectors, since their operating point had to be changed during the beginning of the data taking run. Basic data quality cuts were applied to each detector following Section 3.1 and are shown in Figures A.1–A.5. The data cuts were oriented on the style of different analysts and can differ in strictness. They include the same parameters for each detector, providing a basic cleaning for the artifacts named earlier. The cuts focus on voltage spikes and baseline parameters, allowing a very basic cleaning of the data. Additionally a stability

cut was applied. For the purpose of the study it was not needed to perform an efficiency simulation.

4.4 Energy Reconstruction using ^{55}Fe Peak

In the first analysis run the calibration of the spectrum was done using the standard iron calibration peak. The resolution and position of the Kα peak could be determined reliably for all applied filters. In the low energy region the values of the considered parameters showed high uncertainty originating in a newly introduced non-linearity of the TPE amplitude, making the iron escape peak an unreliable calibration reference for the ROI. In addition to basic filters, the same filter type of higher order was applied after to further explore the issue and characterize the changes in energy reconstruction.

4.4.1 Resolution at Higher Energies

The resolution at higher energies was determined as the variance of a Gaussian fit to the calibration peak from the ^{55}Fe source at 5.89 keV. In the tested detectors an improvement of the relative and absolute resolution of the iron line was seen. The improvement and frequencies for the relative resolution, obtained by comparing the variance of the iron peak to its position or the distance between both iron peaks and absolute calibration results, are shown in Table 4.3. Figure 4.5 shows a comparison of the calibrated recoil spectrum between the standard OF and the altered filter returning the best result. For both modules made of lithium aluminate the second iron peak was not resolved enough to determine its position precisely. The best possible result was obtained by applying a LPF or a BPF with a low value for the high cut-off frequency.

Module	k_{dis}(%)	f(Hz)	k_{pos}(%)	f(Hz)	σ_0(eV)	σ_f(eV)	k_{abs}(%)	f(Hz)
TUM93A	9.35	4–67	9.73	<50	87.40	79.62	8.9	<33
Comm2	24.61	<33	10.55	<25	96.62	82.90	14.2	<50
Li1	-	-	13.74	3–50	191.11	167.12	12.6	3–200
Li2	-	-	4.52	7–50	176.51	163.18	7.5	<100
Sapp2	16.22	4–33	11.72	3–25	107.04	92.78	13.3	4–33

Table 4.3: The best obtained relative resolution improvement for distance k_{dis} and position k_{pos} with the frequency range f allowed by the filter is shown in the left part. The comparison method based on distance was not possible for the lithium aluminate modules. The right part shows the absolute resolution improvement k_{abs} with the corresponding frequency range f. The obtained resolution are σ_0 for the original OF and σ_f for the modified filter.

In general better results were seen for LPFs rather than HPFs, implying that the resolution at higher energies is partly limited by electronic noise or the artificial rise in the filter and can be improved by cutting on the high frequencies. It can be seen that the

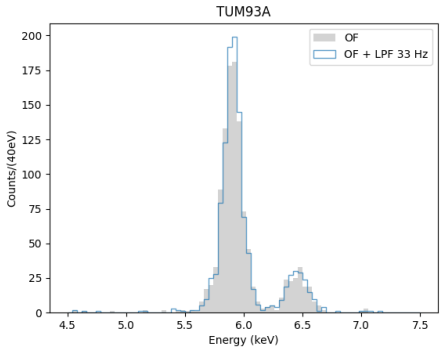

(a) TUM93A $f_l = 33\,\mathrm{Hz}$

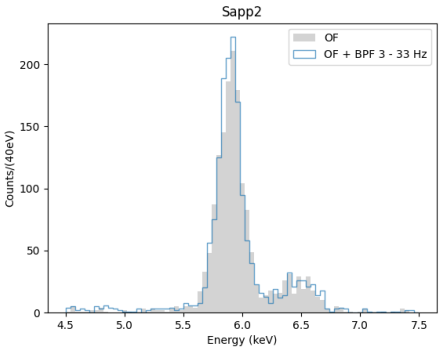

(b) Sapp2 $f_l = 33.3\,\mathrm{Hz}$ & $f_h = 4\,\mathrm{Hz}$

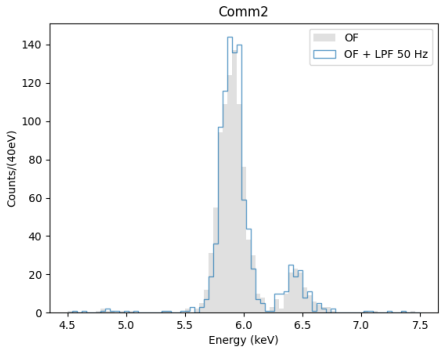

(c) Comm2 $f_l = 50\,\mathrm{Hz}$

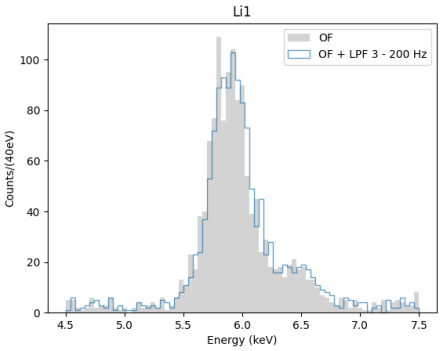

(d) Li1 $f_l = 200\,\mathrm{Hz}$ & $f_h = 3.3\,\mathrm{Hz}$

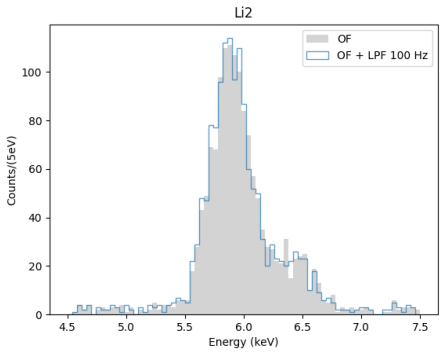

(e) Li2 $f_l = 100\,\mathrm{Hz}$

Figure 4.5: The calibration spectrum in the region of the iron peaks using the original OF (grey) and a modified filter with cut-off frequencies f_l and f_h (blue). A slight improvement of the resolution is calculated for all detectors.

estimation methods give a good approximation to the resolution improvement without the need to calibrate the spectrum.

4.4.2 Low Energy Region: Threshold and Resolution

The energy threshold was determined using the standard method described in Section 3.5 as having one noise trigger per kilogram per day of exposure, assuming the standard probability. An improvement of the calculated energy threshold value can be seen in the considered detectors, when using the determination and calibration method mentioned above. Generally better results are obtained for HPFs. For the calcium tungstate modules an improvement is also seen using LPF. The results are shown in Table 4.4 and Figure 4.6. The error shown for the new threshold values E_{thr} represents only the

Module	$E_{thr,0}$(eV)	E_{thr}(eV)	f(Hz)
TUM93A	51.48	50.49±1.19	<100
Comm2	28.03	22.73±6.52	>12.5
Sapp2	55.31	51.48±4.67	>10
Li1	87.63	85.05±1.78	>3

Table 4.4: The recalculated energy threshold in this work $E_{thr,0}$, the optimized threshold E_{thr} and the corresponding cut-off frequencies f. The error is given by the non-linear deviation of the calibrated energy spectrum.

minimum estimated uncertainty originating in the non-linearity of the energy calibration using the modified filters. The uncertainty is characterized by the deviation of the iron peak, in the plane between the old and new energy calibration, to its expected position taken from an extrapolation of the linear low energy region. In the calibrated recoil spectrum in Figure 3.5 the misplacement of structures, e.g. the peak at around 180 eV in Sapp2, can be seen. The origin of the peak is not certainly known, for a discussion of possible origins see [69].
The baseline resolution was calculated by superimposing a particle pulse with a defined energy of 200 eV onto a set of empty baselines individually, then determining the resolution of the amplitude of the reconstructed pulses. The results are shown in table 4.5.

Module	$\sigma_{bl,0}$(eV)	σ_{bl}(eV)	f(Hz)
TUM93A	7.86±0.01	7.87±0.10	<200
Comm2	4.26±0.03	3.49±1.08	>12.5
Sapp2	7.21±0.09	6.76±0.50	>10

Table 4.5: The recalculated standard baseline resolution in this work $\sigma_{bl,0}$, the optimized resolution σ_{bl} and the corresponding cut-off frequencies f. The error of σ_{bl} is given by the non-linear deviation of the calibrated energy spectrum. The error of $\sigma_{bl,0}$ is the uncertainty of the Gaussian fit.

An improvement of the baseline resolution value can be seen in the Comm2 and Sapp2

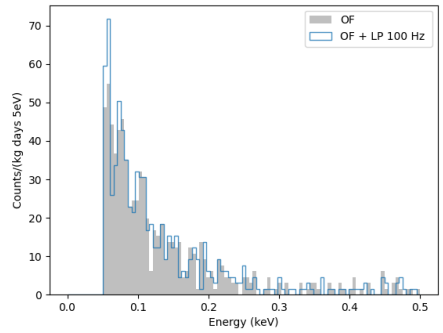

(a) TUM93A $f_l = 100\,\mathrm{Hz}$

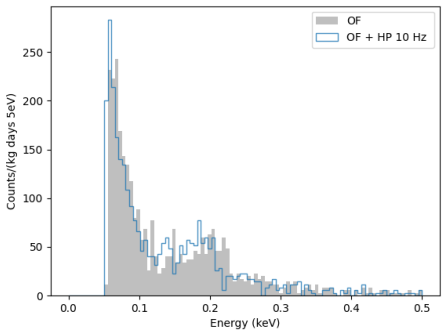

(b) Sapp2 $f_h = 10\,\mathrm{Hz}$

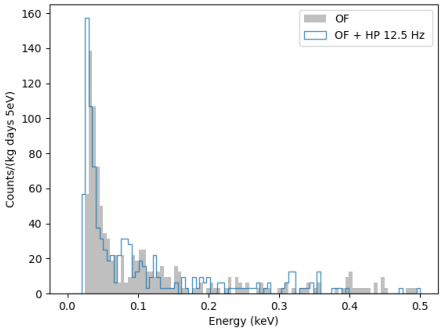

(c) Comm2 $f_h = 12.5\,\mathrm{Hz}$

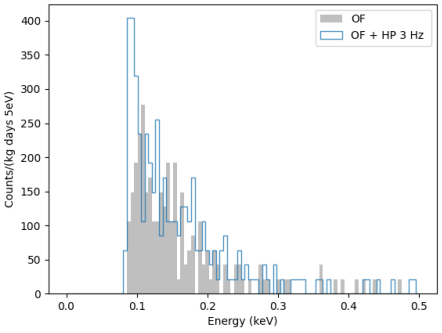

(d) Li1 $f_h = 3\,\mathrm{Hz}$

Figure 4.6: The calibrated energy spectrum at energies below 500 eV using the original (grey) and modified filters with f_l and f_h (blue). The threshold is lowered in all detectors except TUM93A. The peak-like structure at around 180 eV in (b) is shifted to lower energies.

module by applying a HPF to the OF with cut-off frequencies $f_h = 12.5\,\mathrm{Hz}$ and $f_h = 10\,\mathrm{Hz}$ but with a high uncertainty in energy calibration. In the TUM93A module the same resolution could be achieved within error. The reconstructed amplitude is increasingly lower than the initially superimposed amplitude for decreasing cut-off frequencies. For both low energy parameters cutting on high frequencies worsens the outcome with decreasing cut-off frequency. An "over filtering" of the electronic noise is returning a worse sensitivity and the artificially introduced noise fluctuations seem to show no significant negative effect on the analysis. The origin of the apparent reduction of the energy threshold relates to a distortion of the energy calibration caused by the additional filter. The spectrum obtained with the new filter is linear to the energy spectrum only for low energies. The iron peak can no longer be used as a reliable calibration point. The comparison of the calibration with and without the "best" performing additional filter can be seen in Figure 4.7 for the Comm2 detector module. Cutting on low frequencies,

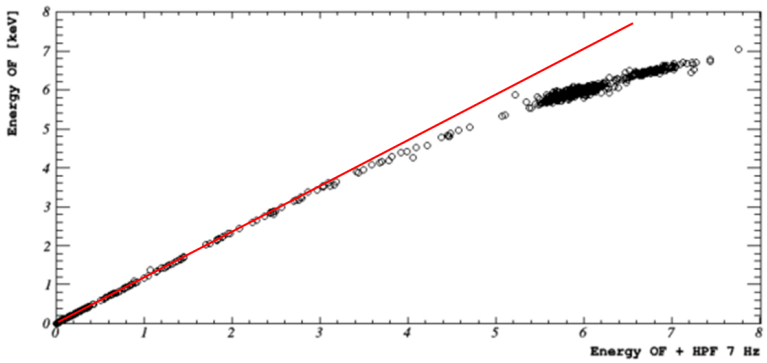

Figure 4.7: Reconstructed energy spectrum using the modified OF, that gives the best threshold result against the original energy scale for Comm2. The red line represents the extrapolation of the linear dependence below 1 keV. The energy reconstruction using the modified filter is visibly non-linear compared to the original.

applying additional HPF, shows the greatest effect on the energy reconstruction. The lowest obtained threshold values correspond with the highest non-linearity in energy calibration. The deviation increases with more invasive cut-off frequencies, raising the question whether the chosen values are too invasive and already cut on pulse information. Speaking against this is that the effect can already be seen in very small frequency ranges being cut and is not observed in all modules. The strongest deviation up to almost 28 % from the linear energy spectrum can be observed in the Comm2 module. TUM93A shows almost no non-linearity, but also no improvement in threshold or low energy resolution. Given these results a material dependence of the effect can be excluded with a high probability. TUM93A returns the lowest calculated values for LPFs, but seeing the small improvement as well as overall small changes in values and similar uncertainty no significant conclusion can be drawn on the influence of different filter types and frequencies. In contrast to the other modules none of the additional filters effect the analysis outcome significantly.

4.4.3 Higher Order Filter

For a more extensive study, filters of higher order were applied to the OF to study the change in low energy parameters and energy calibration. Considering that an improvement for the low energy parameters σ_{bl} and E_{thr} can be seen for mostly HPFs, they were chosen for applying the higher orders to the OF, to create a higher suppression of the frequencies below the cut-off frequency. The uncertainty in energy calibration seemingly increases with more invasive cut-off frequencies, having a filter allowing more frequencies but cutting the power of the filter kernel to a lower level could lead to a better result. The effect on the filter kernel can be seen in Figure 4.8. With increasing order the suppression increases, for a fifth order HPF it is about three orders of magnitude. The obtained resolutions and thresholds using the described filters, along with

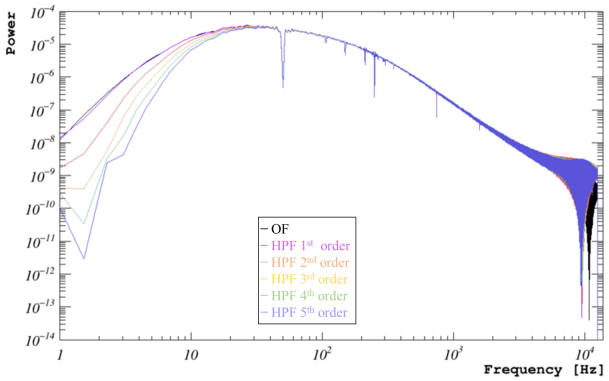

Figure 4.8: The effect of applying higher order HPFs up to the 5th order with $f_h = 5\,\mathrm{Hz}$ to the OF for detector TUM93A. The low frequencies are increasingly suppressed with increasing order up to three orders of magnitude.

the reconstructed energy of the simulated pulse for the baseline resolution are shown in Table 4.6. The pulses to determine the baseline resolution were simulated at a voltage theoretically corresponding to an energy of 200 eV. In Sapp2 and Comm2 a greater improvement of the threshold and baseline resolution can be seen with a higher order filter applied, while the resolution of the iron line worsens. The improvement in baseline resolution corresponds to the reconstruction of the peak at lower energies and an increasing non-linearity of the energy reconstruction. In Comm2 a sharp increase in resolution and threshold improvement can be seen for the second order filter along with an increase in energy calibration uncertainty. In case of the TUM93A detector both the iron and baseline resolution worsen for higher orders. The reconstructed amplitude of the simulated pulses differed from the injected as shown in Figure 4.9, the modified OF reconstructed the amplitude at lower values for higher order filters, the deviation is not

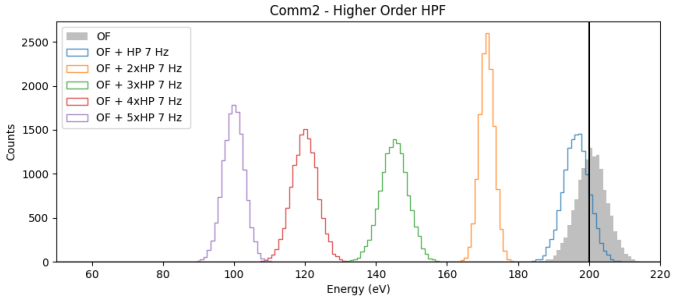

Figure 4.9: The reconstructed amplitude of pulses simulated at a voltage corresponding to 200 eV for higher order HPF with $f_h = 7\,\mathrm{Hz}$ in detector Comm2. The black line indicates the simulated energy.

$\mathcal{O}$(HP)	σ_{Fe}(eV)	σ_{bl}(eV)	A_{inj}(mV)	A_{recon}(eV)	E_{thr}(eV)
0	107.04	7.21	72.17	202.59	55.31
1	126.67	6.76±0.50	74.87	195.52	51.48±3.83
2	148.01	6.14±1.17	79.64	181.04	44.38±8.46
3	183.18	5.58±1.85	85.01	166.92	39.77±13.22
4	188.52	5.44±2.12	84.41	154.13	38.40±14.98
5	156.06	5.79±2.35	77.23	142.75	40.37±16.41

(a) Sapp2 $f_h = 10\,\mathrm{Hz}$

$\mathcal{O}$(HP)	σ_{Fe}(eV)	σ_{bl}(eV)	A_{inj}(mV)	A_{recon}(keV)	E_{thr}(eV)
0	87.40	7.86	29.89	198.98	51.42
1	103.22	8.22±0.29	40.45	185.49	54.17±1.91
2	113.39	28.45±1.07	8.18	188.45	196.94±7.42
3	120.95	28.47±1.62	7.74	170.24	203.68±11.60
4	122.29	27.60±2.98	7.16	153.71	215.04±23.20
5	132.69	22.23±2.87	6.31	142.73	238.90±30.82

(b) TUM93A $f_h = 5\,\mathrm{Hz}$

$\mathcal{O}$(HP)	σ_{Fe}(eV)	σ_{bl}(eV)	A_{inj}(mV)	A_{recon}(eV)	E_{thr}(eV)
0	94.03	4.26	56.26	200.15	28.03
1	162.78	3.55±0.77	66.46	194.75	23.33±5.08
2	332.12	2.08±2.65	109.01	172.03	13.83±17.63
3	161.44	3.85±1.41	55.94	144.91	25.57±9.35
4	123.85	3.65±2.19	56.84	120.72	23.99±14.38
5	304.10	3.00±3.54	66.63	100.27	19.72±23.24

(c) Comm2 $f_h = 10\,\mathrm{Hz}$

Table 4.6: Results for resolution of the iron calibration peak σ_{Fe} and baseline σ_{bl} and energy threshold E_{thr} for higher order HPF. The reconstructed amplitude of the simulated pulses for obtaining the baseline resolution A_{recon} and injected Amplitude A_{inj} are also shown. The first column gives the order of applied high pass filter O(HP).

solely based on the energy calibration, but both effects originate from the same false amplitude reconstruction of the new filter.

4.5 Energy Reconstruction using Tungsten Peak

The additionally applied filter introduces a non-linear uncertainty in the reconstructed energy for energies above around 1–3 keV depending on the filter and detector, while the region below appears to be not or only slightly affected. In the current run a neutron calibration source was used during part of the run to characterize the nuclear recoil bands of the detectors. For the first time a low energetic peak following the

recoil of neutrons on ^{182}W could be clearly observed. For more details on the neutron calibration see Section 3.6.1. The energy of the peak at around 112.4 eV falls within the still linear region of the spectra obtained using the new filters. In the following section the behaviour of the tungsten peak in the iron-calibrated spectra was determined to gain another characterization of the newly introduced uncertainty in energy calibration. In the second part the peak was used to calibrate the energy and obtain a less flawed result for the low energy parameters. In the final section the parameters were determined through the trigger simulation.

4.5.1 Tungsten Peak in Iron-calibrated Data

The analysis of the neutron calibration data was redone using templates from the previous analysis [74, 4, 89], following the style for data cuts from the previous section (see Figures A.6 and A.7). The results agree within only small deviations. The analysed data set contains 0.48 kg · d of exposure for Comm2 and 0.89 kg · d for TUM93A, the files used are shown in Table 4.2. As a next step the analysis was done with filters modified with a HPF of different cut-off frequencies, these filters were chosen, since HPF returned an improvement on the lower energy range in module Comm2. LPF were applied as a cross-check and to study the deviating behaviour of TUM93A compared to the other modules. The data set was calibrated using the iron peak and the position of the tungsten peak obtained by performing a likelihood fit on the low energy region using a constant and an exponential function that describe the LEE in the region of the peak with a simple model following the same method and using analysis code developed for [74]. The fit includes a constant background component and for TUM93A an additional exponential component to characterize the LEE shape more reliably. For simplicity the fit was done assuming a flat cut efficiency of 0.4. The determination of the tungsten recoil peak for the standard filter using this method is shown in Figure 4.10. The tungsten peak in TUM93A could not be resolved as nicely and with lower significance. For the sole purpose of comparison of this analysis the obtained resolution and significance is sufficient. The results for different HPF and LPF are shown in Table 4.7 and an example of one HPF and LPF for Comm2 in Figure 4.11. The error of $\sigma_{(n,\gamma)}$, E_{thr} and $E_{(n,\gamma)}$ contains the uncertainty in energy calibration seen by the position of the tungsten peak. For error of $E_{thr,bck}$ see the section before.

In Comm2 the position of the fitted recoil peak does not match the expected energy for the modified filters. In case of a HPF the energy is reconstructed lower, in case of LPF the peak is shifted higher. The recoil peak is not resolved for the cut-off frequency $f_l = 33$ Hz. The position of the tungsten recoil peak shifts from its intended energy with increasing strictness of the cut-off frequency. Confirming the increasingly inaccurate energy reconstruction.

In TUM93A the position of the peak is roughly stable, but the resolution and goodness of fit is worse in all modified filters, returning results with high error and low significance. The threshold value is increased for all additionally applied filters, but to roughly the same value. There is only a small frequency dependence observable for the thresholds.

Comparing the TPE amplitude reconstructed with the original OF against the recon-

struction with a HPF in Figure 4.12 shows a clear deviation from the expected linearity, as well as an uncertainty in reconstruction in Comm2. Both amplitudes were reconstructed to be linear to the absolute energy scale with an uncertainty. Both considered data sets, background data and data taken with a AmBe source present, show similar behaviour in both modules. In TUM93A only a small non-linear deviation of the energy scale is observed.

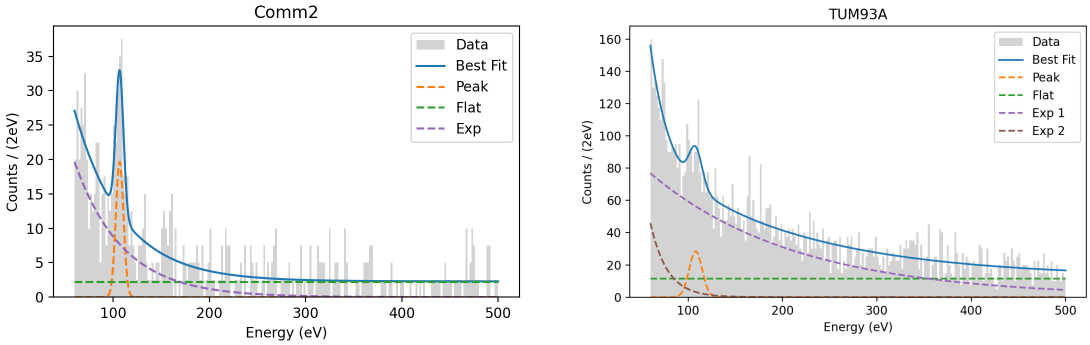

(a) Comm2 (b) TUM93A

Figure 4.10: Fit for determination of the tungsten recoil peak using the standard filter illustrating the method. In both modules the fit included the peak in form of a Gaussian function (orange), a flat constant (green) and an exponential function (purple) to account for background events of the installed source, for the TUM93A a second exponential function (brown) was included to more accurately describe the excess shape.

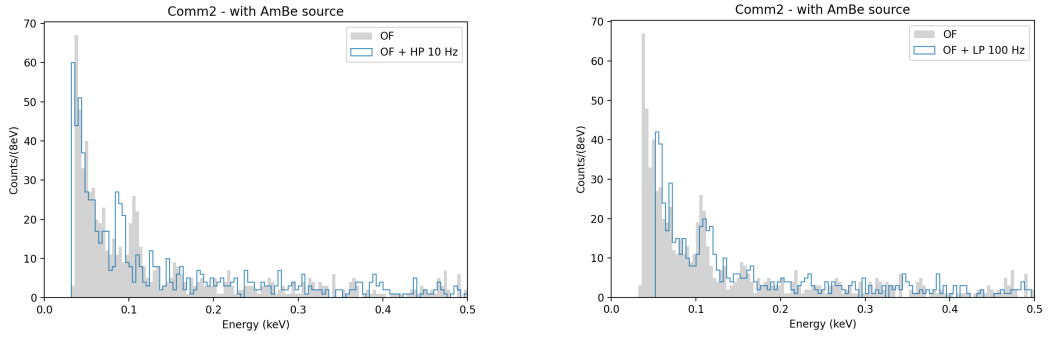

(a) HPF (b) LPF

Figure 4.11: Comparison of the low energy region of Detector Comm2 using the standard filter and HPF with $f = 10\,\mathrm{Hz}$ and LPF with modifications with the iron peak as calibration reference. In (a) the tungsten peak and energy threshold are shifted to lower energies, in (b) the peak sits at a slightly higher energy and the threshold is significantly increased.

f(Hz)	$E_{(n,\gamma)}$(eV)	$\sigma_{(n,\gamma)}$(eV)(sign.)	E_{thr}(eV)	$E_{thr,bck}$(eV)
0	106.8±1.0	3.98±0.89 (6.09)	35.83±1.80	28.03
4	100.2±1.1	3.65±0.90 (4.83)	32.03±3.66	25.85±2.34
5	97.8±1.0	3.48±0.85 (4.98)	32.35±4.27	25.35±2.96
6.7	96.2±1.0	3.74±0.83 (4.99)	32.77±4.67	24.09±3.96
10	89.8±0.9	3.62±0.68 (5.46)	33.59±6.45	23.33±6.24
1000	110.7±1.1	4.48±0.84 (6.10)	38.93±0.60	27.50±0.12
100	113.3±1.7	5.73±1.30 (4.52)	52.11±0.40	34.92±0.51
50	113.2±3.1	7.44±0.94 (3.01)	89.40±0.45	41.96±1.57
25	116.5±5.2	11.75±5.20 (2.69)	90.75±3.29	52.32±3.70

(a) Comm2

f(Hz)	$E_{(n,\gamma)}$(eV)	$\sigma_{(n,\gamma)}$(eV)(sign.)	E_{thr}(eV)	$E_{thr,bck}$(eV)
0	105.3±8.6	8.6±1.8 (3.3)	58.04±8.7	51.48
4	106.9±2.4	6.8±2.0 (3.3)	59.54±4.30	53.66±1.44
5	107.0±2.5	7.0±2.1 (3.2)	60.14±4.34	54.17±1.91
6.7	106.5±2.8	7.4±2.4 (3.0)	61.15±4.85	55.43±2.31
10	106.0±3.3	8.0±2.9 (2.7)	63.12±5.63	57.85±3.18
1000	108.4±3.9	6.1±3.3 (3.2)	57.97±4.19	51.57±0.03
100	106.5±3.2	7.6±2.5 (2.7)	61.84±5.14	50.49±1.19
33	108.3±6.2	9.3±4.4 (1.9)	62.52±5.90	52.60±2.30
25	107.5±5.6	9.8±3.8 (1.9)	63.30±6.10	53.55±3.00

(b) TUM93A

Table 4.7: Reconstructed energy of the ^{182}W recoil peak $E_{(n,\gamma)}$ and resolution $\sigma_{(n,\gamma)}$, also showing the significance of the likelihood fit and the energy threshold of the background $E_{thr,bck}$ and neutron calibration data set E_{thr}. The new data set shows a higher threshold but the effect of the applied filters follows the same trend.

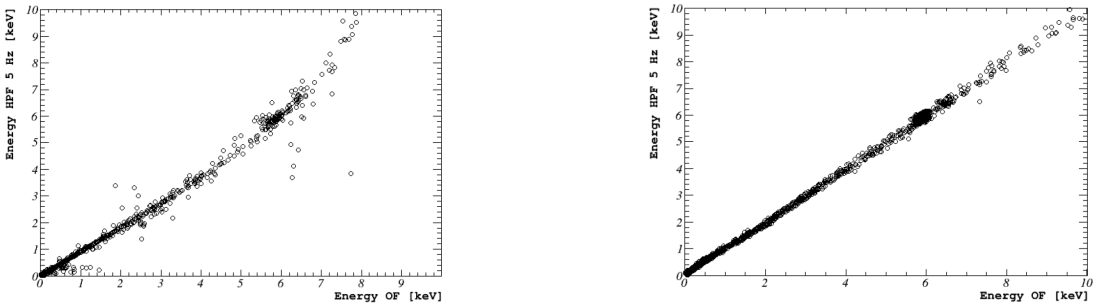

(a) Comm2 (b) TUM93A

Figure 4.12: Comparison of the TPE amplitude in Detector Comm2 (left) and TUM93A (right) using the standard filter and a HPF modification with $f_h = 5$Hz. Comm2 shows a non-linear deviation from the original energy scale.

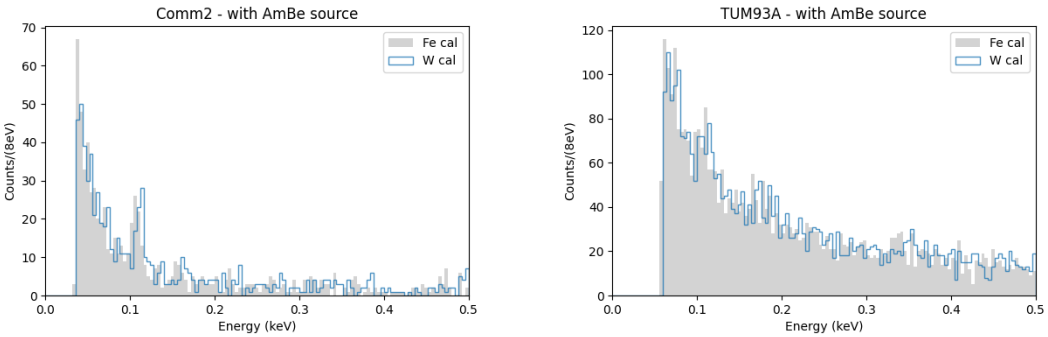

(a) Comm2 (b) TUM93A

Figure 4.13: Recoil energy spectrum calibrated using iron and tungsten calibration for both detector modules. The grey area is showing the spectrum calibrated using the iron peak, the blue line the spectrum using the tungsten peak. With the new calibration method the recoil peak and energy threshold sit at a higher energy value.

4.5.2 Tungsten Calibration

In the following the calibration of the energy spectrum was done using the ^{182}W recoil peak as a reference point instead of the ^{55}Fe escape peak to obtain a more accurate result for the low energy region with less uncertainty. The recalibrated recoil energy spectrum is shown in Figure 4.13. In the standard energy calibration the peak was reconstructed at lower energies with a deviation from the expected position of around 5 %. Using the new calibration returns a higher value for the CPE factor, shifting the recoil spectrum to higher energies and returning higher threshold and low energy resolution values, they are stated in the following section.

4.5.3 Threshold and Resolution

The energy thresholds of the data set were recalculated using the new CPE factor corresponding to the tungsten peak for each previously used filter. The resolution of the peak was determined by a likelihood fit on the new calibrated energy spectra. The obtained values are given in Table 4.8 and 4.9.
In the Comm2 module the reconstructed energy of the iron peak is no longer compatible with the energy of the decay. Applying HPF to the original OF shows at best a small improvement on the resolution of the tungsten recoil peak, that lies within the error of the original resolution and has a lower significance, but significantly worsens the resolution at higher energies. Applying a LPF with a cut-off frequency $f = 1000\,\mathrm{Hz}$ leads to a small improvement of the resolution in module TUM93A, that lies within the error of the original value. No improvement of the threshold is observed.
Using the tungsten recoil peak as a calibration reference, allows a more accurate calibration of the low energy ROI, but the additionally applied filter generally worsens the sensitivity or has no noticeable effect.

$f_{h,l}$(Hz)	E_{Fe}(keV)	σ_{Fe}(eV)	σ_W(eV)(sign.)	E_{thr}(eV)
0	6.15±0.01	139.5±10.7	3.98±0.89 (6.09)	37.35±0.33
4	6.85±0.02	270.9±24.5	3.66±0.90 (4.83)	37.48±0.44
5	6.87±0.03	323.6±31.6	4.48±0.84 (4.98)	37.47±0.43
6.7	7.36±0.04	685.7±51.1	3.73±0.83 (4.99)	38.67±0.44
10	7.55±0.04	587.6±35.9	3.77±0.73 (5.46)	37.62±0.43
1000	6.09±0.01	150.0±9.1	4.48±0.84 (6.10)	39.43±0.39
100	6.07±0.01	139.1±8.6	5.73±1.30 (4.52)	51.70±0.83
50	5.84±0.01	131.6±7.2	6.89±3.80 (3.01)	70.38±2.30
25	5.77±0.01	127.2±7.3	13.00±0.54 (2.69)	88.80±4.06

Table 4.8: The reconstructed energy E_{Fe} and resolution σ_{Fe} of the iron peak, the resolution of the tungsten peak σ_W and the energy threshold E_{thr} after the calibration with the tungsten recoil peak with energy $E_W = 112.4\,\text{eV}$ for detector Comm2.

$f_{h,l}$(Hz)	E_{Fe}(keV)	σ_{Fe}(eV)	σ_W(eV)	E_{thr}(eV)
0	6.15±0.01	105.1±6.5	6.8±1.9 (3.1)	60.50±1.55
4	6.33±0.01	130.2±8.7	7.0±2.1 (3.0)	63.76±2.11
5	6.30±0.01	132.9±10.0	7.2±2.2 (3.0)	64.24±1.58
6.7	6.24±0.01	133.5±8.8	7.7±2.5 (2.9)	64.73±1.78
10	6.17±0.01	133.0±8.8	8.2±3.0 (2.7)	66.18±2.03
1000	6.41±0.01	115.9±7.2	6.4±2.5 (3.0)	62.87±1.44
100	6.12±0.01	104.3±6.6	7.4±2.6 (2.3)	64.18±2.09
50	6.23±0.01	104.7±6.5	5.6±4.3 (1.7)	66.63±3.33
33	6.19±0.01	102.6±6.3	8.3±13.0 (1.5)	65.65±9.69
25	6.26±0.01	102.5±7.3	9.8±4.8 (1.4)	67.15±4.66

Table 4.9: The reconstructed energy E_{Fe} and resolution σ_{Fe} of the iron peak, the resolution of the tungsten peak σ_W and the energy threshold E_{thr} after the calibration with the tungsten recoil peak with energy $E_W = 112.4\,\text{eV}$ for detector TUM93A.

4.5.4 Trigger Simulation

In the following the energy threshold and resolution at the threshold were determined with the help of a trigger simulation, as shown in Section 3.7, to perform a cross-check whether the results originate in the method of determination. The simulation was performed in a range of 0–8 keV with a rate of 0.2 Pulses/s. From all simulated events, those surviving the trigger condition and not responding to a test or control pulse time stamp are considered triggered events. Since the simulated amplitude was considered to build the ratio, a coincidence cut was applied, removing all real events overlapping the simulated events. The threshold and resolution determined from this method show comparable results to the previous section, but the fits give very high errors, especially for the resolution. No improvement of the threshold is observed. The origin of the resulting change does not seem to be dependent on the determination method. The

results are presented in Table 4.10. The error shown is only the error of the fit and does not show any additional uncertainty introduced by the new energy calibration, which is negligible in comparison.

$f_{h,l}$(Hz)	$E_{W,OF}$(keV)	$\sigma_{W,OF}$(eV)	$E_{W,S}$(keV)	$\sigma_{W,S}$(eV)
0	60.50±1.55	6.8±2.5	59.54±9.50	7.56±15.23
4	63.76±2.11	7.0±2.1	55.61 ±14.37	9.72±16.71
5	64.24±1.58	7.2±2.2	56.68±15.22	11.25±20.60
6.7	64.73±1.88	7.7±2.5	59.61±15.35	11.87±21.20
10	66.18±2.03	8.2±3.0	66.09±17.68	15.85±24.44
1000	62.87±1.44	6.4±2.5	59.45±13.54	10.23±19.07
100	64.18±2.09	7.4±2.6	57.71±14.81	11.04±19.10
50	66.63±3.33	5.6±4.3	66.06±17.27	16.05±24.97
33	65.65±9.69	8.3±13.0	69.85±16.19	11.88±21.89
25	67.15±4.66	9.8±4.8	74.86±17.30	12.76±23.73

Table 4.10: The energy threshold E_F and baseline resolution $\sigma_{BL,F}$ determined with the OF method and the threshold E_S and resolution $\sigma_{BL,S}$ obtained with the simulation. The energy spectrum was calibrated with the neutron source. The first two rows show the results obtained with the original OF. The following two using an additional HPF with f_h.

4.6 Conclusion

Applying additional band-pass filters to the OF shows an effect on the analysis outcome for most detectors using the iron escape peak as a calibration reference point. The usage of additional LPFs, that lower the power of the filter kernel at the higher end of the frequency spectrum, leads to an improvement on the resolution of the calibration peak. Additional HPF, that lower the power of the filter kernel at the lower end of the frequency spectrum, at a first glance seem to improve the values of parameters in the low energy region. The parameters include the baseline resolution and the energy threshold. The added HPFs at the same time worsen the resolution of the iron peak at a higher energy, giving additional uncertainty to the calibration. When comparing the calibrated energy spectra of the original OF to the modified filter, a clear non-linearity can be seen. This implies an inaccurate reconstruction of the energy, leading to non conclusive results on the real energy of the parameters in the low energy region. Following the definition of the OF, this confirms a seen energy dependence of the pulse shape, whose influence is enhanced through the modified filter or additionally implies non-stationary noise.
To obtain a more meaningful result the energy of the modules that consist of a calcium tungstate crystal was calibrated using a tungsten recoil peak. The peak lies within the linear region of the new calibration at around 112 eV. In the analysis a small improvement of the tungsten peak at low energies can be seen, but the fit gives a high uncertainty. It can be seen that cutting on lower frequencies has no significant effect on the low energy region in both considered detector modules, while cutting on higher frequencies worsens the low energy parameters.
The low energy region of one of the modules, TUM93A, was almost unaffected by the additional filters in both data sets and both calibrations. The modules differ in material, holding scheme and installation of scintillating foil within the module, but with the limited amount of data and detectors in the current data taking run no conclusions can be drawn on the origin of the differing results. The results for all other modules were dominated by the inaccurate energy calibration shifting the calculated threshold and baseline resolution values to false, low numbers. The Comm2 module showed the highest inaccuracy. Both named modules contain calcium tungstate detector crystals and are the only modules considered for the complete study, where they are showing results with the greatest difference. The other modules of different materials follow roughly the behaviour of Comm2, hinting towards a material independence of the results.
With no filter a significant improvement of the considered parameters, resolution and threshold, could be achieved in the low energy region. But there is room for further exploration of the issue. It can be attempted to correct the energy spectrum for higher energies. Only a very basic type of BPF was explored, different filter types can potentially return the desired result by cutting on the frequencies in different manners. In this study different modules showed to be affected differently, but no clear trend or origin of the differences could be found or investigated due to the limited data and available detector modules. To gain more information the study can be performed on more detector modules and different data sets.

Chapter 5

Low Energy Analysis

In current DM search low threshold experiments observe a rise of unknown events at the very low energies above threshold. For a more detailed discussion of this phenomenon see Section 2.5.1. In the current status of the experiment the LEE is the limiting factor in sensitivity for low mass DM search. Exploring the characteristics and origin is essential to understand and remove its influence on current data or take data without its occurrence in the future. In the most recent data taking campaign of CRESST-III a time dependence and a dependence on temperature increases was observed and studied [56]. This chapter describes the raw data analysis of the standard DM search data and the limit calculation for a calcium tungstate module of the recent data taking run in Section 5.1. The raw data analysis of the data taken during time and temperature dependency tests, as well as a short analysis of the excess' time behaviour is presented in Section 5.2. In the final Section 5.3 the raw data and negative high level analysis is shown for a data set taken with a lower excess rate. The module analysed in the chapter is the TUM93A detector module. Its setup is described in Section 2.3. The crystal used as a target was grown at Technische Universität München (TUM) with specially purified $CaWO_4$ powder and an optimized growing technique, aiming for a reduction of radio impurity and intrinsic stress [4].

5.1 Background Data Dark Matter Analysis

This section describes the raw data analysis and spin-independent exclusion limit calculation of the TUM93A background data set used for DM search. The analysis was trained on a small data set containing $0.66\,\mathrm{kg}\cdot\mathrm{d}$ of data and later applied to the remaining full data set of $3.61\,\mathrm{kg}\cdot\mathrm{d}$.

Data Selection

The data files were selected to exclude files too short in length and files that were affected by technical disturbances. The used file list can be found in Table A.1. A stability cut

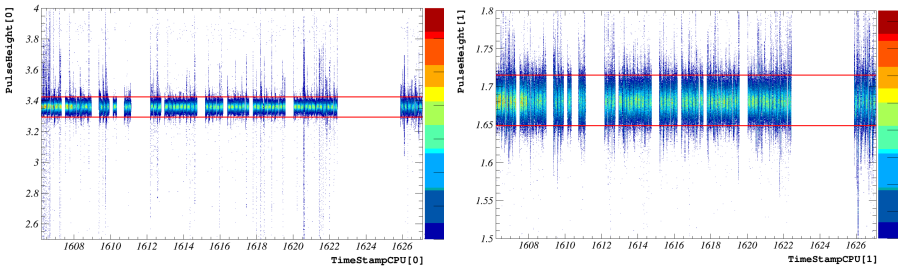

Figure 5.1: Recorded amplitude of the control pulses over time for the phonon channel (left) and light channel (right), the red lines indicate the range within the the pulses are considered stable.

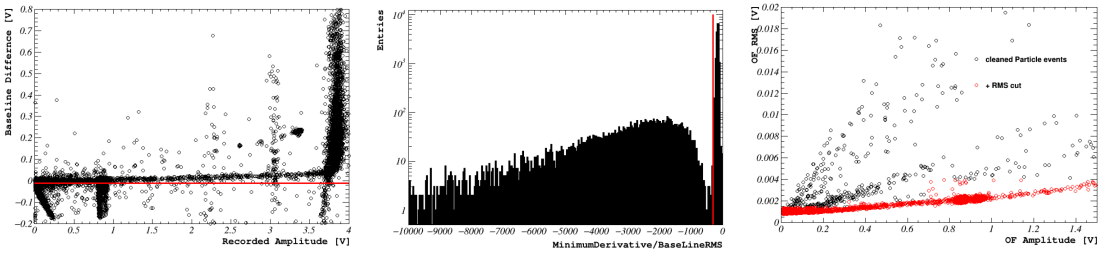

(a) Baseline Difference (b) Voltage Spikes (c) OF r.m.s. (Pulse shape)

Figure 5.2: Data Quality Cuts applied to the particle events of the TUM93A phonon channel. The first two plots show all triggered particle events and the red line marks the applied cut. In (a) all events above the red line were kept, in (b) all events to the right of the line. The last plot shows all particle events surviving the previous two cuts in the linear region of the detector in black and all particle events surviving an additional cut to the r.m.s. of the applied OF in red.

was applied to exclude unstable time periods of the detector with the help of the injected heater control pulses. The amplitude of the pulses over time and the considered stable region, marked with red lines, are shown in Figure 5.1. The stable region is set to be 3σ above and below the mean. Additionally data quality cuts were applied following the criteria in Section 3.1, aiming to exclude non particle events and disturbances while not removing "good" particle events. The cuts applied to the particle events of the phonon channel are shown in Figure 5.2. A rate cut removing time periods of 600 s with a significantly higher rate than average was applied. A cut removing all events with an absolute light yield higher than seven was applied, removing events clearly outside of the acceptance region. The data cuts are based on the phonon response channel leading to a less clean characterization of the light channel mostly observable in the noise spectrum.

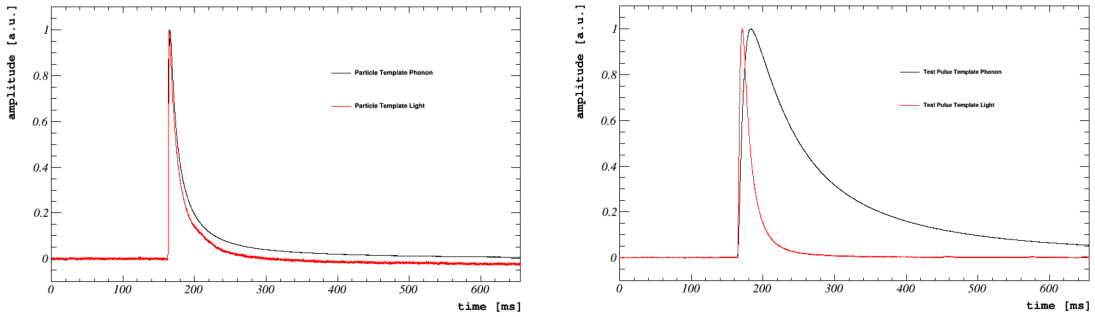

(a) Particle events (b) Test pulse events

Figure 5.3: The SEV templates for particle pulses are in the left plot, the test pulse equivalent in the right one. The black curve shows the phonon channel, the red curve the light channel.

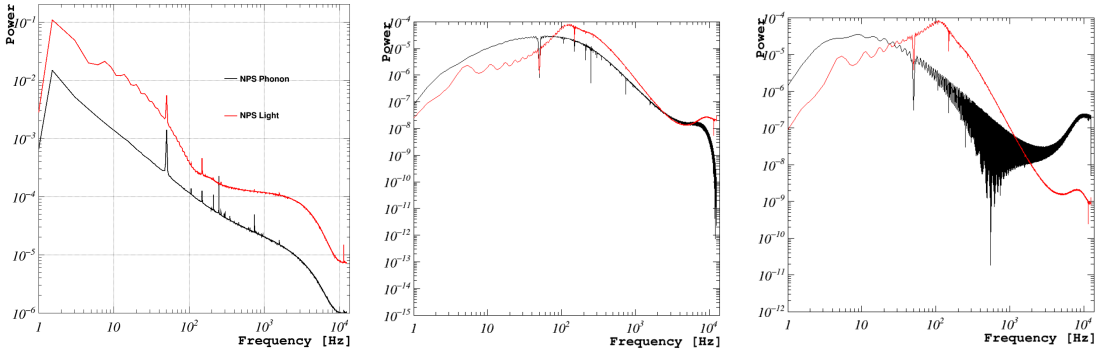

(a) Noise power spectrum (b) Particle optimum filter (c) Test pulse optimum filter

Figure 5.4: The frequency response of the NPS and OF kernel for particle and test pulses events. The phonon channel response is shown in black, the light channel in red.

Pulse Shape, Noise Spectrum and Optimum Filter

Figure 5.3 shows the used SEV templates, Figure 5.4 the NPS and OF for both channels. The light channel pulses show a fast rise for both particle and heater pulses, while the particle pulses of the phonon channel have a similar rise time, the heater pulses of this channel are rising and decaying much slower. The light channel has a faster decay time for both event types. The noise background of the light channel sits at a higher level but shows similar features, e.g. noise spikes, to the phonon channel. The OF of the light channel reflects the high level of noise in the low frequency range. The filter for the test pulses of the phonon channel shows disturbances in a frequency range between 100 Hz and 1300 Hz that are not present in the noise spectrum and must correspond to noise frequencies in the event template or be artificially created while building the filter.

Energy Calibration

The TPR object was built using the OF amplitude and a spline interpolation. The truncation limit of the phonon channel was determined to be around 1 V. Both iron lines at around 0.9 V are within the linear regime of the detector allowing a reliable energy reconstruction with the OF up to 8 keV. Data quality cuts following the selection criteria were applied to the test pulse list. For injected time stamps of the test pulses the spline amplitude of the TPR object is evaluated to obtain the TPE amplitude. The resulting amplitude is plotted for all particle pulses, that survived the data quality cuts, excluding the light yield cut. The two iron peaks at 5.89 keV and 6.49 keV are used for calibrating the energy spectrum returning a CPE factor of 3.11. The same was done for the light channel, returning a CPE factor of 11.54. The threshold and baseline resolution parameters are calibrated using the CPE factor and the reconstructed position of the lowest test pulse compared to its injected power. The so-call conversion factor was determined to be 2.13 for the phonon channel and 4.82 for the light channel. This factor is used to factor in the TPR when calibrating low energy parameters.

Baseline Resolution and Energy Threshold

To determine the baseline resolution small pulses with an amplitude of 0.2 V for the phonon channel and 0.125 V for the light channel were simulated onto empty baselines and the maximum of the OF amplitude was determined. The obtained resolution is 1.33 mV for the Phonon and 2.51 mV for the light channel, this translates to energies of 8.80 eV for the phonon channel and equivalent energy of 136.09 $\mathrm{eV_{ee}}$ for the light response. The threshold of the phonon channel is determined from filtered baselines, returning a value of 8.32 mV, which corresponds to an energy of 55.20 eV.

Trigger and Survival Probability

A simulation was performed to determine the trigger and survival probability of the analysis. In the simulation pulses of different, random amplitudes within the energy range 0–8 eV and a rate of 0.2 $\mathrm{s^{-1}}$ are simulated on the continuous data stream. The fit to the trigger probability returned a threshold value of 55.43 eV, giving a comparable result to the earlier used determination method. Both probabilities are shown in Figure 5.5. For uniformity, both probabilities are shown as a comparison of reconstructed amplitude in the surviving spectrum to injected amplitude in all simulated events. This causes a false visual rise in the trigger probability due to the overlaying of real and simulated events.

5.1.1 Recoil Spectrum and Dark Matter Search

The resulting efficiency corrected energy spectrum obtained using the OF for amplitude reconstruction is shown in Figure 5.6. The spectrum is corrected by multiplying it with the inverse survival probability. The recoil spectrum features the ^{55}Fe lines at 5.89 keV and 6.49 keV and an exponential-like rise of events starting from 200 eV towards the

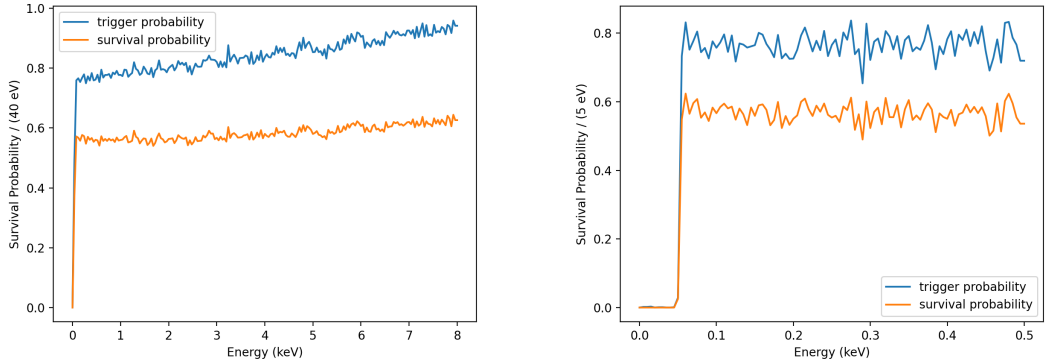

(a) Full simulated range (b) Low energy region

Figure 5.5: The fraction of all simulated particle events surviving the trigger criteria (blue) and data quality cut (orange) in the low energy region gives the trigger and survival probability.

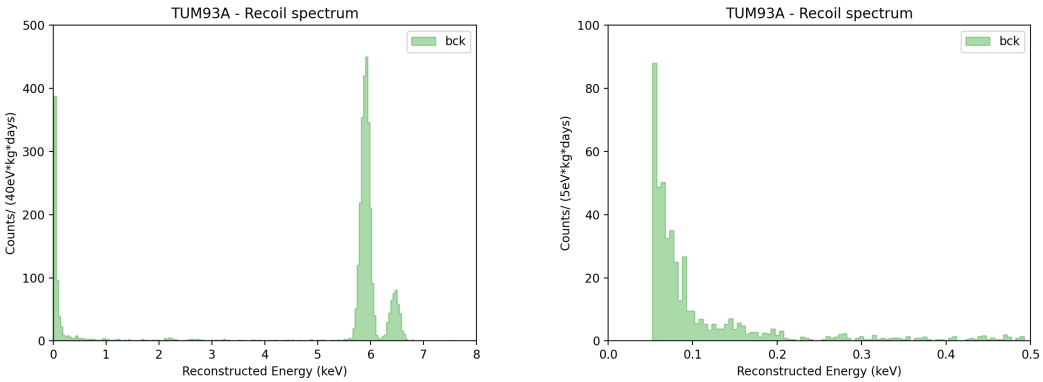

(a) Full linear energy spectrum (b) Low energy region

Figure 5.6: Efficiency and exposure corrected energy spectrum for the full calibrated energy range on the left and a zoom-in on the low energy region up to 500 eV on the right. The full energy spectrum features both iron lines visually resolved. The low energy ROI shows the LEE.

threshold are visible in addition to a low constant background. The spectrum is limited to 8 keV since energies above cannot be reconstructed reliably with the OF amplitude. A band fit was performed and the limit calculated with Yellin's optimal interval method using the limitless software package developed for [93]. Details on the performed band fit, used dark matter model and limit calculation model can be found in Section 3.8.1. The band fit was performed on the neutron calibration data to define the acceptance region more accurately due to higher statistics on nuclear recoil events. The files used

for the creation of the spectrum are shown in A.1, the data was selected, cleaned and analysed following the standard analysis chain. The result of the band fit for both data sets are shown in Figure 5.7. The plots include the fitted light yield bands (top) and fitted recoil spectra (bottom) for the blind background data (left) and neutron calibration data (right). The resulting exclusion limit is shown in Figure 5.8 in reference to the current best limit in the mass region, given by Detector A from a previous CRESST-III run [57]. The limit lies above the old limit for all considered masses, not excluding new parameter space. It follows a similar shape, but the higher threshold compared to 30 eV of Detector A and the lower exposure lead to a worsening of the limit at the lower and upper end. The complete bck data analysis was previously done for [4]; the results are comparable.

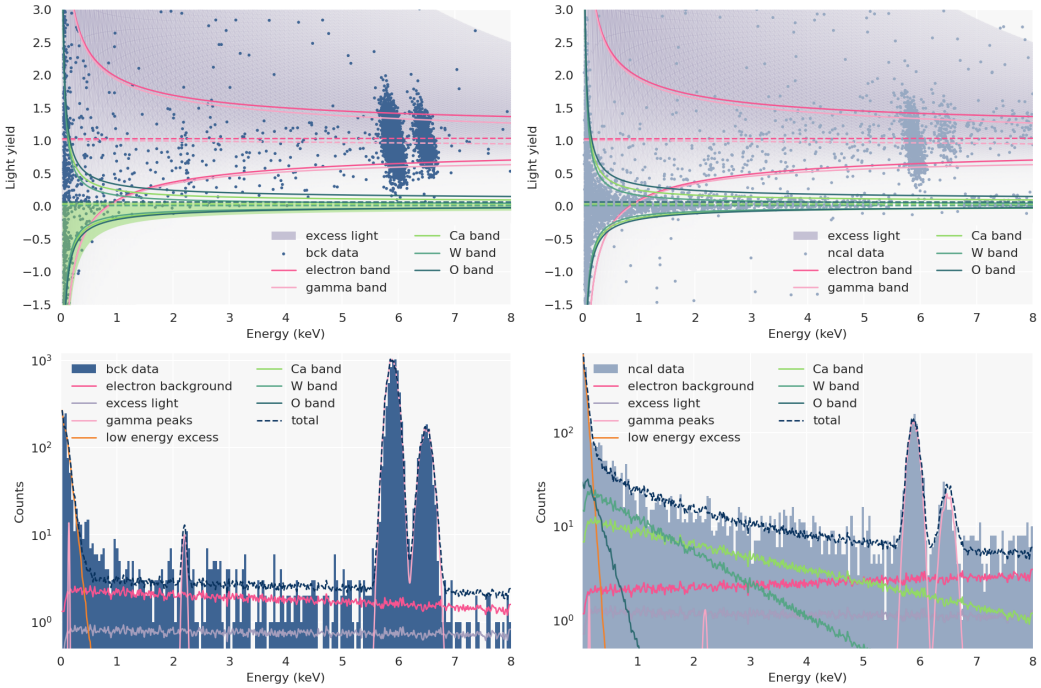

Figure 5.7: Result of the band fit applied to the background (left) and neutron calibration data (right). The top plots show the bands in the light yield, the bottom plots the fitted recoil spectrum. The data is shown in blue, light blue for the neutron calibration data, the pink curves show the electron and gamma band, the green curves represent the individual nuclear recoil bands for the different nuclei in the crystal. The LEE is given by the orange curve and the region of excess light event is shaded in grey.

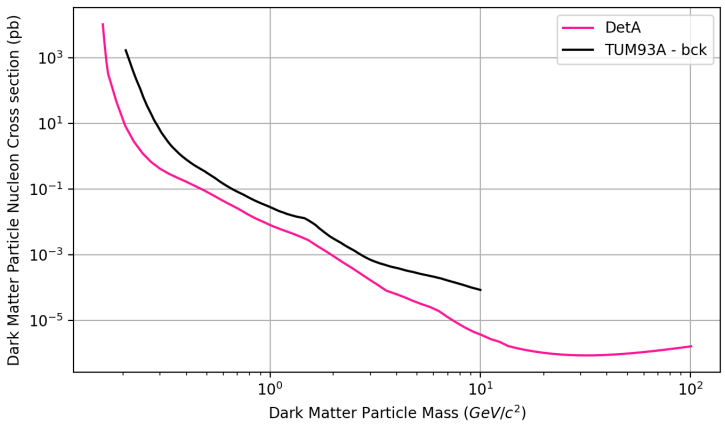

Figure 5.8: DM exclusion limit on spin-independent interactions for the TUM93A background data set in the DM particle mass and DM particle nucleon cross section calculated in this work (black) and Detector A (pink) [57].

5.2 LEE Time Dependence

In detectors of previous CRESST data taking runs a time decay of the LEE events could be observed. To monitor the behaviour of the events in this detector, a range, starting close to the threshold but with mostly flat survival probability up to the end of the prominent exponential-like rise of events, was chosen to be from 60 to 120 eV. In the first part of the section the decay of the bck data set is shown, then the time dependence after temperature increases of the cryostat is shown and shortly analysed.

Background Data

Figure 5.9 shows the LEE time dependence of the bck data set. Each data point represents the counts between 60 and 120 eV in each data file with length of 40 to 60 h scaled with exposure and efficiency. The data was fitted with an exponential function plus a constant part to gain knowledge on the decay time. The fitted decay time is around 85 days with remaining constant background rate of 2.5 d^{-1}. Afterwards the same fit was performed including a short data set taken after the neutron calibration (postcal) and a second blind data set taken roughly 450 to 500 days after the bck data, in the following referred to as AWU data, to monitor the long term behaviour of the decay. It has to be noted that the effect of tests performed in between the two data sets (see Section 5.2.1) on this decay of the excess is not completely known and understood, changes of the decay rate are possible. The fit results are shown in Table 5.1. The fit returns a slightly lower background constant at around one count per day and a longer decay time of 160 days. The fit performs better and returns values with lower uncertainty. A comparison of the average pulse shape of the events in the low energy region and for

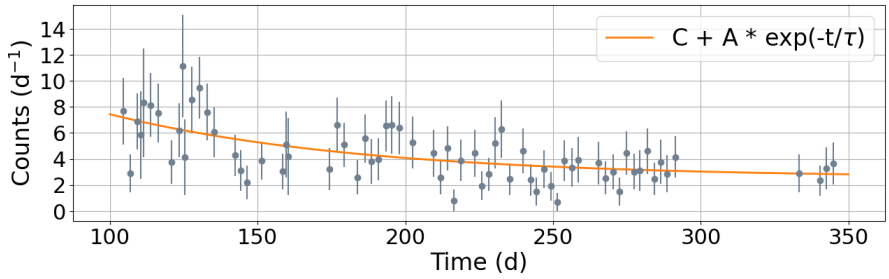

(a) bck

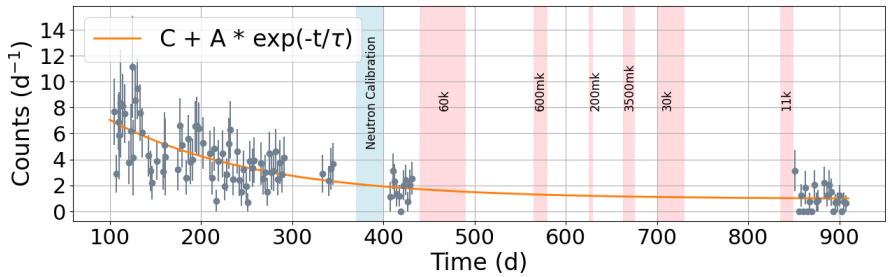

(b) Extended data set

Figure 5.9: The low energy particle events with energies from 60 to 120 eV plotted over time, including the best exponential fit for the bck and an extended data set covering a longer time period. The marked areas indicate the separation of the data sets, not the exact time of the warm-up or start of data taking.

	Constant C	Amplitude A	Decay time τ (d)
bck	2.56±1.01	15.66±9.66	85.80±49.93
extended	0.95±0.33	11.27±1.68	162.79±29.90

Table 5.1: Fit results of the LEE counts over time.

higher energies in Figure 5.10, shows that the LEE events follow a particle-like pulse shape.

5.2.1 Warm-up Tests

After an accidental warm-up in the EDELWEISS experiment, they observed an increase of the LEE rate [94]. The CRESST collaboration decided to test this effect in their own experiment by performing controlled warm-up tests. Up until February 2024 six warm-up cycles were executed. The following temperatures were reached during the warm-up test (in time order): 60 K, 600 mK (uncontrolled), 200 mK, 3.5 K, 30 K, 11 K and 130 K. The temperature value refers to the rough maximum temperature reached in the lead shielding during the warm-up. In the first warm-up it was planned to reach

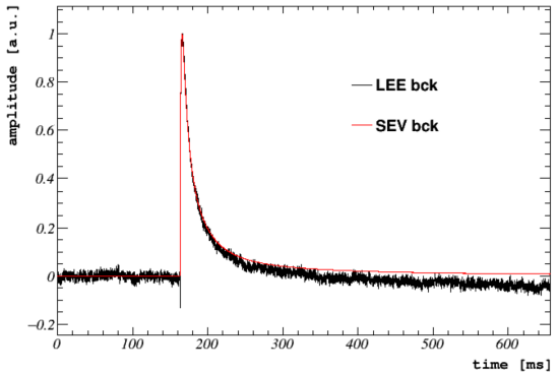

Figure 5.10: The average pulse shape of events from 60 to 120 eV is shown in black, the standard pulse shape taken from the avergae iron pulse is shown in red.

a temperature of 30 K, but due to the uncontrollability of the cryostat a temperature of around 60 K was reached. The data taking was interrupted by a power outage caused by a snow storm in the close geographical area of the experiment, leading to a warm-up of the lead to around 600 mK. After seeing an increase of the rate at 60 K, it was decided to perform warm-ups to lower temperatures to monitor the temperature dependence of the event rate. The temperatures reached during these warm-ups were around 200 mK and 3500 mK, but no noticeable rate increase could be observed. Lead reaches it superconducting state at a critical temperature of 7.2 K [95]. The following warm-up aimed to reach a temperature above this critical temperature at around 10 K, but reached 30 K. After observing an increased rate a second warm-up was executed, aiming to a lower temperature reaching closer to the desired value at around 11 K. No clear rate increase could be observed afterwards, giving a high indication that the effect is not related to the chancing conducting state of the lead shielding. As a final test the warm-up up to 60 K should be repeated but the high temperature should be maintained for a longer time, the initial warm-up reached around 90 K, during the cool down a plugged condenser had to be cleaned leading to a warm-up to around 130 K. The temperature curve of the warm-up is shown in Figure 5.11. During the warm-up test, the cryostat was circulated with liquid nitrogen at 77.3 K, giving the theoretical maximum of the warm-up temperature. Evidently, higher temperatures were recorded, suggesting an inaccurate temperature reading. For this warm-up it was paid close attention on starting the data taking as soon after reaching base temperature as possible to catch any fast decaying components. In the previous tests the data taking was started several days after reaching the operating temperature and the time interval not monitored. The data of the 11 K warm-up was taken as a blind data set to perform a DM analysis with reduced LEE. The other data sets were not taken blind to allow quick feedback of the excess behaviour. The complete analysis chain was done for each warm-up data set individually, accounting for differences in detector performance caused by the warming up and cooling down of the modules. The properties for each data set are stated in Table 5.2, including exposure,

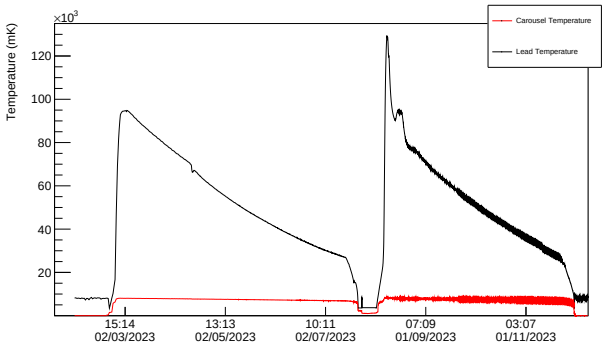

Figure 5.11: Temperature progress of the lead shielding and detector carousel during the 130 K warm-up test. The initial warm-up reached around 90 K, after complication the set-up warmed up until 130 K before the final cool down, taken from [96].

	bck	60 K	600 mK	200 mK	3500 mK	30 K	11 K1	11 K2	130 K
E_{thr} (eV)	55.20	51.70	52.07	51.83	54.72	51.33	48.27	49.70	44.65
σ (eV)	8.80	7.19	7.23	7.16	7.50	7.19	7.42	7.58	6.75
ϵ (kg·d)	3.61	1.54	0.93	0.67	0.26	1.89	0.53	0.59	1.21
lead (K)	293	-	-	-	-	30	11.9	-	129

Table 5.2: Detector performance of each data set, including the background data and all warm-up test in chronological order, is shown by the energy threshold E_{thr}, the baseline resolution σ and the exposure ϵ. The maximum temperature reached during the warm-up in the lead shielding is given if it is known precisely [96].

threshold and resolution. The table contains the maximum temperature values reached in the lead shielding, if they are known from recorded monitoring curves. The temperature before the background data was set to be room temperature. In the following the warm-up test will be referred to by the estimated maximum temperature reached in the lead shielding as they are named in Table 5.2. During the data taking of the 11 K warm-up data, the operating point of the detector changed and two different data sets, before (11 K1) and after (11 K2) the change, were considered. The used data selection cuts, templates, NPS and OFs for all warm-up tests and the post-calibration data are shown in Appendix A.2.3, as well as the survival probability and energy spectra. For more information on the 11 K warm-up see Section 5.3.

Time and Temperature Dependence

The LEE counts seen in the TUM93A detector during the bck data taking and warm-up test are shown in Figure 5.12. Each data point contains the counts of a data file scaled for its length and the simulated survival probability of the data quality cuts. A definite increase of the low energy excess can be observed after the 60 K, 30 K and 130 K warm-up, which then decays with a shorter decay time than the decay observed in the bck data set. No increase above the uncertainty can be seen for the warm-ups to 200 mK,

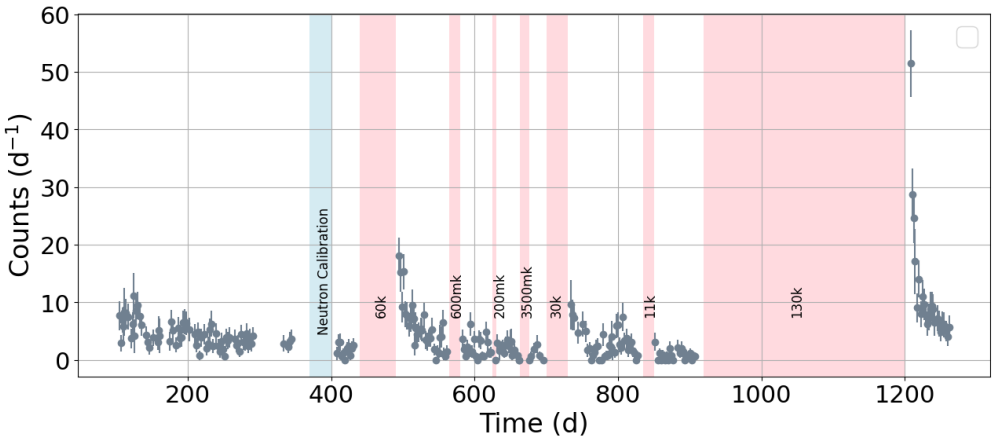

Figure 5.12: The grey dots represent the data counts in an energy region between 60 and 120 eV in each individual file corrected for the average survival probability and length of the file. The x-axis shows the time since the beginning of the first data file taken in the current run about two weeks after the initial cool down of the cryostat reaching operating temperature. The data includes the bck data, data taken after the neutron calibration and all warm-up test until February 2024. The marked areas indicate the separation of the data sets, not the exact time of the warm-up or start of data taking.

600 mK and 3500 mK. A potential small increase of the excess rate can be seen in the 11 K warm-up. The neutron calibration, that was performed in between the bck and postcal data sets, showed no noticeable effect on the LEE rate. The data sets, that saw a rise in excess events were fitted with two exponential functions to account for the slow decay with the decay constant τ_s and amplitude A seen in the bck data set and the new faster decay in the warm-up data with the decay constant τ_f and amplitude B.

$$F(t) = C + A \cdot exp(-t/\tau_s) + B \cdot exp(-t/\tau_f) \tag{5.1}$$

First the fit was done with free parameters, in a second attempt the slow decay constant was fixed to the value of the bck data and extended data set. For the 11 K data set no satisfying fit could be achieved for the free parameter fit and the result states simply the average. This average value matches the constant value obtained from the fit of the slow decay above. The 60 K data set includes data taken after the 200 mK, 600 mK and 3500 mK warm-ups. The results of the free fit are shown in Figure 5.13 and Table 5.3, the results for the fit with fixed slow decay time are in Table 5.4. In the plot zero in the x-axis marks the begin of the data taking of the considered data set. The free fit returns values around 200 days for the slow decay time but with a high uncertainty, the fast decay component is around 10 days. Fixing the slow decay returns similar values for the fast decay in the 60 K and 30 K data and no fast decay in the 11 K data. The constant is roughly 1 d^{-1} for all data sets and fits. The free fit parameters are in better agreement with the values obtained from the extended data set. The results of the 130 K warm-up deviate from the others by returning faster decay times for all time parameters.

It reaches a background constant of zero counts per day but with high uncertainty. The differences can arise from the data taking starting earlier after reaching the working temperature of the cryostat than previous warm-ups, but also can originate from the long duration and different progress of the cool down. Due to the fact that the data set is taken late after the original cool down the overall background level from e.g. the iron source could be reduced or in the previous data sets the constant was not determined accurately due to lack of statistics. A precise comparison of the slow decay component or the background constant including the 130 K data cannot be made on account of the short measurement time caused by a technical failure of the cryostat.

	Constant C	Decay time τ_s(d)	Decay time τ_f (d)
60 K	0.00±6.48	155.88±492.16	11.52±3.94
30 K	2.30±1.48	49.38±0.00	10.55±10.48
11 K	0.87±0.18	-	-
130 K	0.00±24.91	62.66±218.76	3.17±0.58

Table 5.3: Fit results of the LEE counts over time with a constant and exponential function.

	Constant C	Decay time τ_f (d)
60 K	0.87±2.12	10.55±4.24
30 K	2.30±2.48	10.54±9.32
11 K	0.86±0.94	-
130 K	0.00±49.93	3.40±0.61

	Constant C	Decay time τ_f (d)
60 K	0.00±7.33	11.82±4.02
30 K	2.30±4.68	10.55±8.72
11 K	0.87±1.75	-
130 K	0.00±202.57	3.71±0.68

Table 5.4: Fit results of the LEE counts over time with a constant and exponential function with fixed slow decay constant to the extended data set result of $\tau_s = 86$ d (left) and $\tau_s = 165$ d (right).

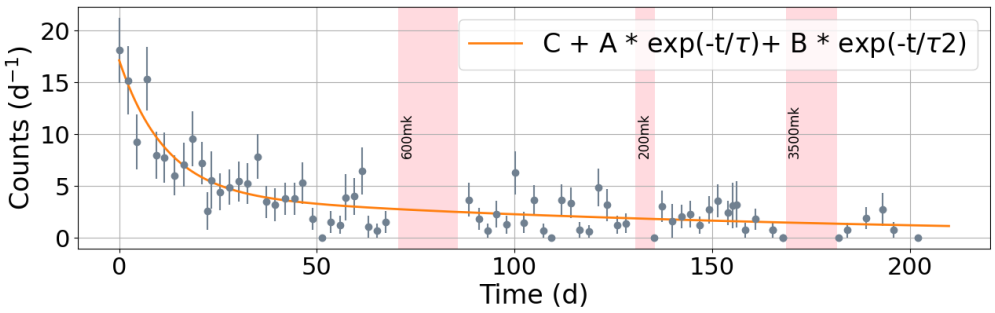

(a) 60 K

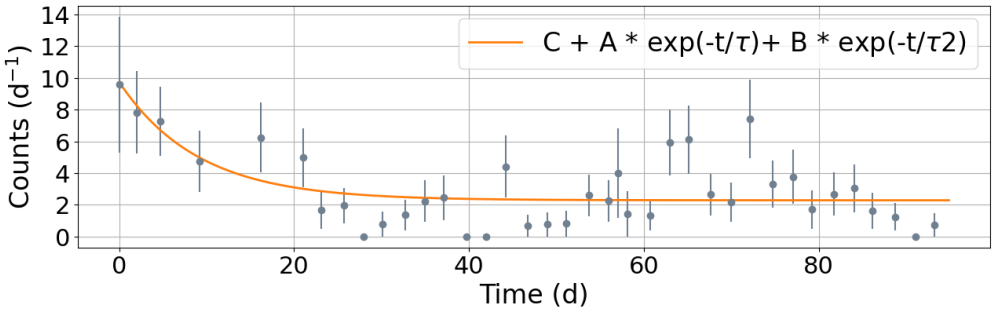

(b) 30 K

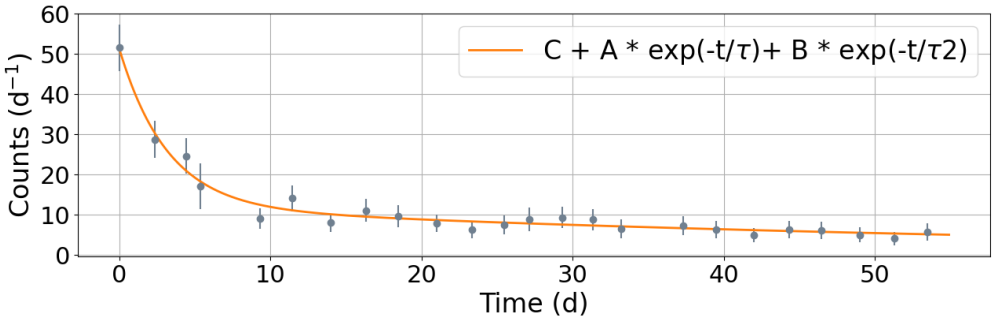

(c) 130 K

Figure 5.13: The grey dots represent the data counts in an energy region between 60 and 120 eV in each individual file corrected for the average survival probability and length of the file. The x-axis shows the time since the beginning of the individual data set. The data sets shown are the (a) 60 K, (b) 30 K and (c) 130 K AWU data. The marked areas indicate the separation of the data sets, not the exact time of the warm-up or start of data taking. The orange curve shows the best free fit using a constant and two exponential functions.

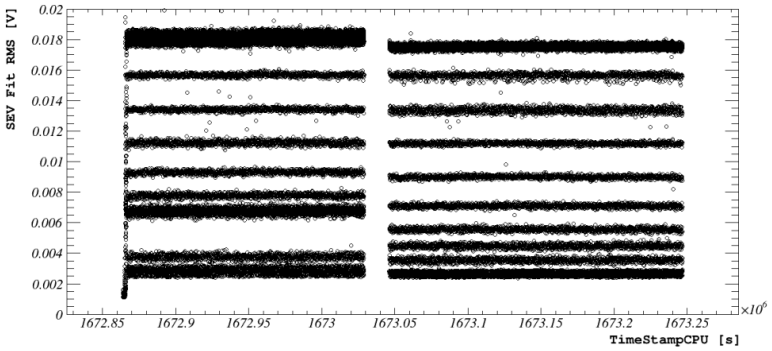

Figure 5.14: r.m.s. of the SEV fit performed on the injected heater test pulses plotted over time for the file before and after the shift of the operating point.

5.3 After Warm-up Data Dark Matter Analysis

Following the assumption that the limiting factor for DM search and detection sensitivity in CRESST is currently the unexplained exponential rise of events towards the threshold in the low energy region and the observation, that the LEE rate decays over time, it was decided to take a second blind data set about 850 days after the initial cool down of the cryostat, directly following the warm-up of the detector setup to 11 K.

Data Sets

No significant rise in events was observed after the 11 K warm-up test, giving a data set with a minimal excess rate of less than one count per day below 120 eV. Due to complications a shift of the detectors operation point occurred within the middle of the blind data taking. The shift is clearly visible in the r.m.s. of the SEV fit, that is used to monitor the detector. The r.m.s. over time for the files before and after the shift is shown in Figure 5.14. To account for the shift within the data analysis the data set was split in to two smaller sets. The first two files of each were used as the training set, the exact file numbers can be found in Appendix A.2, alongside the data quality cuts, the resulting exposure is $0.53\,\mathrm{kg}\cdot\mathrm{d}$ for the first set (11 K1) and $0.59\,\mathrm{kg}\cdot\mathrm{d}$ for the later set (11 K2). The training set of the first AWU set was triggered with the OF created from the bck data set using a trigger threshold of 8 mV. The blind data set was triggered at a threshold of 7.1 mV using the OF built from the training set. The data was processed using the same OF and data quality cuts trained on the training set. A small change in the pulse shape can be observed. The base power level is reduced by an order of magnitude for frequencies below ca. 50 Hz and roughly a factor of 5 for higher frequencies. At frequencies from 100 to 1000 Hz multiple noise spikes can be observed that were not present in the earlier data set. The energy threshold and baseline resolution were determined the same way as in the bck data. The second blind set was triggered at a threshold of 7 mV and processed the same way as the first set. A comparison of the resulting templates is shown in Figure 5.15. The results for

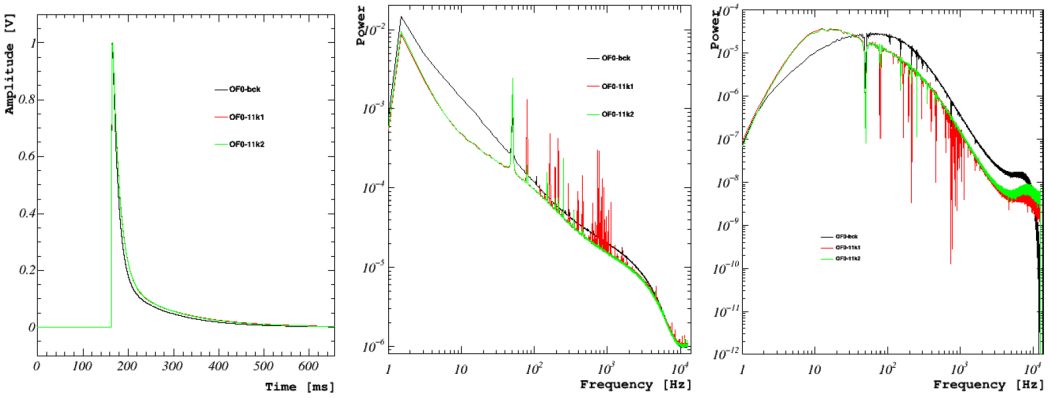

(a) Particle Events

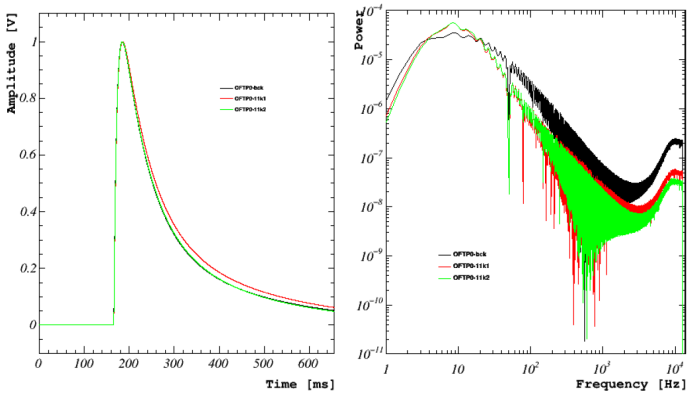

(b) Test Pulse Events

Figure 5.15: Templates of the AWU data sets for (a) particle and (b) test pulse events. The bck data set is shown for comparison in black, 11 K1 is given in red and 11 K2 in green. The left plot shows the SEV template, the middle plot shows the NPS and the right plot shows OF kernel.

	11 K1		11 K2		bck	
Threshold	7.05 mV	48.27 eV	7.07 mV	49.07 eV	8.32 mV	55.20 eV
Resolution	1.08 mV	7.42 eV	1.08 mV	7.58 eV	1.33 mV	8.80 eV

Table 5.5: Threshold and resolution in the AWU data sets and bck data

threshold and resolution can be found in Table 5.5. The value for both parameters is lower in the new data set compared to the background data, in recorded voltage as well as calibrated energy. The detectors sensitivity increased by around 15 %. The second data set shows slightly higher values in calibrated energy but the difference lies within the uncertainty of the calibration method, the shifting operating point does not affect the detector's performance. A simulation to determine the trigger and survival

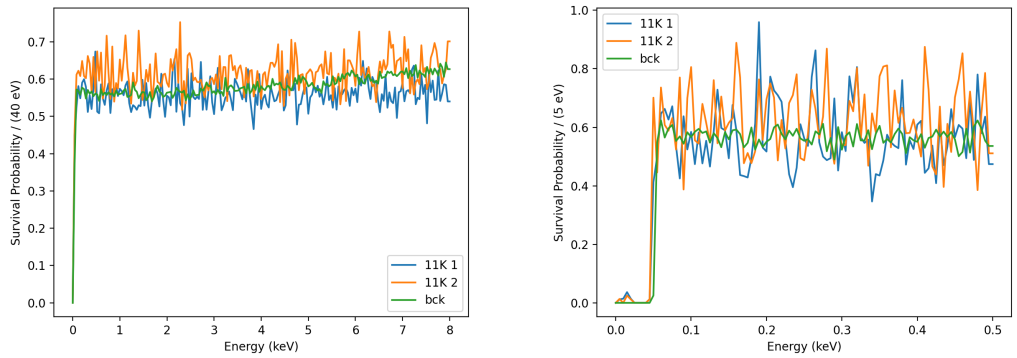

(a) Full simulated range

(b) Low energy region

Figure 5.16: The fraction of simulated particles surviving the trigger condition and all applied data quality tests for the bck (green), 11 K1 (blue), 11 K2 (orange) data. The flat part of survival probability is at the same level in all three data sets, but the 11 K2 shows high energy dependent fluctuations.

probability was performed for both data sets, the survival probability is shown in Figure 5.16, including a comparison to the bck data. In all three cases the constant level of the survival probability lies above 60 %. The probability in the AWU data shows higher fluctuations due to lower statistics. A comparison of the resulting energy spectra for both AWU data sets can be seen in Figure 5.17, the spectra are corrected for survival probability and exposure. The second part of the AWU data set showed a rise in the count rate of LEE events, that is noticeable but lies within the general uncertainty of the count rate. The rise in events starts occurring days after the change and cannot be directly related. In both data sets the LEE is now limited to an energy range from threshold to around 80 eV. The time dependence of the LEE rate between 50 and 120 eV can be seen in Figure 5.18. Each data point marks the counts in a recorded file and is corrected for the file duration and average survival probability. The extended energy range compared to the one considered in the previous section shows no rise in event rate directly after the warm-up test.

Combined Exclusion Limit

To obtain a DM exclusion limit for the complete data set, exploiting the maximum exposure of the data taking period, the two blind data sets were combined. Figure 5.19 shows the energy spectrum of the full blind data set compared to the background data scaled for exposure and cut efficiency. As expected the iron calibration shows a lower count rate in the later data set. The set was taken around 400 days after the end of the first set, reaching half of the decay time of the iron isotope at around 1000 days [97]. The overall background count in the later data set is also reduced. The LEE count rate is significantly reduced in the previously considered range, but the lower

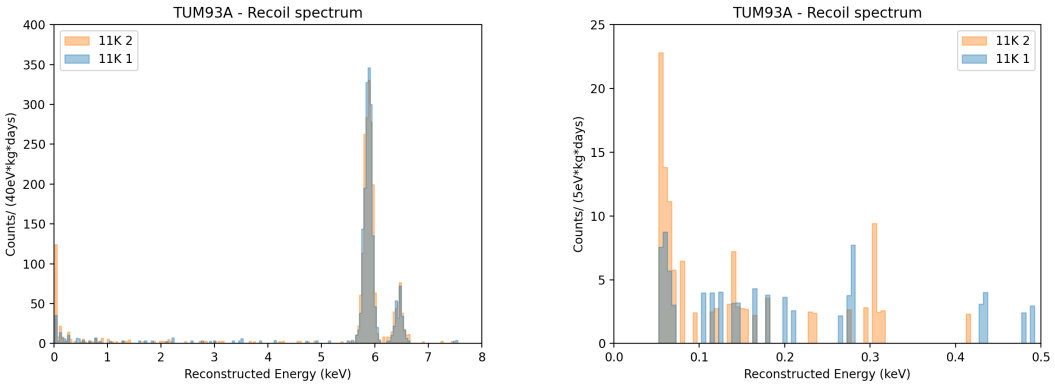

(a) Full linear energy range

(b) Low energy region

Figure 5.17: Efficiency and exposure corrected energy spectrum of the AWU data (11 K1 in blue, 11 K2 in orange) for the full calibrated energy range on the left and a zoom-in on the low energy region up to 500 eV on the right. The full energy spectrum features both iron lines visually resolved. The later set shows a much higher LEE.

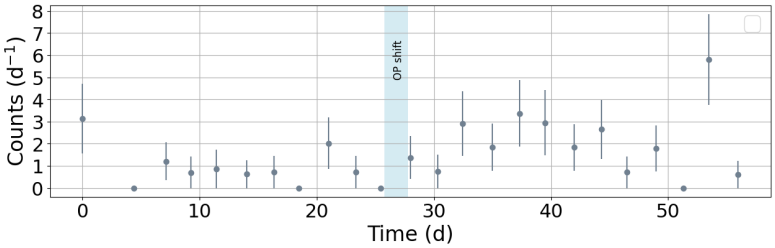

Figure 5.18: LEE count rate between 50 and 120 eV. The time frame in which the shift of the operating point (OP shift) happened is shaded light blue.

threshold in the AWU set introduces new counts following the rising behaviour of the excess towards threshold. The new limits were calculated using Yellin's optimal interval method following the same procedure for the standard bck data. The limits for the complete and individual data sets are shown in Figure 5.20. The limit of the bck data set and the current best published limit in the mass range of Detector A are shown for reference. In comparison to the limit of the background data the new DM exclusion limit reaches lower parameter space for masses between 0.23 and 6 $\mathrm{GeV/c^2}$, between the masses of around 0.4–2 $\mathrm{GeV/c^2}$ the improvement is close to an order of magnitude. Lower interaction cross section can be reached despite the exposure of the new data set being less than one third of the previous. Considering only the first set of the AWU data a lower cross section can be reached in the mass range even with only ∼14 % of the original exposure. For two small mass ranges 0.4–0.8 $\mathrm{GeV/c^2}$ and 1.1–2 $\mathrm{GeV/c^2}$ the Detector A limit from 2020 can be surpassed. A dent can be seen in the new limit between 0.8 and 1.1 $\mathrm{GeV/c^2}$ not surpassing the old limit. In the higher mass range the

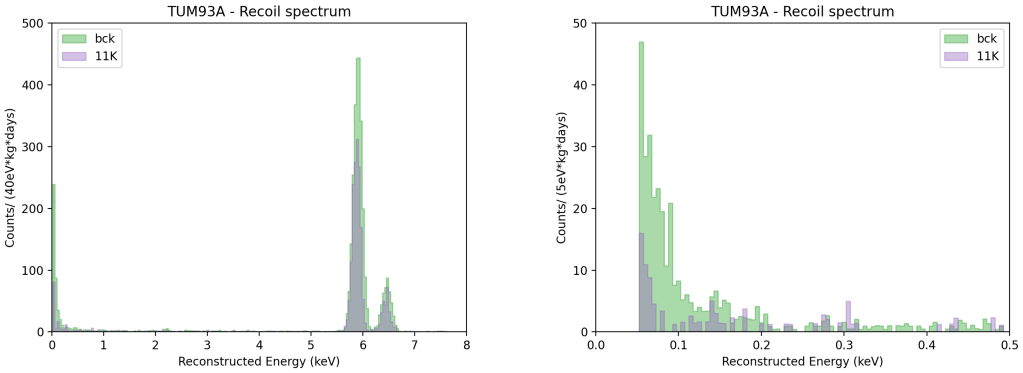

Figure 5.19: Efficiency and exposure corrected energy spectrum of the combined 11 K / AWU data (purple) and bck data (green) for the full calibrated energy range on the left and a zoom-in on the low energy region up to 500 eV on the right. The full energy spectrum features both iron lines visually resolved with expected lower count rate in the later data set. The LEE count rate is lower in the later set and reaches up to 80 eV compared to 120 eV in the bck data.

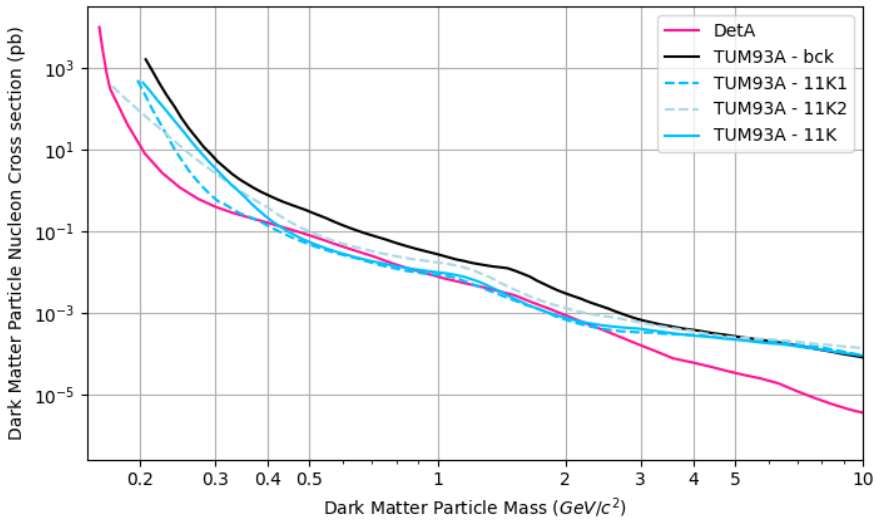

Figure 5.20: DM exclusion limit on spin-independent interactions for the TUM93A bck and 11 K data in the DM particle mass and DM particle nucleon cross section calculated in this work and Detector A (pink) [57]. The bck limit is shown in black, the full 11 K in blue, the 11 K1 in blue (dashed) and the 11 K2 in light blue (dashed). The 11 K exlusion limit reaches a slightly lower level for DM masses between 0.4–0.8 $\mathrm{GeV/c^2}$ and 1.1–2 $\mathrm{GeV/c^2}$.

new limit is limited by the low exposure, in the low masses by the threshold of the detector and the remaining LEE.

5.4 Conclusion

The TUM93A detector module shows an overall good and stable performance but falls short to explore new parameter space for the probing of DM in its initial data taking. Compared to other modules of a similar type it has a higher energy threshold and worse energy resolution. The energy spectrum is characterised by unknown excess events in the energy region between threshold and 200 eV. The rising exponential-like shape of the excess mimics a DM signal, but a time dependent decay with a decay time in the order of hundred days is observed, excluding any standard model of DM.
To gain more knowledge on the excess events and their dependence on temperature changes the cryostat was warmed up to six different temperature between 200 mK and 130 K followed by a cool down to operating temperature. For the warm-ups to 30 K and above an increased excess rate, that decayed immediately was measured. The origin of this increase is not known and still under investigation. Following each warm-up the detector showed a slightly lower threshold and energy resolution, than in the previous data taking. This could originate in the detector finding a more optimized operating point in each cycle, but also depend on other factors.
Following the observation of the time decay of the excess events a second blind DM data set was taken around 850 days after the initial cool down. In the new data set the LEE is reduced significantly in count rate and energy range. Despite the low exposure within the data set, lower interaction cross sections could be reached in the considered mass range, showing the limitation that the LEE brings to the sensitivity of the current DM search in CRESST.
It could be shown that the LEE rate reduces over time and a detector gains higher sensitivity towards lower DM interaction cross sections in the same mass range with lower LEE rate. For improvements in low mass DM search the origin and behaviour of the LEE needs to be understood. New detector concepts were developed to isolate and study the unknown events in more detail in the near future.

Chapter A

Data Selection and Templates

A.1 Signal Processing

A.1.1 Training Data

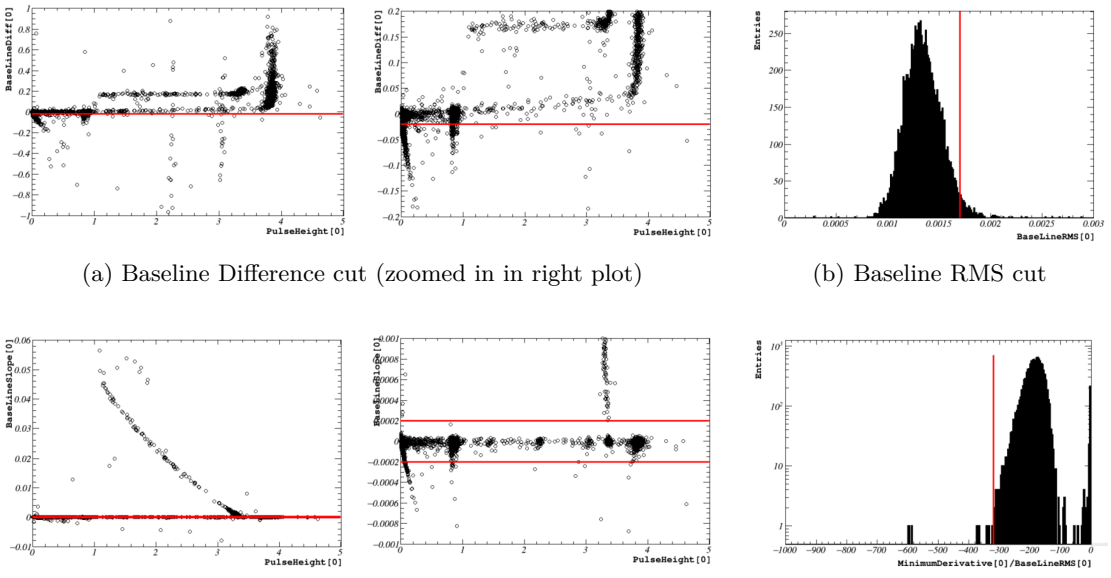

(a) Baseline Difference cut (zoomed in in right plot)

(b) Baseline RMS cut

(c) Baseline Slope cut (zoomed in on the right)

(d) Voltage Spikes cut

Figure A.1: Data Quality cuts applied to the TUM93A Phonon Channel.

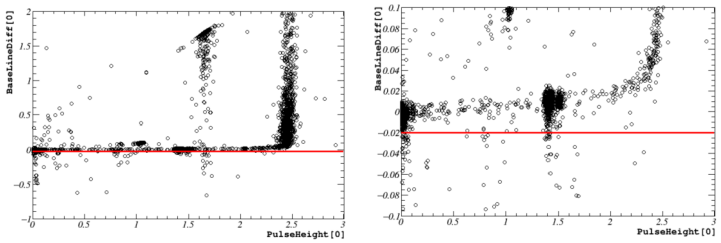

(a) Baseline Difference cut (zoomed in in right plot)

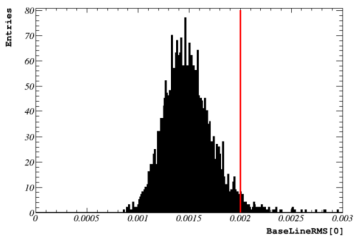

(b) Baseline RMS cut

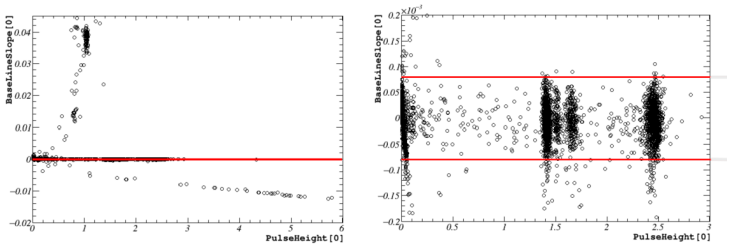

(c) Baseline Slope cut (zoomed in on the right)

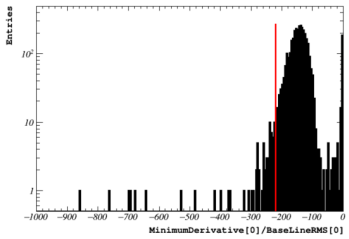

(d) Voltage Spikes cut

Figure A.2: Data Quality cuts applied to the Comm2 Phonon Channel.

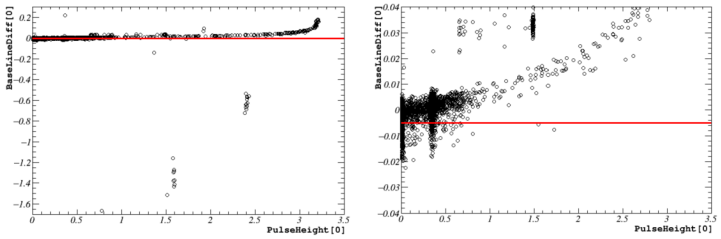

(a) Baseline Difference cut (zoomed in in right plot)

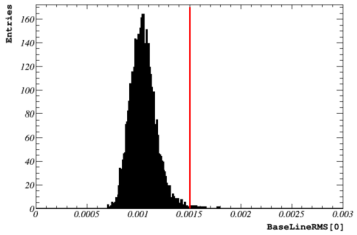

(b) Baseline RMS cut

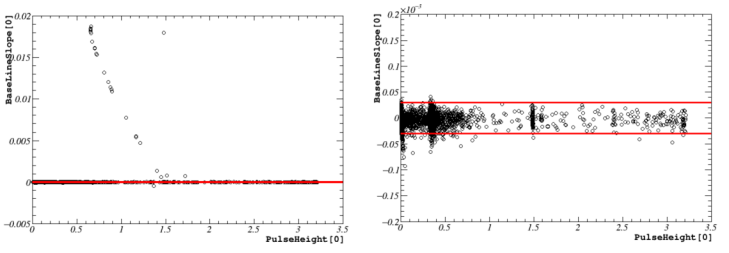

(c) Baseline Slope cut (zoomed in on the right)

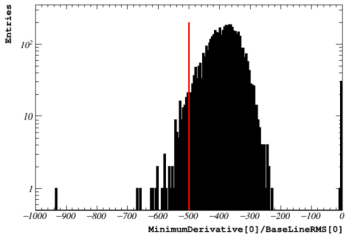

(d) Voltage Spikes cut

Figure A.3: Data Quality cuts applied to the Li1 Phonon Channel.

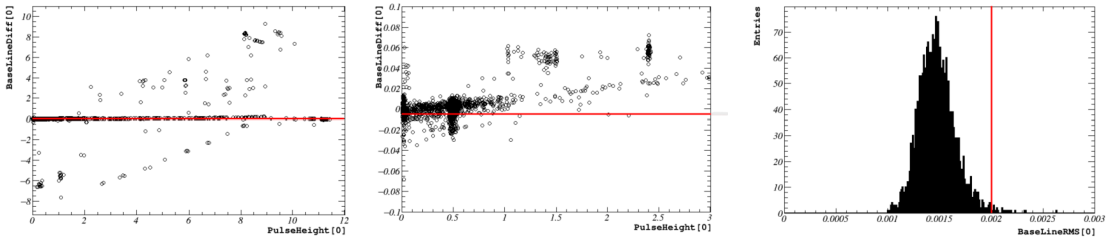

(a) Baseline Difference cut (zoomed in in right plot)

(b) Baseline RMS cut

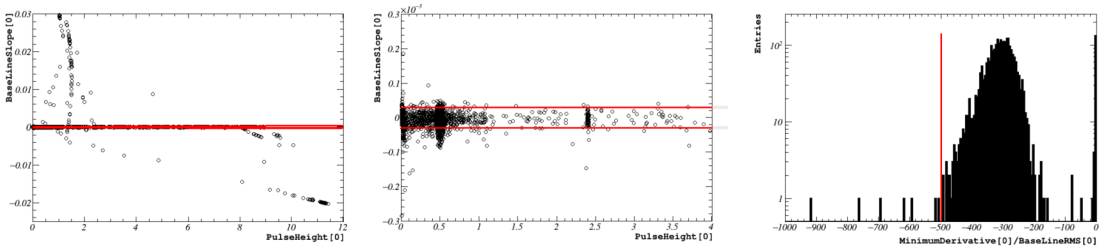

(c) Baseline Slope cut (zoomed in on the right)

(d) Voltage Spikes cut

Figure A.4: Data Quality cuts applied to the Li2 Phonon Channel.

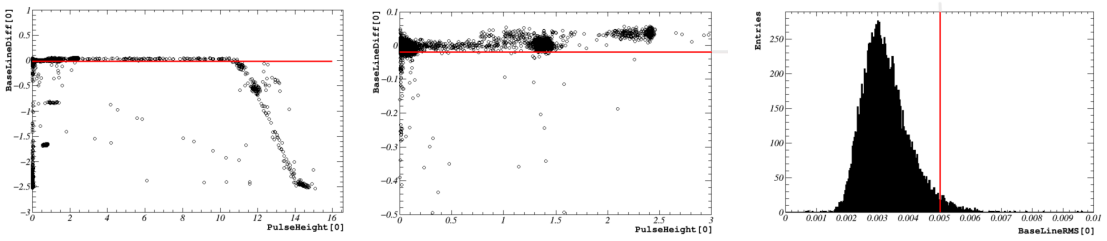

(a) Baseline Difference cut (zoomed in in right plot)

(b) Baseline RMS cut

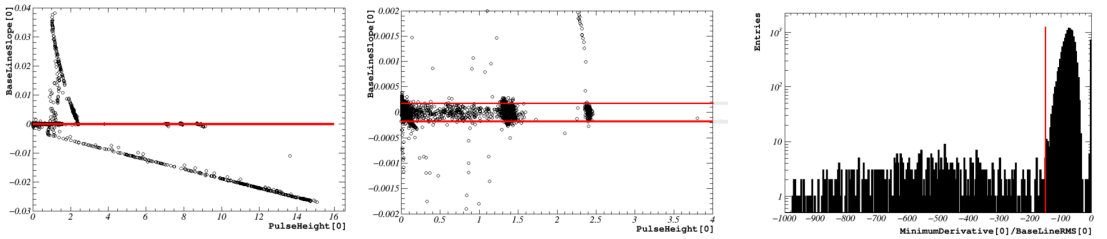

(c) Baseline Slope cut (zoomed in on the right)

(d) Voltage Spikes cut

Figure A.5: Data Quality cuts applied to the Sapp2 Phonon Channel.

A.1.2 Neutron Calibration Data

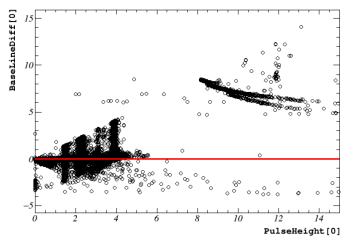

(a) Baseline Difference cut (zoomed in in right plot)

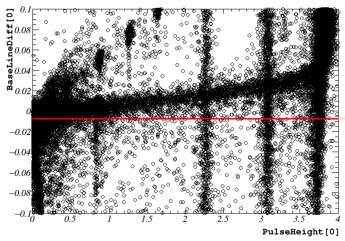

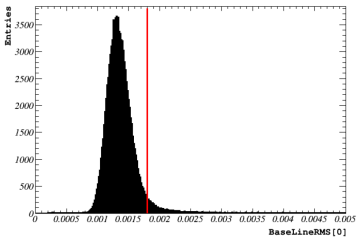

(b) Baseline RMS cut

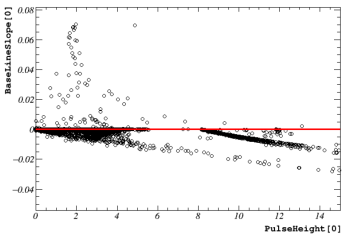

(c) Baseline Slope cut (zoomed in on the right)

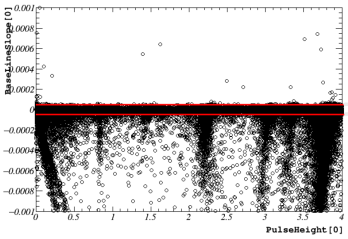

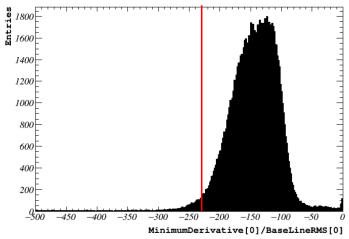

(d) Voltage Spikes cut

Figure A.6: Data Quality cuts applied to the TUM93A Phonon Channel data taken with an AmBe source installed.

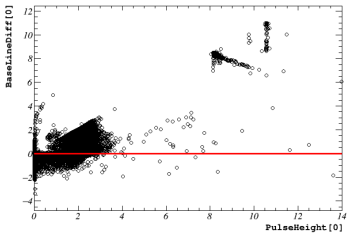

(a) Baseline Difference cut (zoomed in in right plot)

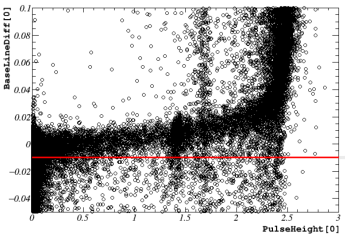

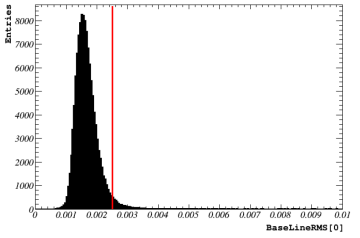

(b) Baseline RMS cut

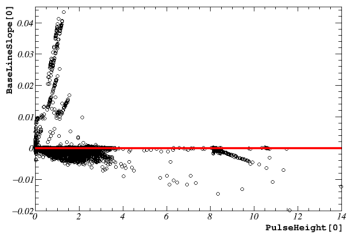

(c) Baseline Slope cut (zoomed in on the right)

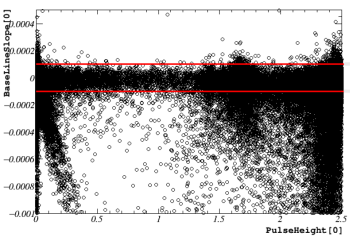

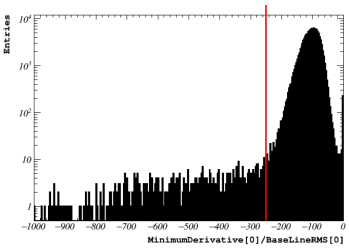

(d) Voltage Spikes cut

Figure A.7: Data Quality cuts applied to the Comm2 Phonon Channel data taken with an AmBe source installed.

A.2 Low Energy Analysis

A.2.1 Data Files

The data files used in Chapter 5. Table A.1 shows the files used for the DM analysis of the background data, Table A.2 used for the AWU DM analysis and Table A.3 used for the analysis of the warm-up tests.

training data	(bck_003 - bck_008) bck_018 bck_028 bck_039 bck_048 bck_058 bck_078 bck_089
blind data	(bck_010 - bck_014) bck_016 bck_017 (bck_019 - bck_022) (bck_024 - bck_027) (bck_030 - bck_032) bck_034 (bck_036 - bck_038) (bck_045 - bck_047) (bck_049 - bck_055) bck_057 (bck_060 - bck_062) bck_066 bck_067 (bck_070 - bck_074) bck_077 (bck_079 - bck_087) (bck_090 - bck_101) bck_120 (bck_123 - bck_125)
ncal data	(ncal_005 - ncal_022)

Table A.1: Used files in the TUM93A background data DM analysis for training and blind data set, including the neutron calibration (ncal) data used in to assist the band fit.

11 K1 training	awu11K_001 awu11K_002
11 K1 blind	awu11K_003 awu11K_004 (awu11K_007 - awu11K_014)
11 K2 training	awu11K_015 awu11K_016
11 K2 blind	(awu11K_017 - awu11K_027)

Table A.2: Used data files for analysis of data taken after the warm-up to a temperature of 11 K.

60 K	awu_bck_002 awu_bck_003 awu_bck_005 (awu_bck_007 - awu_bck_035)
600 mK	(awu_bck_037 - awu_bck_054)
200 mK	awu_bck_055 awu_bck_056 (awu_bck_063 - awu_bck_070) (awu_bck_072 - awu_bck_074) awu_bck_076 awu_bck_077
3500 mK	awu_bck_078 awu_bck_079 awu_bck_082 awu_bck_085 awu_bck_088 awu_bck_102
30 K	(awu_bck_113 - awu_bck_115) awu_bck_117 awu_bck_120 (awu_bck_122 - awu_bck_154)
130 K	(awu130K_001 - awu130K_016) (awu130K_018 - awu130K_025)
postcal	(bck_postcal_008 - bck_postcal_018)

Table A.3: Used data files in the time and temperature dependent analysis during the warm-up tests for TUM93A including the warm-ups to 60 K, 600 mK ,200 mK, 3500 mK, 30 K and 130 K and the postcal data set.

A.2.2 Data Quality Cuts

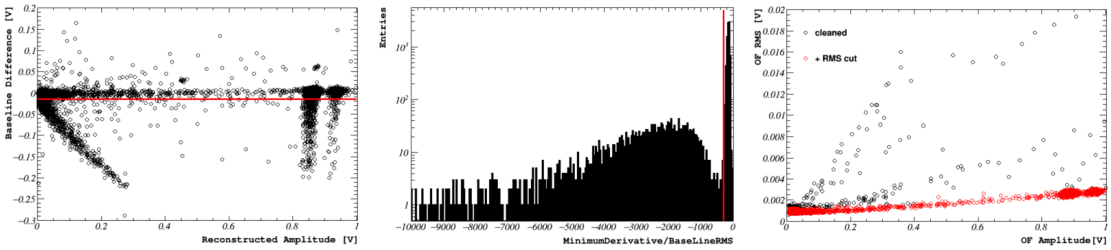

(a) Baseline Difference (b) Voltage Spikes (c) OF r.m.s. (Pulse shape)

Figure A.8: Data Quality Cuts applied to the particle events of the TUM93A phonon channel after the 60 K warm-up. The first two plots show all triggered particle events and the red line marks the applied cut. The last plot shows all particle events surviving the previous two cuts in the linear region of the detector in black and all particle events surviving an additional cut to the r.m.s. of the applied OF in red.

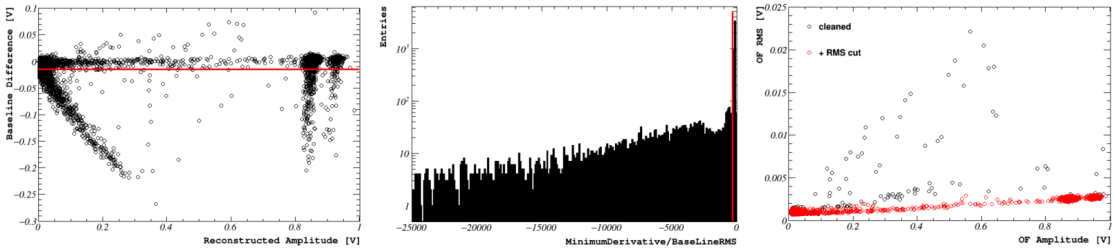

(a) Baseline Difference (b) Voltage Spikes (c) OF r.m.s. (Pulse shape)

Figure A.9: Data Quality Cuts applied to the particle events of the TUM93A phonon channel after the 600 mK warm-up. The first two plots show all triggered particle events and the red line marks the applied cut. The last plot shows all particle events surviving the previous two cuts in the linear region of the detector in black and all particle events surviving an additional cut to the r.m.s. of the applied OF in red.

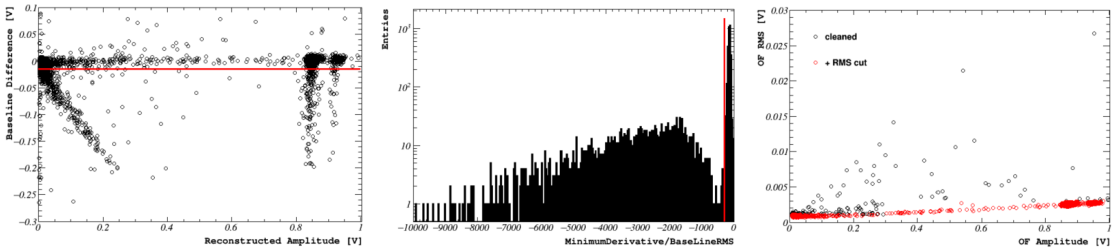

(a) Baseline Difference (b) Voltage Spikes (c) OF r.m.s. (Pulse shape)

Figure A.10: Data Quality Cuts applied to the particle events of the TUM93A phonon channel after the 200 mK warm-up. The first two plots show all triggered particle events and the red line marks the applied cut. The last plot shows all particle events surviving the previous two cuts in the linear region of the detector in black and all particle events surviving an additional cut to the r.m.s. of the applied OF in red.

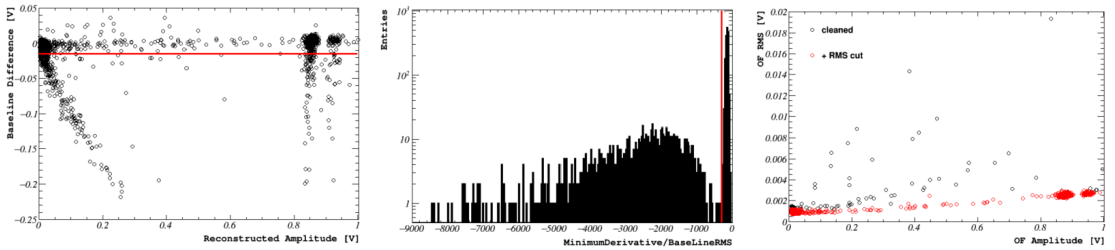

(a) Baseline Difference (b) Voltage Spikes (c) OF r.m.s. (Pulse shape)

Figure A.11: Data Quality Cuts applied to the particle events of the TUM93A phonon channel after the 3.5 K warm-up. The first two plots show all triggered particle events and the red line marks the applied cut. The last plot shows all particle events surviving the previous two cuts in the linear region of the detector in black and all particle events surviving an additional cut to the r.m.s. of the applied OF in red.

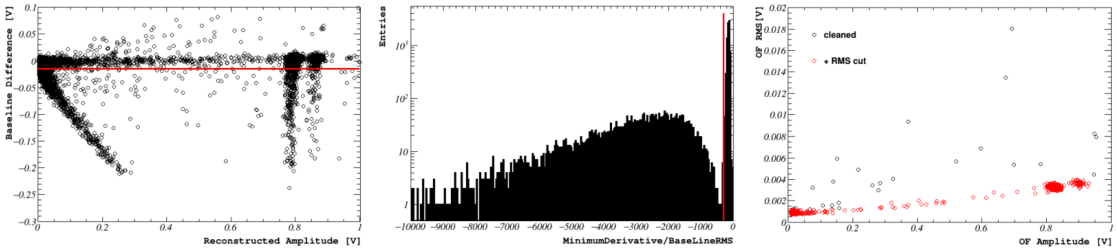

(a) Baseline Difference (b) Voltage Spikes (c) OF r.m.s. (Pulse shape)

Figure A.12: Data Quality Cuts applied to the particle events of the TUM93A phonon channel after the 30 K warm-up. The first two plots show all triggered particle events and the red line marks the applied cut. The last plot shows all particle events surviving the previous two cuts in the linear region of the detector in black and all particle events surviving an additional cut to the r.m.s. of the applied OF in red.

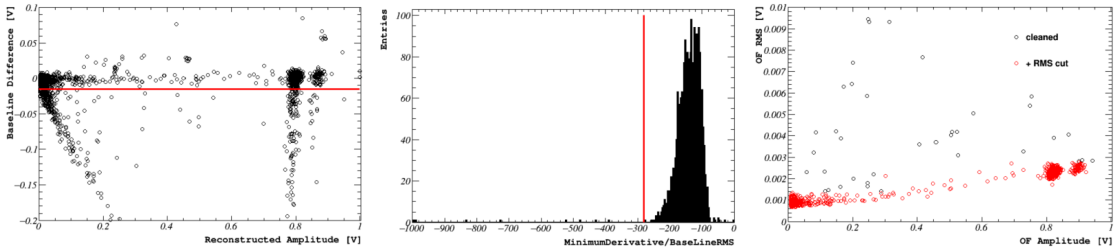

(a) Baseline Difference (b) Voltage Spikes (c) OF r.m.s. (Pulse shape)

Figure A.13: Data Quality Cuts applied to the particle events of the TUM93A phonon channel after the 11 K warm-up. The first two plots show all triggered particle events and the red line marks the applied cut. The last plot shows all particle events surviving the previous two cuts in the linear region of the detector in black and all particle events surviving an additional cut to the r.m.s. of the applied OF in red.

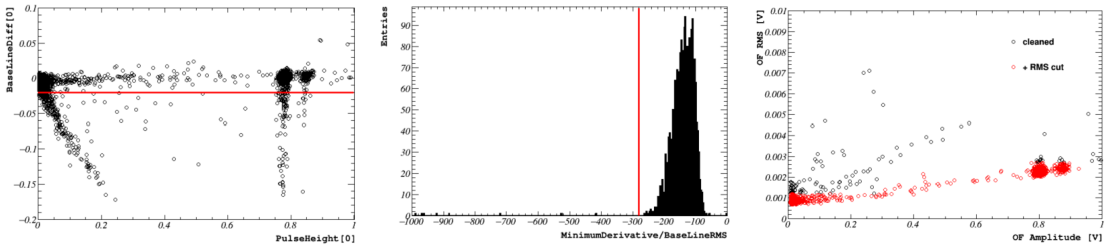

(a) Baseline Difference (b) Voltage Spikes (c) OF r.m.s. (Pulse shape)

Figure A.14: Data Quality Cuts applied to the particle events of the TUM93A phonon channel during the 11 K2 data set. The first two plots show all triggered particle events and the red line marks the applied cut. The last plot shows all particle events surviving the previous two cuts in the linear region of the detector in black and all particle events surviving an additional cut to the r.m.s. of the applied OF in red.

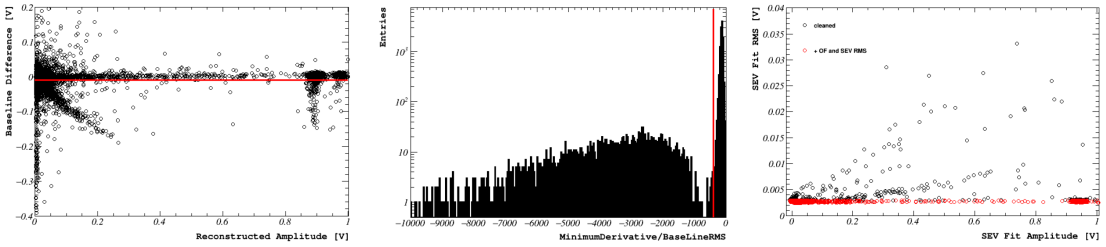

(a) Baseline Difference (b) Voltage Spikes (c) OF and SEV r.m.s.

Figure A.15: Data Quality Cuts applied to the particle events of the TUM93A phonon channel after the 130 K warm-up. The first two plots show all triggered particle events and the red line marks the applied cut. The last plot shows all particle events surviving the previous two cuts in the linear region of the detector in black and all particle events surviving an additional cut to the r.m.s. of the applied OF and the SEV fit in red.

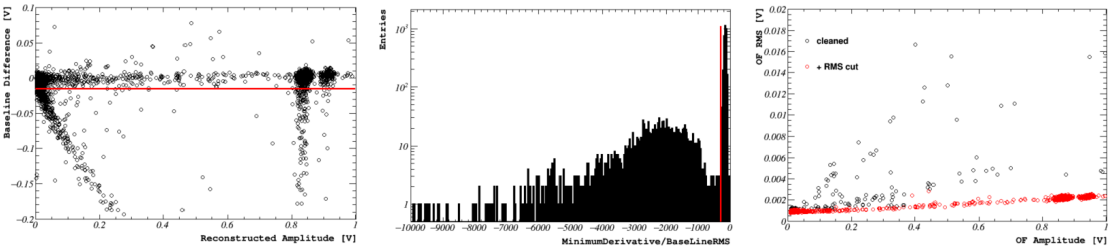

(a) Baseline Difference (b) Voltage Spikes (c) OF r.m.s. (Pulse shape)

Figure A.16: Data Quality Cuts applied to the particle events of the TUM93A phonon channel during the postcal data set. The first two plots show all triggered particle events and the red line marks the applied cut. The last plot shows all particle events surviving the previous two cuts in the linear region of the detector in black and all particle events surviving an additional cut to the r.m.s. of the applied OF in red.

A.2.3 Warm-up Templates

This section shows NPS, SEV templates and OFs of each data set during the warm-up tests and the postcal data in comparison to the previous data set.

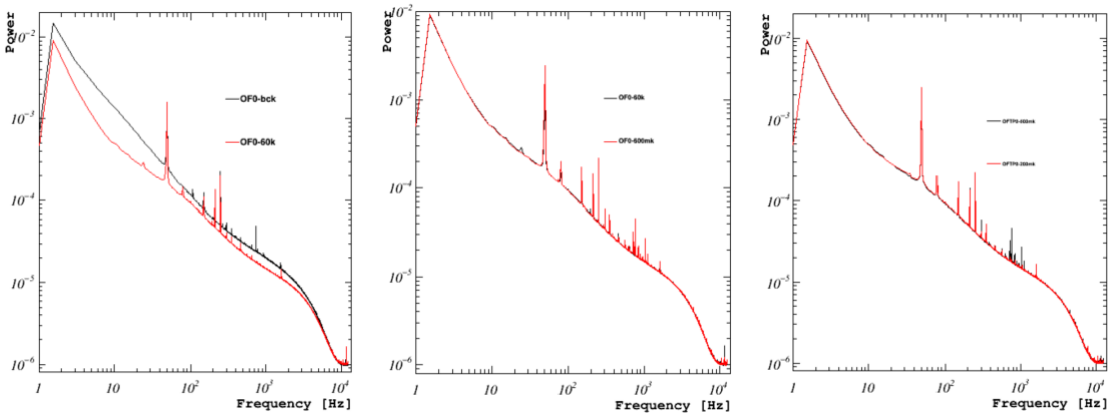

(a) 60 K (b) 600 mK (c) 200 mK

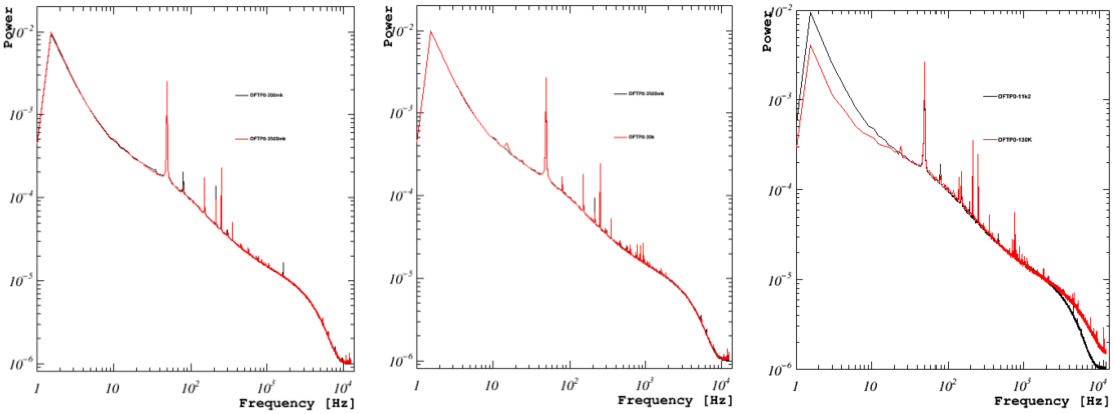

(d) 3500 mK (e) 30 K (f) 130 K

Figure A.17: NPS of the phonon channel for data sets after each warm-up test. The red curves shows the NPS of the considered data set, the black curves the NPS of the previous data set.

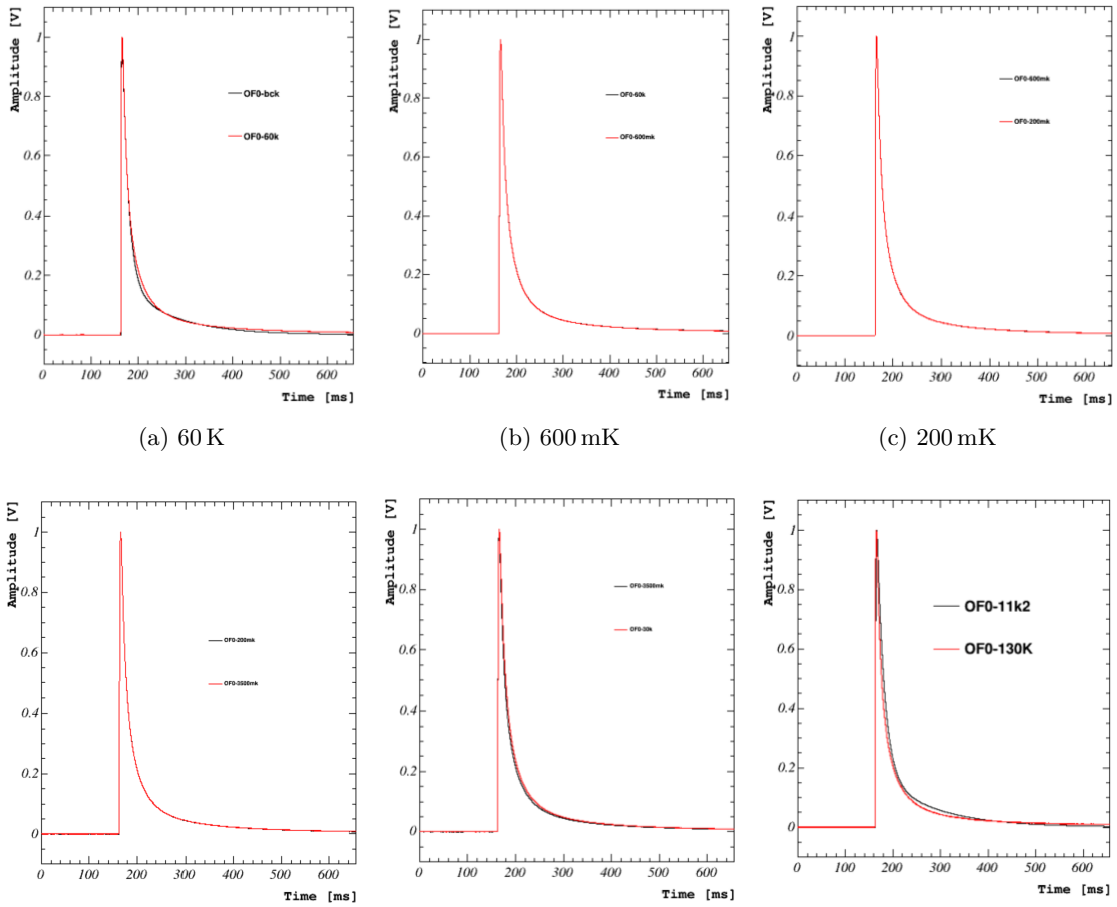

(a) 60 K (b) 600 mK (c) 200 mK

(d) 3500 mK (e) 30 K (f) 130 K

Figure A.18: SEV for particle events in the phonon channel for data sets after each warm-up test. The red curves shows the SEV of the considered data set, the black curves the SEV of the previous data set.

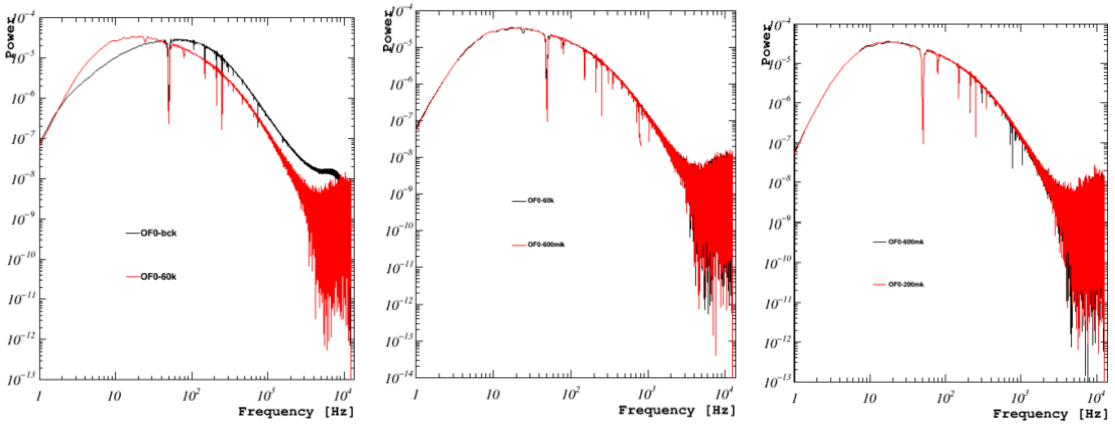

(a) 60 K (b) 600 mK (c) 200 mK

(d) 3500 mK (e) 30 K (f) 130 K

Figure A.19: OF for particle events in the phonon channel for data sets after each warm-up test. The red curves shows the OF of the considered data set, the black curves the OF of the previous data set.

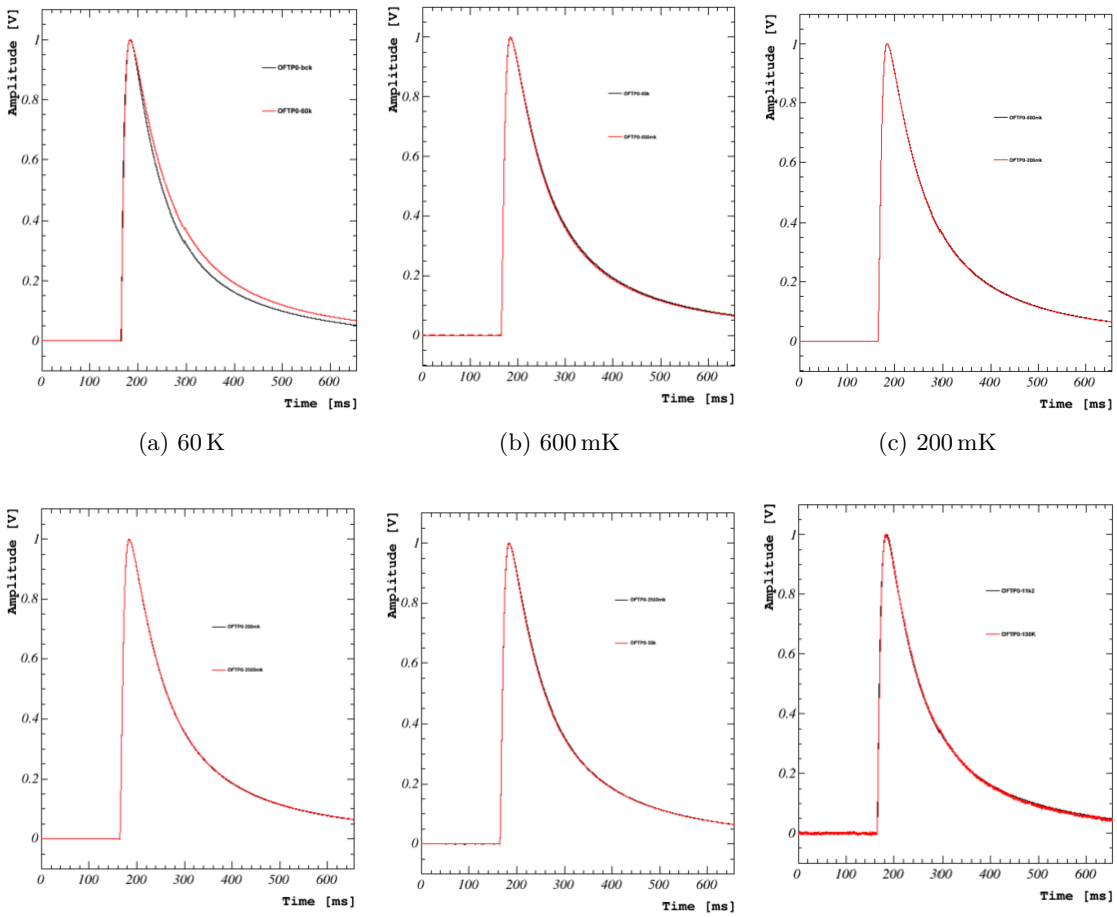

(a) 60 K (b) 600 mK (c) 200 mK

(d) 3500 mK (e) 30 K (f) 130 K

Figure A.20: SEV for test pulse events in the phonon channel for data sets after each warm-up test. The red curves shows the SEV of the considered data set, the black curves the SEV of the previous data set.

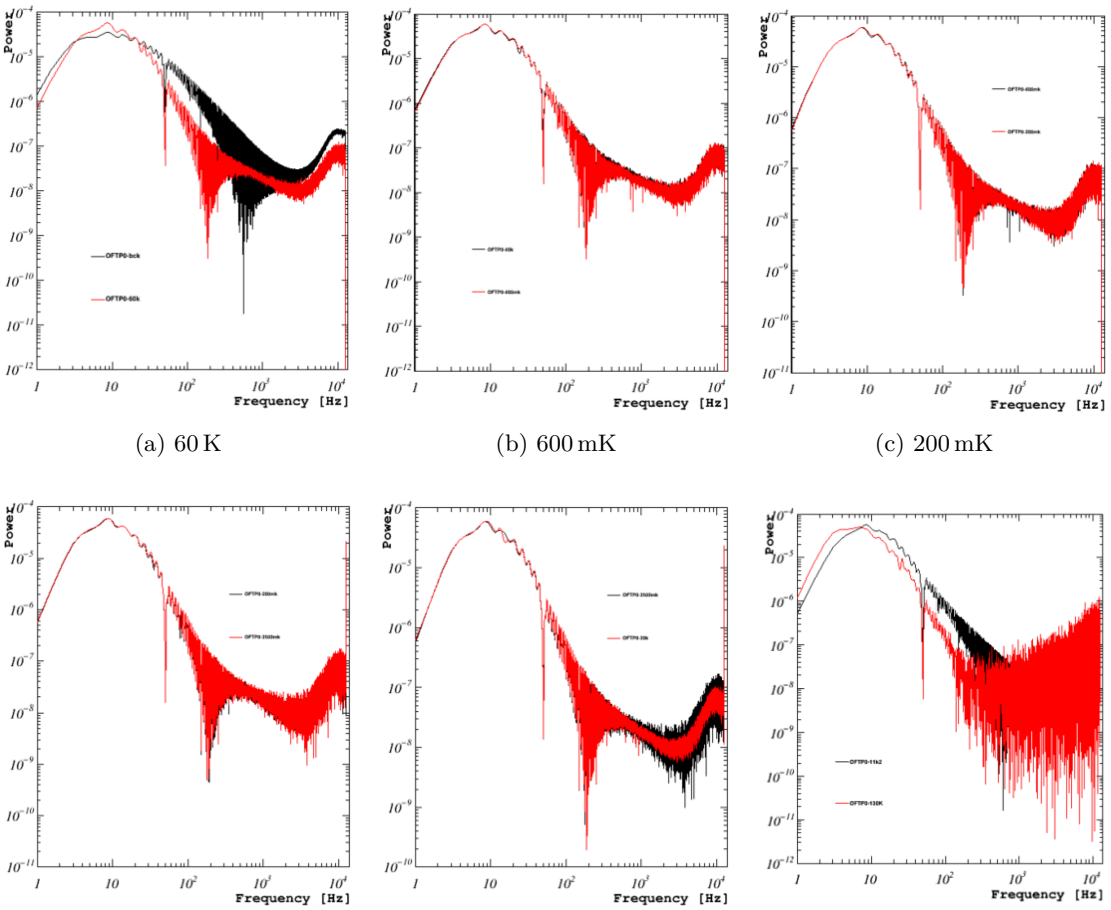

(a) 60 K (b) 600 mK (c) 200 mK

(d) 3500 mK (e) 30 K (f) 130 K

Figure A.21: OF for test pulse events in the phonon channel for data sets after each warm-up test. The red curves shows the OF of the considered data set, the black curves the OF of the previous data set.

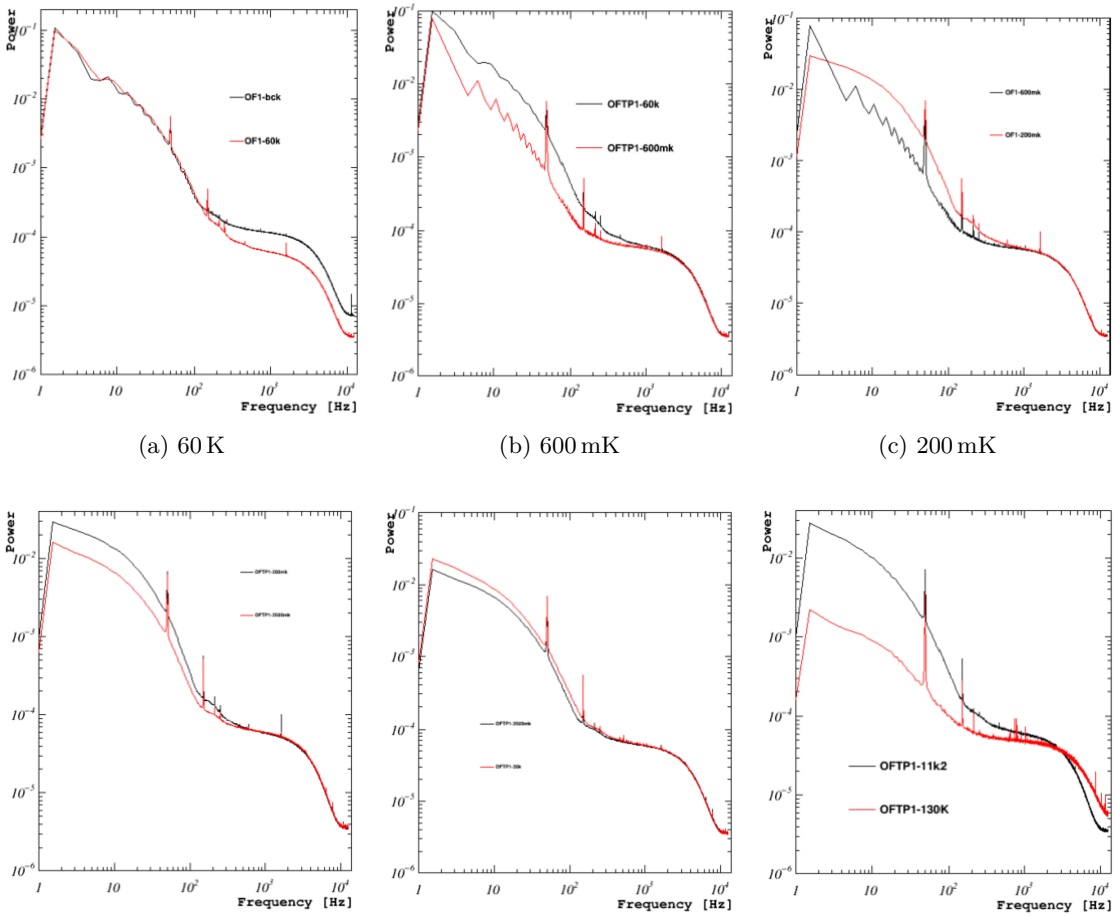

(a) 60 K (b) 600 mK (c) 200 mK

(d) 3500 mK (e) 30 K (f) 130 K

Figure A.22: NPS of the light channel for data sets after each warm-up test. The red curves shows the NPS of the considered data set, the black curves the NPS of the previous data set.

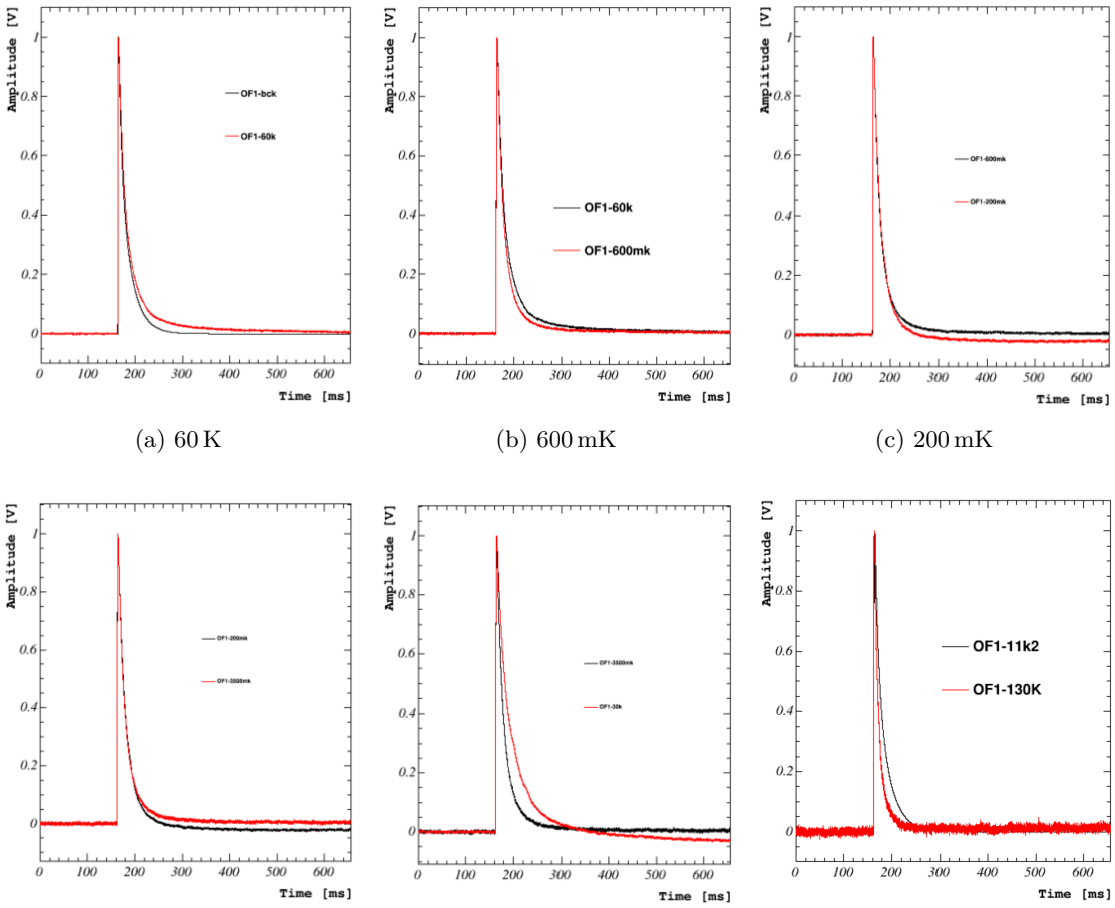

(a) 60 K (b) 600 mK (c) 200 mK

(d) 3500 mK (e) 30 K (f) 130 K

Figure A.23: SEV for particle events in the light channel for data sets after each warm-up test. The red curves shows the SEV of the considered data set, the black curves the SEV of the previous data set.

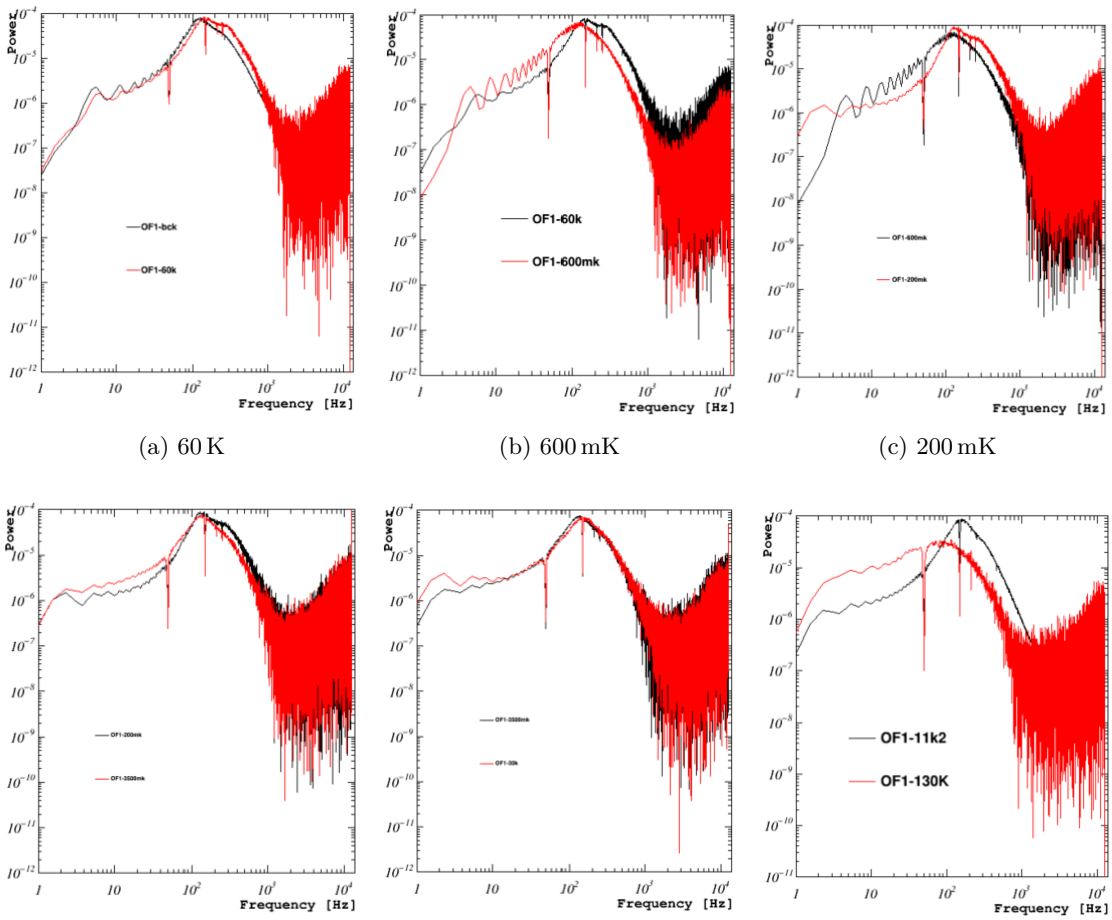

(a) 60 K (b) 600 mK (c) 200 mK

(d) 3500 mK (e) 30 K (f) 130 K

Figure A.24: OF for particle events in the light channel for data sets after each warm-up test. The red curves shows the OF of the considered data set, the black curves the OF of the previous data set.

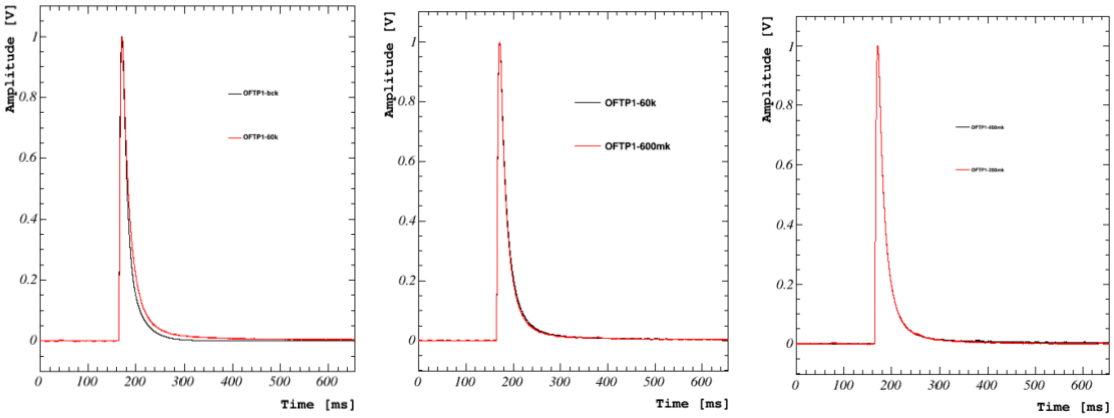

(a) 60 K (b) 600 mK (c) 200 mK

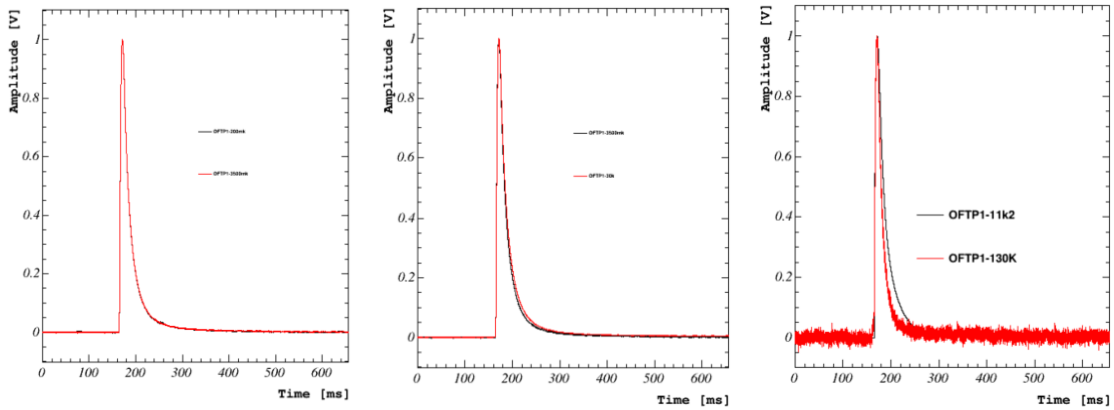

(d) 3500 mK (e) 30 K (f) 130 K

Figure A.25: SEV for test pulse events in the light channel for data sets after each warm-up test. The red curves shows the SEV of the considered data set, the black curves the SEV of the previous data set.

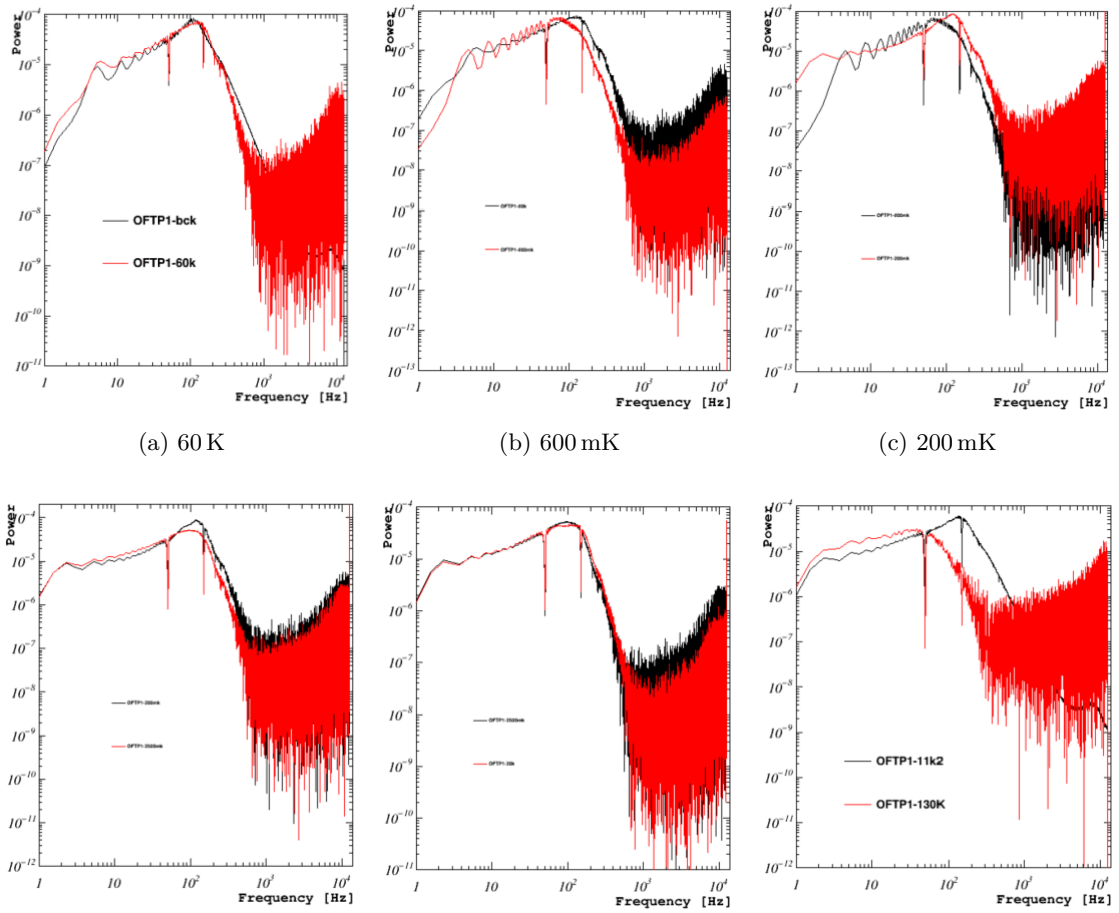

(a) 60 K (b) 600 mK (c) 200 mK

(d) 3500 mK (e) 30 K (f) 130 K

Figure A.26: OF for test pulse events in the light channel for data sets after each warm-up test. The red curves shows the OF of the considered data set, the black curves the OF of the previous data set.

A.2.4 Recoil Spectra

Survival Probability

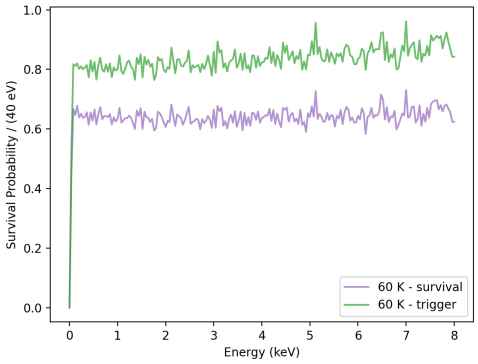

(a) 60 K

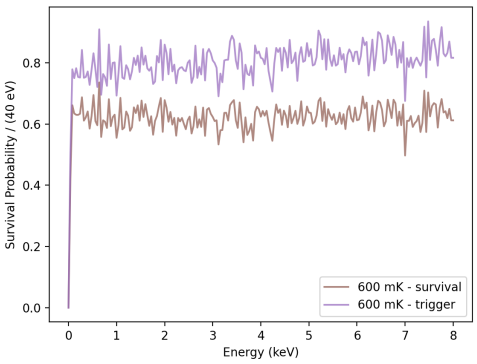

(b) 600 mK

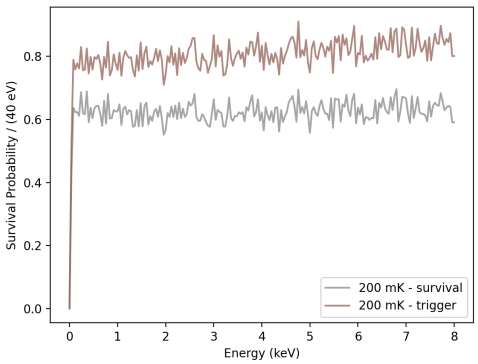

(c) 200 mK

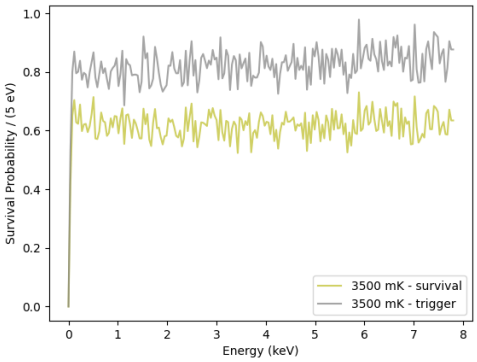

(d) 3500 mK

Figure A.27: Survival probability over energy after the 60 K, 600 mK, 200 mK and 3500 mK warm-up test. The survival probability is similar in all data sets. Shorter data sets show a higher fluctuations due to lack of statistics.

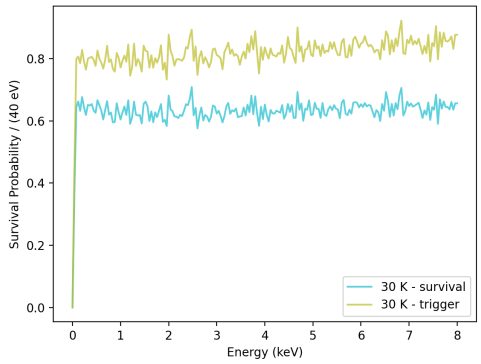

(a) 30 K

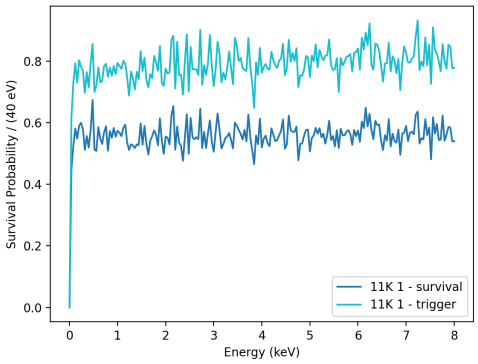

(b) 11 K1

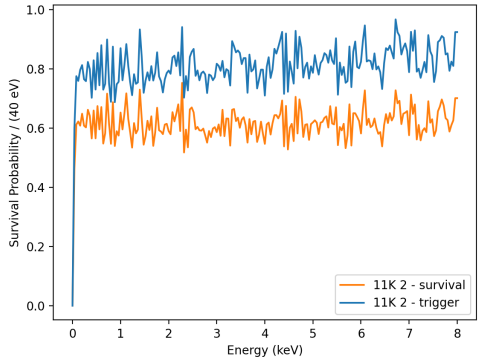

(c) 11 K2

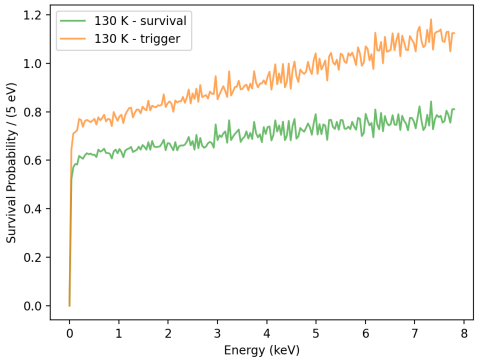

(d) 130 K

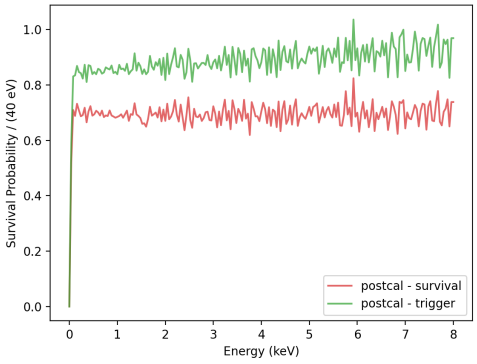

(e) postcal

Figure A.28: Survival probability over energy after the 30 K , 11 K and 130 K warm-up test and during the postcal data. The survival probability is similar in all data sets. Shorter data sets show a higher fluctuations due to lack of statistics.

Reconstructed and Corrected Energy

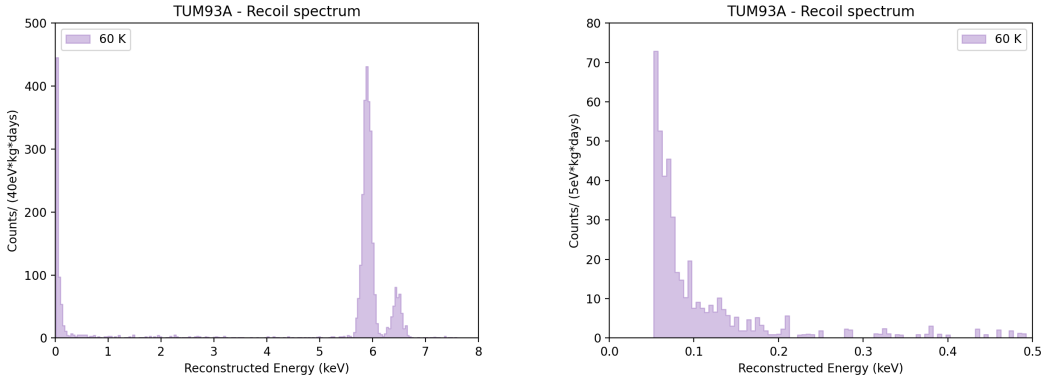

(a) Full linear energy spectrum

(b) Low energy region

Figure A.29: Efficiency and exposure corrected energy spectrum for the full calibrated energy range after the 60 K warm-up on the left and a zoom-in on the low energy region up to 500 eV on the right. The full energy spectrum features both iron lines visually resolved. The low energy ROI shows the LEE.

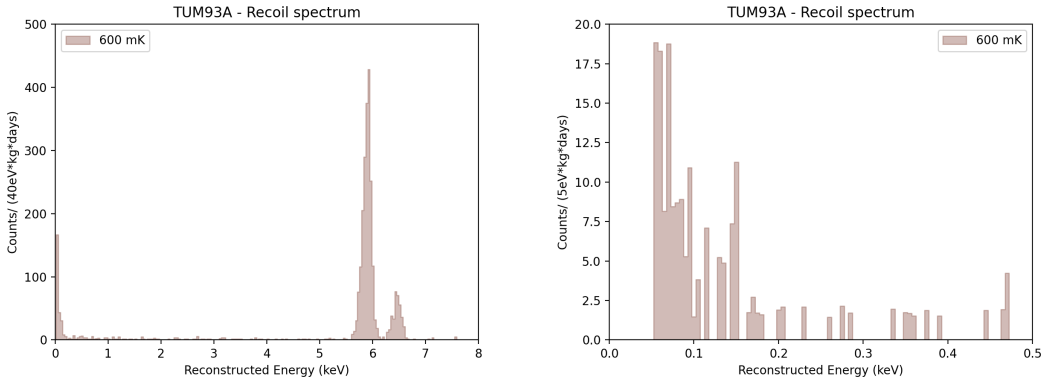

(a) Full linear energy spectrum

(b) Low energy region

Figure A.30: Efficiency and exposure corrected energy spectrum for the full calibrated energy range after the 600 mK warm-up on the left and a zoom-in on the low energy region up to 500 eV on the right. The full energy spectrum features both iron lines visually resolved. The low energy ROI shows the LEE.

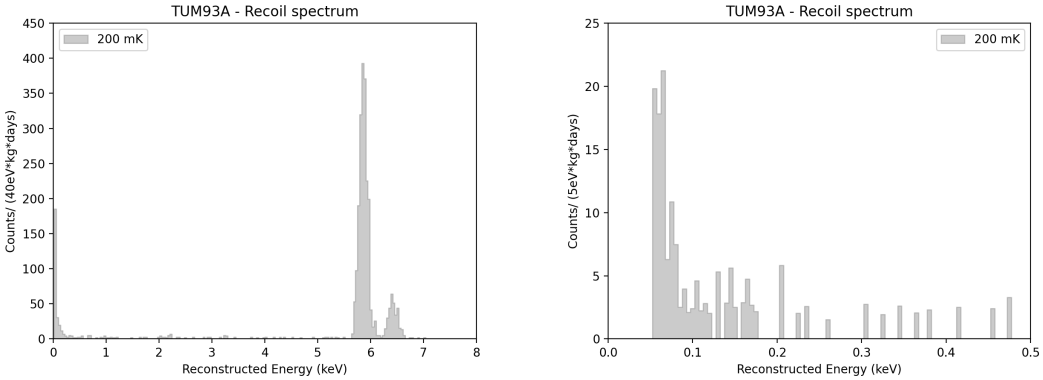

(a) Full linear energy spectrum (b) Low energy region

Figure A.31: Efficiency and exposure corrected energy spectrum for the full calibrated energy range after the 200 mK warm-up on the left and a zoom-in on the low energy region up to 500 eV on the right. The full energy spectrum features both iron lines visually resolved. The low energy ROI shows the LEE.

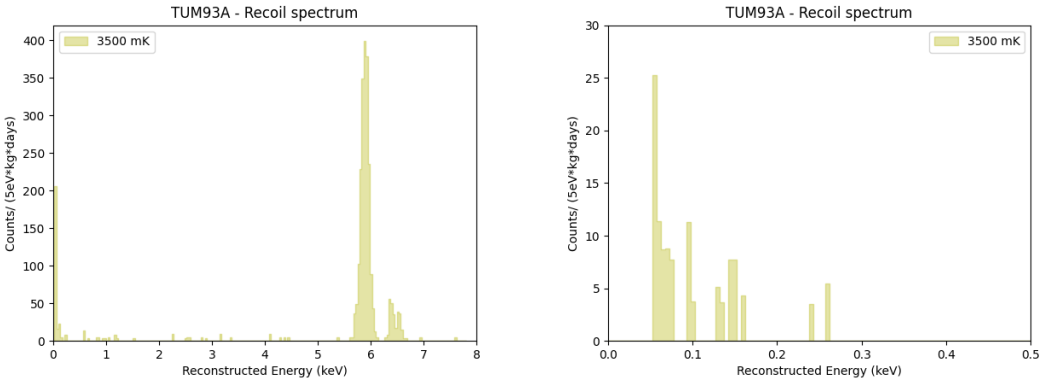

(a) Full linear energy spectrum (b) Low energy region

Figure A.32: Efficiency and exposure corrected energy spectrum for the full calibrated energy range after the 3500 mK warm-up on the left and a zoom-in on the low energy region up to 500 eV on the right. The full energy spectrum features both iron lines visually resolved. The low energy ROI shows the LEE.

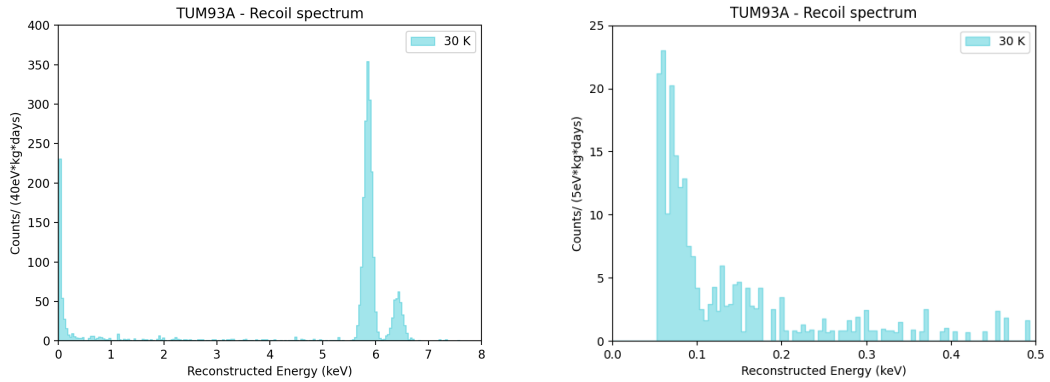

(a) Full linear energy spectrum (b) Low energy region

Figure A.33: Efficiency and exposure corrected energy spectrum for the full calibrated energy range after the 30 K warm-up on the left and a zoom-in on the low energy region up to 500 eV on the right. The full energy spectrum features both iron lines visually resolved. The low energy ROI shows the LEE.

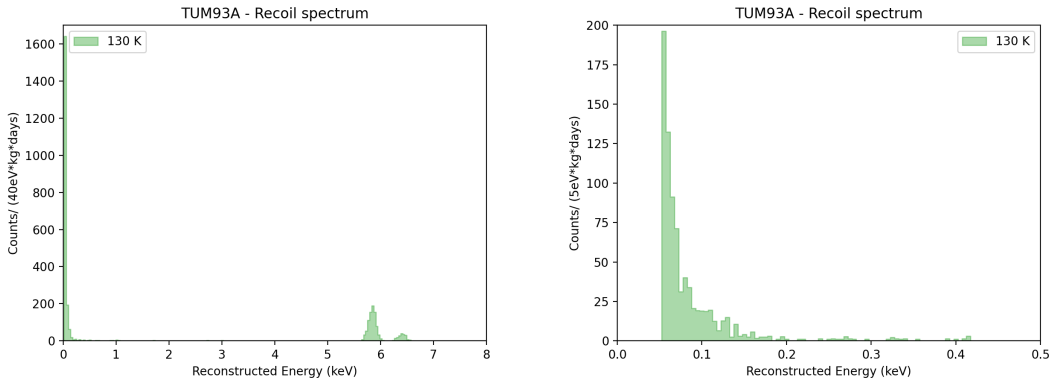

(a) Full linear energy spectrum (b) Low energy region

Figure A.34: Efficiency and exposure corrected energy spectrum for the full calibrated energy range after the 130 K warm-up on the left and a zoom-in on the low energy region up to 500 eV on the right. The full energy spectrum features both iron lines visually resolved. The low energy ROI shows the LEE.

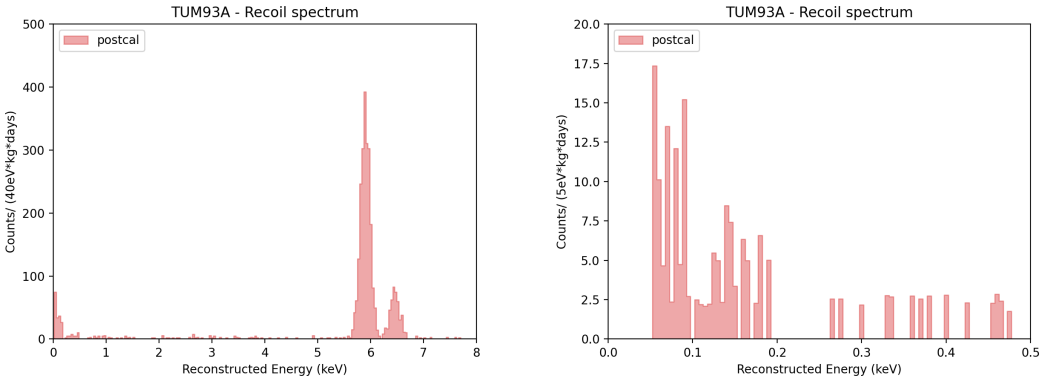

(a) Full linear energy spectrum

(b) Low energy region

Figure A.35: Efficiency and exposure corrected energy spectrum for the full calibrated energy range during the postcal data set on the left and a zoom-in on the low energy region up to 500 eV on the right. The full energy spectrum features both iron lines visually resolved. The low energy ROI shows the LEE.

List of Abbreviations

List of Figures

List of Tables

Bibliography

[1] N. Ferreiro Iachellini. "Increasing the sensitivity to low mass dark matter in CRESST-III with a new DAQ and signal processing". PhD thesis. Ludwig-Maximilians-Universität München, 2018.

[2] E. Gatti and P. F. Manfredi. "Processing the Signals From Solid State Detectors in Elementary Particle Physics". In: *Riv. Nuovo Cim.* 9N1 (1986), pp. 1–146. DOI: 10.1007/BF02822156.

[3] G. Angloher et al. "Results on sub-GeV dark matter from a 10 eV threshold CRESST-III silicon detector". In: *Phys. Rev. D* 107 (12 2023), p. 122003. DOI: 10.1103/PhysRevD.107.122003.

[4] A. Kinast. "Enhancing the Dark Matter Sensitivity of CRESST: Purification, Stress Reduction and 17O Enrichment of CaWO4 Target Crystals". Dissertation. München: Technische Universität München, 2023.

[5] F. Zwicky. "Die Rotverschiebung von extragalaktischen Nebeln". In: *Helv. Phys. Acta* 6 (1933), pp. 110–127. DOI: 10.5169/seals-110267.

[6] R. Clausius. "Ueber einen auf die Wärme anwendbaren mechanischen Satz". In: *Annalen der Physik* 217.9 (1870), pp. 124–130. DOI: 10.1002/andp.18702170911.

[7] V. C. Rubin and W. K. Ford Jr. "Rotation of the Andromeda Nebula from a Spectroscopic Survey of Emission Regions". In: *Astrophys. J. 159: 379-403* (1970). DOI: 10.1086/150317.

[8] V. C. Rubin, W. K. Ford Jr., and N. Thonnard. "Rotational properties of 21 SC galaxies with a large range of luminosities and radii, from NGC 4605 (R=4kpc) to UGC 2885 (R=122kpc)." In: *Astrophys. J. 238: 471-487* (1980).

[9] T. S. van Albada et al. "Distribution of dark matter in the spiral galaxy NGC 3198." In: *The Astrophysical Journal* 295 (1985), pp. 305–313. DOI: 10.1086/163375.

[10] D. Clowe et al. "A Direct Empirical Proof of the Existence of Dark Matter*". In: *The Astrophysical Journal* 648.2 (2006), p. L109. DOI: 10.1086/508162.

[11] R. K. Sachs and A. M. Wolfe. "Perturbations of a Cosmological Model and Angular Variations of the Microwave Background". In: *The Astrophysical Journal* 147 (1967), p. 73. DOI: 10.1086/148982.

[12] Planck Collaboration et al. "Planck 2018 results - VI. Cosmological parameters". In: *A&A* 641 (2020), A6. DOI: 10.1051/0004-6361/201833910.

[13] N. Yoshida. *Structure Formation in the Early Universe*. 2009. arXiv: 0906.4372 [astro-ph.CO].

[14] V. Springel et al. "Simulations of the formation, evolution and clustering of galaxies and quasars". In: *Nature* 435.7042 (2005), pp. 629–636. ISSN: 1476-4687. DOI: 10.1038/nature03597.

[15] Ya. B. Zel'dovich, L. B. Okun', and S. B. Pikel'ner. "QUARKS: ASTROPHYSICAL AND PHYSICOCHEMICAL ASPECTS". In: *Soviet Physics Uspekhi* 8.5 (1966), p. 702. DOI: 10.1070/PU1966v008n05ABEH003030.

[16] G. Jungman, M. Kamionkowski, and K. Griest. "Supersymmetric dark matter". In: *Physics Reports* 267.5 (1996), pp. 195–373. ISSN: 0370-1573. DOI: doi.org/10.1016/0370-1573(95)00058-5.

[17] B. W. Lee and S. Weinberg. "Cosmological Lower Bound on Heavy-Neutrino Masses". In: *Phys. Rev. Lett.* 39 (4 1977), pp. 165–168. DOI: 10.1103/PhysRevLett.39.165.

[18] J. L. Feng. "Dark Matter Candidates from Particle Physics and Methods of Detection". In: *Annual Review of Astronomy and Astrophysics* 48.1 (2010), pp. 495–545. ISSN: 1545-4282. DOI: 10.1146/annurev-astro-082708-101659.

[19] J. M. Pendlebury et al. "Revised experimental upper limit on the electric dipole moment of the neutron". In: *Physical Review D* 92.9 (2015). ISSN: 1550-2368. DOI: 10.1103/physrevd.92.092003.

[20] J. E. Kim and G. Carosi. "Axions and the strong CP problem". In: *Rev. Mod. Phys.* 82 (1 2010), pp. 557–601. DOI: 10.1103/RevModPhys.82.557.

[21] R. D. Peccei and H. R. Quinn. "CP Conservation in the Presence of Pseudoparticles". In: *Phys. Rev. Lett.* 38 (25 1977), pp. 1440–1443. DOI: 10.1103/PhysRevLett.38.1440.

[22] F. Wilczek. "Problem of Strong P and T Invariance in the Presence of Instantons". In: *Phys. Rev. Lett.* 40 (5 1978), pp. 279–282. DOI: 10.1103/PhysRevLett.40.279.

[23] B. J. Carr and S. W. Hawking. "Black holes in the early Universe". In: *Monthly Notices of the Royal Astronomical Society* 168 (1974), pp. 399–416. DOI: 10.1093/mnras/168.2.399.

[24] I. D. Novikov et al. "Primordial black holes". In: *A&A* 80.1 (1979), pp. 104–109.

[25] M. Milgrom. "A modification of the Newtonian dynamics as a possible alternative to the hidden mass hypothesis." In: *The Astrophysical Journal* 270 (1983), pp. 365–370. DOI: 10.1086/161130.

[26] J. D. Bekenstein. "Relativistic gravitation theory for the modified Newtonian dynamics paradigm". In: *Phys. Rev. D* 70 (8 2004), p. 083509. DOI: 10.1103/PhysRevD.70.083509.

[27] C. Skordis and T. Zlosnik. "New Relativistic Theory for Modified Newtonian Dynamics". In: *Phys. Rev. Lett.* 127 (16 2021), p. 161302. DOI: 10.1103/PhysRevLett.127.161302.

[28] J.D. Lewin and P.F. Smith. "Review of mathematics, numerical factors, and corrections for dark matter experiments based on elastic nuclear recoil". In: *Astroparticle Physics* 6.1 (1996), pp. 87–112. ISSN: 0927-6505. DOI: doi.org/10.1016/S0927-6505(96)00047-3.

[29] F. Donato, N. Fornengo, and S. Scopel. "Effects of galactic dark halo rotation on WIMP direct detection". In: *Astroparticle Physics* 9.3 (1998), pp. 247–260. ISSN: 0927-6505. DOI: https://doi.org/10.1016/S0927-6505(98)00025-5.

[30] J. Engel, S. Pittel, and P. Vogel. "NUCLEAR PHYSICS OF DARK MATTER DETECTION". In: *International Journal of Modern Physics E* 01.01 (1992), pp. 1–37. DOI: 10.1142/S0218301392000023.

[31] R. H. Helm. "Inelastic and Elastic Scattering of 187-Mev Electrons from Selected Even-Even Nuclei". In: *Phys. Rev.* 104 (5 1956), pp. 1466–1475. DOI: 10.1103/PhysRev.104.1466.

[32] A. Gütlein et al. *Solar and Atmospheric Neutrinos: Limitations for Direct Dark Matter Searches*. 2010. arXiv: 1009.3815 [hep-ph].

[33] D. Speller and (for the SuperCDMS Collaboration). "Dark matter direct detection with SuperCDMS Soudan". In: *Journal of Physics: Conference Series* 606.1 (2015), p. 012003. DOI: 10.1088/1742-6596/606/1/012003.

[34] J. Gascon and the EDELWEISS Collaboration. "Recent results from EDELWEISS Dark Matter searches". In: *Journal of Physics: Conference Series* 1468.1 (2020), p. 012018. DOI: 10.1088/1742-6596/1468/1/012018.

[35] E. Aprile et al. "Light Dark Matter Search with Ionization Signals in XENON1T". In: *Phys. Rev. Lett.* 123 (25 2019), p. 251801. DOI: 10.1103/PhysRevLett.123.251801.

[36] J. Aalbers et al. "First Dark Matter Search Results from the LUX-ZEPLIN (LZ) Experiment". In: *Phys. Rev. Lett.* 131 (4 2023), p. 041002. DOI: 10.1103/PhysRevLett.131.041002.

[37] P. Agnes et al. "Low-Mass Dark Matter Search with the DarkSide-50 Experiment". In: *Phys. Rev. Lett.* 121 (8 2018), p. 081307. DOI: 10.1103/PhysRevLett.121.081307.

[38] T. Bringmann and C. Weniger. "Gamma ray signals from dark matter: Concepts, status and prospects". In: *Physics of the Dark Universe* 1.1 (2012). Next Decade in Dark Matter and Dark Energy, pp. 194–217. ISSN: 2212-6864. DOI: 10.1016/j.dark.2012.10.005.

[39] M. Cirelli et al. "Model-independent implications of the e±, p^{-} cosmic ray spectra on properties of Dark Matter". In: *Nuclear Physics B* 813.1 (2009), pp. 1–21. ISSN: 0550-3213. DOI: 10.1016/j.nuclphysb.2008.11.031.

[40] B. Chauhan et al. *Neutrino constraints on inelastic dark matter captured in the Sun*. 2023. arXiv: 2308.16134 [hep-ph].

[41] K. Frankiewicz. *Searching for Dark Matter Annihilation into Neutrinos with Super-Kamiokande*. 2015. arXiv: 1510.07999 [hep-ex].

[42] R. Abbasi et al. "Search for GeV-scale dark matter annihilation in the Sun with IceCube DeepCore". In: *Physical Review D* 105.6 (2022). ISSN: 2470-0029. DOI: 10.1103/physrevd.105.062004.

[43] A. Boveia and C. Doglioni. "Dark Matter Searches at Colliders". In: *Annual Review of Nuclear and Particle Science* 68.1 (2018), pp. 429–459. ISSN: 1545-4134. DOI: 10.1146/annurev-nucl-101917-021008.

[44] F. Kahlhoefer. "Review of LHC dark matter searches". In: *International Journal of Modern Physics A* 32.13 (2017), p. 1730006. ISSN: 1793-656X. DOI: 10.1142/s0217751x1730006x.

[45] S. et al. Cooper. "Proposal to the Gran Sasso laboratory for a dark matter search using cryogenic detectors". In: (1993).

[46] M. Bravin et al. "The CRESST dark matter search". In: *Astroparticle Physics* 12.1 (1999), pp. 107–114. ISSN: 0927-6505. DOI: 10.1016/S0927-6505(99)00073-0.

[47] G. Angloher et al. "CRESST-II: dark matter search with scintillating absorbers". In: *Nuclear Physics B - Proceedings Supplements* 138 (2005), pp. 153–155. ISSN: 0920-5632. DOI: 10.1016/j.nuclphysbps.2004.11.035.

[48] S. Di Lorenzo. "Multiple Detector Analysis in the CRESST Dark Matter Experiment". Dissertation. L'Aquila: Gran Sasso Science Institute, 2020.

[49] M. Agostini et al. "Modulations of the cosmic muon signal in ten years of Borexino data". In: *Journal of Cosmology and Astroparticle Physics* 2019.02 (2019), p. 046. DOI: 10.1088/1475-7516/2019/02/046.

[50] N. Agafonova et al. "LVD status report: underground muon physics". In: *Journal of Physics: Conference Series* 1690.1 (2020), p. 012101. DOI: 10.1088/1742-6596/1690/1/012101.

[51] G. Angloher et al. "Commissioning run of the CRESST-II dark matter search". In: *Astroparticle Physics* 31.4 (2009), pp. 270–276. ISSN: 0927-6505. DOI: 10.1016/j.astropartphys.2009.02.007.

[52] R. C. Jaklevic et al. "Quantum Interference Effects in Josephson Tunneling". In: *Phys. Rev. Lett.* 12 (7 1964), pp. 159–160. DOI: 10.1103/PhysRevLett.12.159.

[53] H. Weinstock. *SQUID Sensors: Fundamentals, Fabrication, and Applications*. NATO ASI series: Applied sciences. Kluwer Academic Publishers, 1996. ISBN: 9780792343509.

[54] CRESST Collaboration et al. *A likelihood framework for cryogenic scintillating calorimeters used in the CRESST dark matter search*. 2024. arXiv: 2403.03824 [astro-ph.CO].

[55] A. Fuß. "Simulation based Neutron Background Studies for the CRESST and COSINUS Dark Matter Search Experiments". Dissertation. Wien: Technische Universität Wien, 2022.

[56] G. Angloher et al. "Latest observations on the low energy excess in CRESST-III". In: *14th International Workshop on the Identification of Dark Matter 2022*. 2022. arXiv: 2207.09375 [astro-ph.CO].

[57] H. Kluck et al. "Latest results of CRESST-III's search for sub-GeV/c 2 dark matter". In: *Journal of Physics: Conference Series* 1468 (Feb. 2020), p. 012038. DOI: 10.1088/1742-6596/1468/1/012038.

[58] E. Aprile et al. "First Dark Matter Search with Nuclear Recoils from the XENONnT Experiment". In: *Phys. Rev. Lett.* 131 (4 2023), p. 041003. DOI: 10.1103/PhysRevLett.131.041003.

[59] F. Wagner. "Towards next-generation cryogenic dark matter searches with superconducting thermometers". Dissertation. Wien: Technische Universität Wien, 2023.

[60] S. Kuckuk. Dissertation in preperation. Tübingen: Uni Tübingen.

[61] S. Kuckuk. "Description of the low energy excess in CRESST using two-dimensional unbinned likelihood fits". 2023. URL: https://indico.cern.ch/event/1199289/contributions/5449613/. Poster presented at TAUP23 in Vienna, Austria.

[62] L. Hehn et all. "Improved EDELWEISS-III sensitivity for low-mass WIMPs using a profile likelihood approach". In: *The European Physical Journal C* (2016). DOI: 10.1140/epjc/s10052-016-4388-y.

[63] P. Adari et al. "EXCESS workshop: Descriptions of rising low-energy spectra". In: *SciPost Phys. Proc.* (2022), p. 001. DOI: 10.21468/SciPostPhysProc.9.001.

[64] I. Alkhatib et al. "Light Dark Matter Search with a High-Resolution Athermal Phonon Detector Operated above Ground". In: *Phys. Rev. Lett.* 127 (6 2021), p. 061801. DOI: 10.1103/PhysRevLett.127.061801.

[65] M. F. Albakry et al. "Investigating the sources of low-energy events in a SuperCDMS-HVeV detector". In: *Phys. Rev. D* 105 (11 2022), p. 112006. DOI: 10.1103/PhysRevD.105.112006.

[66] A. Aguilar-Arevalo et al. "Characterization of the background spectrum in DAMIC at SNOLAB". In: *Phys. Rev. D* 105 (6 2022), p. 062003. DOI: 10.1103/PhysRevD.105.062003.

[67] Liron Barak et al. "SENSEI: Direct-Detection Results on sub-GeV Dark Matter from a New Skipper CCD". In: *Phys. Rev. Lett.* 125 (17 2020), p. 171802. DOI: 10.1103/PhysRevLett.125.171802.

[68] M. Stahlberg. "Probing low-mass dark matter with CRESST-III : data analysis and first results". PhD thesis. Technische Universität Wien, 2020.

[69] D. Fuchs. "New Analysis Methods for Enhanced Sensitivity to Light Dark Matter at CRESST-III and Studies of Discovery Potential for Next Generation Cryogenic Experiments". Dissertation. München: Technische Universität München, 2023.

[70] R. Brun et al. *root-project/root: v6.18/02*. Version v6-18-02. June 2020. DOI: 10.5281/zenodo.3895860.

[71] F. Pröbst et al. "Model for cryogenic particle detectors with superconducting phase transition thermometers". In: *Journal of Low Temperature Physics* 100.1-2 (1995), pp. 69–104. DOI: 10.1007/BF00753837.

[72] M. Mancuso et al. "A Low Nuclear Recoil Energy Threshold for Dark Matter Search with CRESST-III Detectors". In: *J. Low Temp. Phys.* 193.3-4 (2018), pp. 441–448. DOI: 10.1007/s10909-018-1948-6.

[73] M.M. Bé et al. *Update of X Ray and Gamma Ray Decay Data Standards for Detector Calibration and Other Applications. Volume 2*. Vienna, Austria: International Atomic Energy Agency, 2007.

[74] G. Angloher et al. "Observation of a low energy nuclear recoil peak in the neutron calibration data of the CRESST-III experiment". In: *Phys. Rev. D* 108 (2023), p. 022005. DOI: 10.1103/PhysRevD.108.022005.

[75] H. Abele et al. "Observation of a Nuclear Recoil Peak at the 100 eV Scale Induced by Neutron Capture". In: *Phys. Rev. Lett.* 130 (2023), p. 211802. DOI: 10.1103/PhysRevLett.130.211802.

[76] L. Thulliez et al. "Calibration of nuclear recoils at the 100 eV scale using neutron capture". In: *Journal of Instrumentation* 16.07 (2021), P07032. DOI: 10.1088/1748-0221/16/07/P07032.

[77] D. Schmiedmayer. "Calculation of dark-matter exclusions-limits using a maximum Likelihood approach". Diplomathesis. Wien: Technische Universität Wien, 2019.

[78] R.J. Strauß. "Energy-dependent quenching factor measurements of $CaWO_4$ crystals at mK temperatures and detector prototypes for direct dark matter search with CRESST". PhD thesis. Munich: Technische Universität München, 2013.

[79] S. Yellin. "Finding an upper limit in the presence of an unknown background". In: *Phys. Rev. D* 66 (3 2002), p. 032005. DOI: 10.1103/PhysRevD.66.032005.

[80] Roger Barlow. "Extended maximum likelihood". In: *Nuclear Instruments and Methods in Physics Research Section A: Accelerators, Spectrometers, Detectors and Associated Equipment* 297.3 (1990), pp. 496–506. ISSN: 0168-9002. DOI: 10.1016/0168-9002(90)91334-8.

[81] S. S. Wilks. "The Large-Sample Distribution of the Likelihood Ratio for Testing Composite Hypotheses". In: *The Annals of Mathematical Statistics* 9.1 (1938), pp. 60–62. DOI: 10.1214/aoms/1177732360.

[82] Glen Cowan et al. "Asymptotic formulae for likelihood-based tests of new physics". English (US). In: *European Physical Journal C* 71.2 (Feb. 2011). ISSN: 1434-6044. DOI: 10.1140/epjc/s10052-011-1554-0.

[83] J. G. Proakis and D. G. Manolakis. *Digital Signal Processing (3rd Ed.): Principles, Algorithms, and Applications*. USA: Prentice-Hall, Inc., 1996. ISBN: 0133737624.

[84] R. G. Lyons. *Understanding Digital Signal Processing (2nd Edition)*. USA: Prentice Hall PTR, 2004. ISBN: 0131089897.

[85] Andreas Maier et al. *Medical Imaging Systems : An Introductory Guide*. eng. 1st ed. 2018. Image Processing, Computer Vision, Pattern Recognition, and Graphics. Cham: Springer International Publishing, 2018. ISBN: 3-319-96520-4.

[86] M.; Owen. *Practical Signal Processing*. Cambridge; Cambridge University Press., 2007.

[87] S. Butterworth. "On the Theory of Filter Amplifiers". In: *Experimental Wireless & the Wireless Engineer* 7 (Oct. 1930), pp. 536–541.

[88] L. Wanhammar. "4 - Digital Filters". In: *DSP Integrated Circuits*. Ed. by Lars Wanhammar. Academic Press Series in Engineering. Burlington: Academic Press, 1999, pp. 115–186. ISBN: 978-0-12-734530-7.

[89] S. Gupta. "Sub-GeV Dark Matter Studies and Universal Bound States Exploration with CRESST-III". Dissertation. Wien: Technische Universität Wien, 2024.

[90] A. Bertolini. Dissertation in preperation. Garching: MPP Garching.

[91] G. Angloher et al. "Testing spin-dependent dark matter interactions with lithium aluminate targets in CRESST-III". In: *Phys. Rev. D* 106 (9 2022), p. 092008. DOI: 10.1103/PhysRevD.106.092008.

[92] F. Wagner et al. "Cait: Analysis Toolkit for Cryogenic Particle Detectors in Python". In: *Comput. Softw. Big Sci.* 6.1 (2022), p. 19. DOI: 10.1007/s41781-022-00092-4. arXiv: 2207.02187 [physics.ins-det].

[93] L. Einfalt. Dissertation in preperation. Wien: Technische Universität Wien.

[94] E. Queguiner. "Analysis of the data of the EDELWEISS-LT experiment searching for low-mass WIMP". Dissertation. Université de Lyon, 2018.

[95] J. P. Franck and Douglas L. Martin. "THE SUPERCONDUCTING TRANSITION TEMPERATURE OF LEAD". In: *Canadian Journal of Physics* 39.9 (1961), pp. 1320–1329. DOI: 10.1139/p61-156.

[96] S. Di Lorenzo. internal communication. 2023.

[97] G. Audi et al. "The Nubase evaluation of nuclear and decay properties". In: *Nuclear Physics A* 729.1 (2003). The 2003 NUBASE and Atomic Mass Evaluations, pp. 3–128. ISSN: 0375-9474. DOI: https://doi.org/10.1016/j.nuclphysa.2003.11.001.